



UCGE Reports
Number 20284

Department of Geomatics Engineering

**Continuous Measurement-While-Drilling Surveying
System Utilizing MEMS Inertial Sensors**

(URL: <http://www.geomatics.ucalgary.ca/research/publications>)

by

Mahmoud Lotfy ElGizawy

February 2009



UNIVERSITY OF CALGARY

Continuous Measurement-While-Drilling Surveying System Utilizing
MEMS Inertial Sensors

by

Mahmoud Lotfy ElGizawy

A THESIS

SUBMITTED TO THE FACULTY OF GRADUATE STUDIES
IN PARTIAL FULFILMENT OF THE REQUIREMENTS FOR THE
DEGREE OF DOCTOR OF PHILOSOPHY

DEPARTMENT OF GEOMATICS ENGINEERING

CALGARY, ALBERTA

FEBRUARY, 2009

© Mahmoud Lotfy ElGizawy 2009

ABSTRACT

Oil and gas are global fuels obtained primarily from drilling wells in underground terrestrial reservoirs. Vertical drilling is preferred because of its simplicity and therefore low cost, but subsurface targets can often be procured only by directing the wellbore along predefined nonvertical trajectories. For instance, directional drilling must be employed to reach locations inaccessible to the drilling rig, to side track an existing well (multilateral drilling), or to drill multiple wells from the same offshore platform (horizontal drilling). A complete knowledge of the wellbore direction and orientation during the drilling process is essential to guarantee proper directional drilling procedure. Thus, besides the conventional drilling assembly, directional drilling operations require position sensors to provide azimuth, inclination, and toolface angles of the drill. These sensors are part of the measurement-while-drilling (MWD) tool, which in current technology is installed several feet behind the drill bit. Values for inclination and toolface angles are determined from accelerometer measurements at predetermined stationary surveying stations; these values are then incorporated with magnetometer measurements to deliver the azimuth angle. Values for inclination and azimuth angles at the current surveying station are combined with those from the previous station to compute the position of the probe. However, there is no accurate information about the wellbore trajectory between survey stations. Additionally, the magnetic field of the magnetometers has deleterious effect on the overall accuracy of surveying measurements.

A method to provide continuous information about the wellbore trajectory has been developed in this study. The module developed integrates a rotary steerable

system (RSS) and MWD tool into one drilling probe utilizing inertial navigation system (INS) technology. This is achieved by designing a reliable real-time low cost MWD surveying system based on MEMS inertial sensors miniaturized inside the RSS housing installed directly behind the drill bit. A continuous borehole surveying module based on MEMS inertial sensors integrated with other drilling measurements was developed using Kalman filtering. In addition, qualification testing of MEMS accelerometers and gyroscopes under hostile drilling environments was conducted. Techniques to detect and mitigate shock and vibration effects while drilling are proposed to enhance the performance of the MEMS inertial sensors.

ACKNOWLEDGEMENTS

Writing this acknowledgement concludes a long journey, which could have never been possible without the support and encouragement of many people.

- My precious parents: You were always there for me, thank you for teaching me the value of working hard to achieve my goals, and the value of the family to have a happy life. Your unconditional love, endless support, and continuous encouragement mean so much to me and shall put me in debt forever. My sister: thank you for inspiring me by your dedication, patience, love, and support.
- My lovely wife Safa and my adorable daughter Zaina: I could not have gone this far without you beside me. Thank you for your encouragement and support through this thesis journey, and for your patience to reach a happy ending. I am so looking forward to enjoying more of our times together without having to interrupt them to work on my thesis.
- My distinguished supervisors Dr Naser El-Sheimy and Dr Aboelmagd Nouredin: Thank you for believing in me from the first day. Your clear guidance, valuable time, fruitful discussions, and continuous support are immensely appreciated.
- My examination committee Dr Andrew Hunter, Dr. Mohamed Ibnkahla, Dr Gérard Lachapelle and Dr. Abu Sesay are acknowledged for reviewing this dissertation and for their constructive comments.

- The wonderful staff at the Department of Geomatics Engineering is thanked for their help and for making things easy over the past years. Special thanks go to Lu-Anne Markland, Monica Barbaro, Macia Inch, Julia Lai, Gail Leask, Kirk Collins, and Garth Wannamaker.
- Many thanks to my colleagues at the University of Calgary for sharing their time with me, especially Dr Taher Hassan, Dr Samah Nassar, Bruce Wright, Wes Teskey, Dr Chris Goodall, Dr Zainab Syed, Priyanka Aggarwal, Dr Mohamed Youssef, and Dr Mohamed El-Habiby.
- My good friends in Calgary and Edmonton, Dr. Hatem Ibrahim, Dr Walid Abdel-Hamid, Hussain Lala, Dr. Abdallah Osman, Dr Ahmed H. Osman, Dr Mohamed Elshayeb, and Ihab Farag: Thank you for the good times we spent together. Dr Samer Adeeb, thank you for the fun time through the past 10 years, and for convincing me that I am always right and I can do it.
- I also acknowledge the Natural Sciences and Engineering Research Council of Canada (NSERC), the Queen Elizabeth II award, the Innovation in Mobile Mapping Award, and the Department of Geomatics Engineering Graduate Research Scholarships at the University of Calgary for providing the financial support for this dissertation.

DEDICATION

To my parents, my sister, my sweet wife, and my adorable daughter

"All that I am, and all that I will ever be, I owe to you"

TABLE OF CONTENTS

APPROVAL	ii
ABSTRACT.....	ii
ACKNOWLEDGEMENTS.....	iv
DEDICATION.....	vi
LIST OF TABLES.....	x
LIST OF FIGURES AND ILLUSTRATIONS.....	xi
CHAPTER ONE: INTRODUCTION.....	1
1.1 Background.....	1
1.2 Problem Statement.....	4
1.3 Research Contributions.....	6
1.4 Dissertation Outline.....	7
CHAPTER TWO: WELL BORE SURVEYING TECHNOLOGIES.....	10
2.1 Hydrocarbon Well Life Cycle.....	10
2.2 Measurements-While-Drilling Magnetic Based System.....	14
2.2.1 Magnetometers.....	14
2.2.2 Magnetometer MWD Limitations.....	18
2.2.2.1 Drill string magnetic interference.....	19
2.2.2.2 External magnetic interference.....	19
2.2.2.3 BHA sag effect.....	21
2.3 Measurements-While-Drilling Gyroscope Based System.....	21
2.3.1 In Hole Orientation Gyroscope Tool.....	22
2.3.2 Wireline Gyroscope Tool.....	22
2.3.3 Single-Axis Gyroscope Based MWD Tool.....	24
2.3.4 Dual-Axes Gyroscope Based MWD Tool.....	26
2.4 RSS Technology.....	28
2.4.1 RSS Overview and Advantages.....	28
2.4.2 RSS Challenges.....	30
2.5 Proposed Integrated RSS Technology.....	32
CHAPTER THREE: SHOCK AND VIBRATION CHALLENGE WHILE DRILLING.....	33
3.1 Characteristics of MEMS Inertial Sensors.....	34
3.2 Direction and Inclination Package Preparation.....	37
3.3 Shock Qualification Testing.....	38
3.3.1 Test Setup.....	39
3.3.2 Sensors Qualification under Drilling Shock.....	41
3.3.3 Analysis of Shock Impact.....	43
3.4 Vibration Qualification Testing.....	51
3.4.1 Test Setup.....	52
3.4.2 Sensor Qualification under Drilling Vibration.....	53

3.4.3 Analysis of Vibration Effect.....	55
3.5 Summary	59
 CHAPTER FOUR: PERFORMANCE ENHANCEMENT UNDER DRILLING	
SHOCK AND VIBRATION	61
4.1 Wavelet Transform	64
4.1.1 Continuous and Discrete Wavelet Transform	67
4.1.2 Wavelet Multi-Resolution Analysis WMRA	68
4.1.3 Wavelet Packet Transform WPT	71
4.2 Shock Effects on MEMS Sensors	73
4.2.1 WPT analysis of shock forces	73
4.2.2 Detection of Shock Impact	79
4.3 Vibration Effects on MEMS Sensors.....	83
4.3.1 WPT Analyses of Vibration Effects	83
4.3.2 Detection of Vibration Effects.....	87
4.4 Mitigation of Harsh Drilling Environment Effects.....	89
4.5 Summary	94
 CHAPTER FIVE: CONTINUOUS WELL TRAJECTORY WHILE DRILLING	
BASED ON KALMAN FILTERING	96
5.1 Current Industrial Well Trajectory Computation while Drilling	96
5.2 Continuous Well Trajectory while Drilling Based on the INS Mechanization	99
5.2.1 Mechanization Equations	100
5.2.2 Computational Coordinates Frames	102
5.2.3 Transformation between Navigation Frame and Body Frame	105
5.2.4 Modeling Motion in Navigation Frame.....	105
5.2.5 Directional Drilling Parameter Computations.....	107
5.2.6 Drill Bit Synthetic Attitude Angles	111
5.3 Surveying Error Modelling Using Linear State Equations.....	112
5.4 Kalman Filtering to Limit Error Growth of Inertial Sensor Measurements	113
5.4.1 Kalman Filtering Algorithm	113
5.4.2 Drilling Observation Updates for Kalman Filtering.....	119
5.4.2.1 <i>Continuous surveying observations updates while drilling</i>	120
5.4.2.2 <i>Stationary surveying observation updates</i>	123
5.5 Setup of Soft and Hard Formation Drilling Tests.....	126
5.6 Analysis of Results for Soft Formation Drilling Test.....	134
5.6.1 Analysis of Raw Measurements	134
5.6.2 Estimation Errors—Covariance Analysis.....	138
5.6.2.1 Position errors	138
5.6.2.2 Velocity errors	140
5.6.2.3 Attitude errors	141
5.6.2.4 Inertial sensor errors	143
5.6.3 Position Results Analysis	144
5.6.3.1 Drilling with continuous updates and no telemetry interruption	145
5.6.3.2 Drilling with continuous updates during telemetry interruption	
periods	147
5.6.3.3 Limiting position error growth during telemetry interruption	149

5.6.4 Velocity Results.....	151
5.6.4.1 Drilling with continuous updates and no telemetry interruption	151
5.6.4.2 Drilling with continuous updates during telemetry interruption periods	152
5.6.4.3 Limiting velocity error growth during telemetry interruption	153
5.6.5 Attitudes Results.....	154
5.6.5.1 Drill bit inclination and toolface results analysis.....	154
5.6.5.2 Synthetic drill bit inclination angle and toolface angle	156
5.6.5.3 Analysis of azimuth angle results	158
5.6.5.4 Stationary azimuth angle updates	159
5.7 Analysis of Test Results from Hard Formation Drilling	160
5.7.1 Position Results	161
5.7.2 Velocity Results.....	163
5.7.3 Attitude Results	164
5.8 Conclusions.....	166
CHAPTER SIX: CONCLUSIONS AND THESIS CONTRIBUTIONS	168
6.1 Summary.....	168
6.2 Conclusions and Thesis Contributions	169
6.3 Recommendations and Future Research.....	173
REFERENCES	175
APPENDIX A: MODELING MOTION IN NAVIGATION FRAME	187
A.1 Position Mechanization in the Navigation Frame.....	187
A.2 Velocity Mechanization in the Navigation Frame	189
A.3 Attitude Mechanization in the Navigation Frame.....	193
APPENDIX B: INS MECHANIZATION EQUATIONS SOLUTION BY QUATERNION	196
APPENDIX C: SURVEYING ERROR MODELLING USING LINEAR STATE EQUATIONS.....	201
C.1 Drill String Coordinate Errors.....	201
C.2 Drill String Velocity Errors.....	202
C.3 Drill String Attitude Errors	204
C.4 Inertial Sensor Error Modelling	206

LIST OF TABLES

Table 2.1: Characteristics of a Flux Gate Magnetometer	18
Table 3.1: Characteristics of MEMS Sensors Manufactured by Analog Devices Inc,.....	36
Table 4.1: Threshold of Shock Levels	81
Table 4.2: Signal Output Uncertainty of Raw and Filtered Measurements	94
Table 5.1: Crossbow IMU300CC Specifications [Crossbow, 2007]	133
Table 5.2: HG1700 Specifications [Honeywell, 1997].....	134
Table 5.3: Improvements in SNR of Output Signals	136

LIST OF FIGURES AND ILLUSTRATIONS

Figure 1.1: Dissertation Outline.....	9
Figure 2.1: Drilling Well Types [Bourgoyne et al., 2005].....	11
Figure 2.2: Conventional PDM Motor behind the Drill Bit [Berger et al., 1999]	13
Figure 2.3: Arrangement of Sensors in an MWD Tool [Eickelberg, 1982]	16
Figure 2.4: Single FOG Installed inside the Bearing Assembly [Noureldin, 2002]	26
Figure 2.5: Dual-Axes Gyroscope MWD Tool [Noureldin, 2002].....	28
Figure 2.6: MWD Tool Installed behind RSS	31
Figure 3.1: MEMS Inertial Measurements Unit Stacked and Foamed before Testing.....	38
Figure 3.2: a) IMU Installed in the V-Channel; b) Shock Test Fixture	40
Figure 3.3: Orthogonal Accelerometers Measurements under 1400 g Shocks.....	42
Figure 3.4: Raw Measurements of Two Channels.....	44
Figure 3.5: PSD of Forward Accelerometer Measurements at Different Shock Levels...	47
Figure 3.6: PSD of Upward Gyroscope Measurements at Different Shock Levels.....	51
Figure 3.7: Sensors Package Installed on the Vibration Table	53
Figure 3.8: Accelerometer Measurements throughout Vibration Test	54
Figure 3.9: Screen Capture of Vibration Test Parameters	56
Figure 3.10: PSD of Accelerometer X Output Signal Contaminated by Vibration Effects	58
Figure 3.11: PSD of Gyroscope Z Output Signal Contaminated by Vibration Effects	59
Figure 4.1: Time-Frequency Representation of Short Time Fourier Transform STFT [Robertson et al., 1996].....	63
Figure 4.2: Time Frequency Representation of Wavelet Transform WT [Robertson et al., 1996].	65
Figure 4.3: Mother Wavelets [Misiti et al., 2000]	66
Figure 4.4: WMRA Structure at 3 Levels of Decomposition of the Input Signal	71

Figure 4.5: WPT of 3 Levels of Decomposition of the Input Signal	72
Figure 4.6: Raw Measurements under 1400 g Shock Forces	74
Figure 4.7: WPT Accelerometer Signal Decomposition at Level 6 under Shock	76
Figure 4.8: WPT Gyroscope Signal Decomposition at Level 6 under Shocks.....	78
Figure 4.9: Energy of Extracted Packet Detail D1 (a), and Approximation A6 (b)	82
Figure 4.10: Raw Measurements under Vibration Effects.....	83
Figure 4.11: WPT Accelerometer Signal Decomposition at Level 6 under Vibration.....	85
Figure 4.12: WPT Gyroscope Signal Decomposition at Level 6 under Vibration	86
Figure 4.13: Energy of Extracted Packet Detail D1 (a) and Approximation A6 (b)	88
Figure 4.14: MEMS Accelerometer Output Signals Under Vibration (upper panel), Denoised Signals (lower panel)	91
Figure 4.15: MEMS Gyroscope Output Signals under Vibration (upper panel), Denoised Signals (lower panel)	93
Figure 5.1: MCM Stationary Survey	98
Figure 5.2: Body Frame (Drill String Frame) Axes of the Rotary Steerable System.....	103
Figure 5.3: Navigation Frame (N, E, and UP) of a Given Point relative to the Earth- Fixed Frame	104
Figure 5.4: INS Mechanization in the Navigation Frame.....	106
Figure 5.5: Block Diagram of the Kalman Filtering Sequential Recursive Algorithm ..	116
Figure 5.6: Drilling Scheme of Kalman Filtering.....	120
Figure 5.7: Drilling Simulation Test—Rotation Table in Vertical Position.....	127
Figure 5.8: Drilling Simulation Test—Rotation Table in Inclined Position.....	128
Figure 5.9: Drilling Simulation Test—Rotation Table in Highly Inclined Section.....	128
Figure 5.10: Test 1 Rotation Rates around the 3 Axes	131
Figure 5.11: Test 2 Rotation Rates around the 3 Axes	132
Figure 5.12 Accelerometer X (upper panel), Y (middle panel), and Z (lower panel) Measurements before and after Wavelet Denoising	135

Figure 5.13: Gyroscope X (upper panel), Y (middle panel), and Z (lower panel) Measurements before and after Wavelet Denoising	137
Figure 5.14: Covariance of Position Components during Drilling with a Continuous Drill Bit Rate of Penetration Updates and Stationary Updates	139
Figure 5.15: Covariance of Position Components during Drilling with Continuous MCM Position/Drill Bit Rate of Penetration Updates and Stationary Updates	140
Figure 5.16: Covariance of Velocity Components during Drilling with Continuous MCM Position/Drill Bit Rate of Penetration Updates and Stationary Updates	141
Figure 5.17: Covariance of Attitude Components during Drilling with Continuous MCM Position/Drill Bit Rate of Penetration Updates and Stationary Updates	142
Figure 5.18: Covariance of Inertial Sensor Errors during Drilling with Continuous MCM Position/Drill Bit Rate of Penetration Updates and Stationary Updates	144
Figure 5.19: North Position Derived by KF Compared to a Reference Position (upper panel); Position Errors (lower panel) during Drilling	145
Figure 5.20: East Position Derived by KF Compared to a Reference Position (upper panel), Position Errors (lower panel) during Drilling	146
Figure 5.21: Altitude Derived by KF Compared to a Reference Altitude (upper panel), Position Errors (lower panel) during Drilling	147
Figure 5.22: Position Errors in North (upper panel), East (middle panel), and Altitude (lower panel) Directions	148
Figure 5.23: Position in North Direction Compared to a Reference Position (upper panel); Position Errors (lower panel)	149
Figure 5.24: Position in East Direction Compared to a Reference Position (upper panel); Position Errors (lower panel)	150
Figure 5.25: Altitude Position Compared to a Reference Altitude (upper panel); Position Errors (lower panel)	150
Figure 5.26: Velocity Error in East (upper panel), North (middle panel), and Up (lower panel) Directions	151
Figure 5.27: Velocity Error in East (upper panel), North (middle panel), and Up (lower panel) Directions	153
Figure 5.28: Velocity Errors in East (upper panel), North (middle panel), and Up (lower panel) Directions	154

Figure 5.29: KF Pitch Angle Compared to Reference Angle (upper panel); Error in the Pitch Angle (lower panel).	155
Figure 5.30: KF Toolface Angle Compared to Reference Drill bit Toolface Angle (upper panel); Error in Toolface Angle (lower panel).	156
Figure 5.31: Synthetic Pitch Angle Compared to Reference and KF Derived Pitch Angles (upper panel); Error in Synthetic Pitch Angle (lower panel).	157
Figure 5.32: Synthetic Toolface Angle Compared to Reference and KF Derived Toolface Angles (upper panel); Error in Synthetic Toolface Angle (lower panel).	157
Figure 5.33: KF Azimuth Angle Compared to a Reference Angle (upper panel); Errors in Azimuth Angle (lower panel)	158
Figure 5.34: KF Azimuth Angle Compared to a Reference Angle (upper panel); Errors in the Azimuth Angle (lower panel)	160
Figure 5.35: Position in North Direction Compared to the Reference North Position (upper panel); Error in North Position (lower panel).	162
Figure 5.36: East Position Compared to the Reference East Position (upper panel); Error in East Position (lower panel).	162
Figure 5.37: Altitude Compared to the Reference Altitude (upper panel); Error in Altitude (lower panel)	163
Figure 5.38: Velocity Error in East (upper panel), North (middle panel) and Up (lower panel) Directions.	164
Figure 5.39: Synthetic Pitch Angle Compared to Reference and KF Driven Pitch Angles (upper panel); Error in Synthetic Pitch Angle (lower panel).	165
Figure 5.40: Synthetic Toolface Angle Compared to Reference and KF Driven Toolface Angles (upper panel); Error in Synthetic Toolface Angle (lower panel)	165
Figure 5.41: KF Azimuth Compared to a Reference Azimuth (upper panel); Error in Azimuth (lower panel)	166
Figure A.1: Velocity Components of a Given Point in the Navigation Frame	188
Figure A.2: Change of Orientation of the Navigation Frame	191

LIST OF ABBREVIATIONS AND SYMBOLS

Abbreviations

BHA	Bottom hole assembly
CWT	Continuous wavelet transform
DFT	Discrete Fourier transform
FOG	Fibre optic gyroscope
FT	Fourier transform
GBR	Gas bearing gyroscope
GM	Gauss-Markov
Hz	Hertz
IMU	Inertial measurement unit
INS	Inertial navigation system
KF	Kalman filter
LWD	Logging while drilling
MBG	Mechanical based gyro
MCM	Minimum curvature method
MEMS	Micro-electro-mechanical-systems
MSEE	Mean square estimate error
MWD	Measurement while drilling
PDM	Positive displacement motor
PSD	Power spectral density
psi	Pressure per square inch
RLG	Ring laser gyro
RMS	Root mean square
rpm	Revolution per minute
RSS	Rotary steerable system
SNR	Signal to noise ratio
STFT	Short time Fourier transform
TVD	True vertical depth
vpm	Vibration per minute
WBM	Well bore mapping
WMRA	Wavelet multi-resolution analysis
WPT	Wavelet packet transform
WT	Wavelet transform
ZUPT	Zero velocity update

Symbols

f_x	Accelerometer measurement along x -direction
f_y	Accelerometer measurement along y -direction

f_z	Accelerometer measurement along z-direction
g	Earth's gravity
K	Kalman gain
M_x	Magnetometer measurement along x-direction
M_y	Magnetometer measurement along y-direction
M_z	Magnetometer measurement along z-direction
ω_x	Gyro measurement along x-direction
ω_y	Gyro measurement along y-direction
ω_z	Gyro measurement along z-direction
θ	Pitch angle
I	Inclination angle
ϕ	Toolface angle
ψ	Azimuth angle
σ	Standard deviation
φ	Latitude angle
λ	Longitude angle
h	Altitude
Q	Covariance matrix of measurement noise
R	Covariance matrix of observation noise
V^n	Velocity in north direction
V^e	Velocity in east direction
V^u	Velocity in up direction

CHAPTER ONE:

INTRODUCTION

1.1 Background

Directional drilling is the science of directing a wellbore along a predefined trajectory leading to a subsurface target [Bourgoyne et al., 2005]. Directional drilling is essential for many reasons such as inaccessible surface locations to the drilling rig, side tracking of an existing well, drilling multiple wells from the same offshore platform, multilateral drilling, and horizontal drilling. Additionally, horizontal wells have higher oil and gas deliverability where they have larger contact area with oil and gas reservoirs [Joshi and Ding, 1991]. This in turn substantially reduces the cost and time of drilling operations. Thus, in recent years, the development of directional well drilling technologies has gained more attention than improvements in vertical drilling technologies in Canadian global oil and gas industries.

In Huntington Beach, California, the first controlled directional well was drilled in the 1930s; however, it was initially used for the unethical purpose of crossing property lines. Up to 1950, directional wells were drilled by using whipstocks and bit jetting techniques to deviate the well path [Bourgoyne et al., 2005]. In the 1960s the first commercial positive displacement motor (PDM) was used for directional drilling. The PDM is constructed with a bent housing to provide a side force to the bit and to deflect

the hole trajectory. The 1980s witnessed the first use of a measurement-while-drilling (MWD) tool. In 1999 a rotary steerable system (RSS) entered directional drilling markets. The RSS increased the efficiency of directional drilling operations by reducing drilling time due to a continuous rotation of the entire drill string while drilling. In addition, an RSS provides better borehole cleaning with fewer wiper trips, optimizes drilling parameters, and provides a higher rate of penetration while drilling.

Complete knowledge of the drill bit direction and orientation during the drilling process is essential to guarantee proper directional drilling. Thus, besides the conventional drilling assembly, directional drilling operations require position sensors to provide estimations of the azimuth (deviation from the north direction in the horizontal plane), the inclination (deviation from the vertical direction, or pitch angle), and the toolface angle (roll angle) of the drill bit [Conti et al., 1989]. These sensors are part of the MWD tool, which is installed several feet behind the drill bit to monitor all physical parameters that affect the drilling operation. After completing the drilling procedure, a quality control process known as well-bore mapping (WBM) is performed for established directional wells. WBM determines the well bore trajectory and direction as a function of depth and compares it to the planned (designed) trajectory and direction [Bourgoyne et al., 2005].

The directional drilling system includes directional MWD equipment, a steering system, a drilling assembly, and data links to communicate measurements taken from the bottom of the hole to the surface. The drilling assembly for directional drilling

consists of a bit, a high-speed motor, nonmagnetic drill collars, and a drill pipe. The nonmagnetic drill collar holds the surveying equipment. The directional drilling procedure begins with drilling a vertical hole to an appropriate depth using conventional rotary drilling. The directional drilling assembly is then installed in the hole. The bit is directed toward the desired offset angle (azimuth direction) using the adjustable housing in a PDM motor. The offset angle is usually 1.5 degrees, with a maximum of 3 degrees [Fisher et al., 1991].

The azimuth direction is determined in a stationary mode by using three-axis magnetometers, while the inclination and the toolface angle are determined using three-axis accelerometers. As soon as the azimuth, inclination, and toolface of the drill bit is determined, drilling starts in either a sliding or rotary drilling mode. In a sliding mode, the entire drill string does not rotate while the bend points the bit in a direction different from the axis of the well bore. Drilling commences as soon as drilling fluid is pumped through the motor. The drill bit turns and cuts through the formation. As soon as the well bore direction is achieved, the entire drill string is rotated and drills straight rather than at an angle. The rotary mode has the advantage of providing ultimately smoother boreholes; also, it allows higher rates of penetration. If using an RSS instead of a PDM motor, the drilling is always in a rotary mode. However, drilling has to stop frequently at surveying stations in order to measure the inclination, azimuth, and the drilled length using the MWD tool. The well trajectory is then computed between the two surveying stations based on mathematical assumptions; for instance, it may be assumed that the drilled distance is a smooth arc.

The current technology available for MWD tools utilizes a set of three accelerometers to monitor tool inclination and toolface. Another set of three magnetometers is used to monitor the drilling azimuth of the tool [Helm, 1991; Thorogood and Knott, 1990; Russel and Russel, 1979]. On the other hand, the RSS utilizes three accelerometers to monitor the toolface of the drilling bit. The steerable system reacts mechanically according to the measured toolface and corrects the drill bit direction based only on the toolface information.

1.2 Problem Statement

Within the scope of this research, the following are current problems and challenges that face the directional drilling industry:

1. MWD technologies are currently based on systems integrating three magnetometers and three accelerometers. Toolface, inclination, and azimuth angles are determined at surveying stations when drilling is stationary. Therefore, there is no accurate information available about the wellbore trajectory between the survey stations. Additionally, the use of magnetometers has a deleterious effect on the overall accuracy of the surveying process. Factors such as magnetic interference of drill string components, formation ore deposits, and solar magnetic storms disturb magnetometer measurements. In an attempt to partially reduce the effects of such magnetic interference, drilling companies install surveying sensors inside an expensive nonmagnetic drill collar [Russel and Roesler, 1985; Grindord

and Wolf, 1983]. This minimizes but does not eliminate magnetic interference with magnetometer measurements.

2. Drilling motors/RSS and stabilizer collars are installed directly behind the drill bit, and then followed by the MWD tool. Thus, the MWD tool which contains the surveying sensors is installed at least 15 meters behind the drill bit. Accordingly, a directional driller has to drill 15 metres in order to know the drill bit position, toolface, inclination, and azimuth. If the wellbore deviates from the designed plan, it is expensive to correct, especially in hard formation where drilling is relatively slow.
3. A current drawback of the RSS is that it cannot utilize azimuth information in steering the well. The present technology separates the MWD tool and the RSS. Integration into one drill housing is impossible because of the high magnetic interference on the bit when the magnetometer is inside the RSS.
4. Harsh and hostile drilling environments invoke wear on drill electronic components and sensors when the drill bit grinds through hard formations. This is the main challenge for sensors, and tremendous cost is incurred if sensors fail while drilling. This limits the use of gyroscope technology in drilling.
5. Wellbore diameters can be as small as 152.4 mm (6 in), which restricts MWD or RSS housing to a maximum outer diameter of 120.65 mm (4.75 in). A portion of this outer diameter is used to flow the drilling fluid through the drill string. Thus, the size limitations of electronics and sensors play a major role in sensor selection criteria.

6. Recently, a gyroscopic surveying system has been developed for MWD operations replacing the three-axis magnetometers with single and dual fibre optic gyroscopes (FOG) [Noureldin, 2003]. This system has a major drawback; that is, there is a limited space available inside the MWD tool and the collar cannot accommodate a complete inertial measurement unit (IMU) containing three orthogonal fibre optic gyroscopes. In addition, this type of gyroscope is highly susceptible to the high shocks and vibrations encountered in drilling operations.

1.3 Research Contributions

Real implementation of gyroscope technology while drilling is thought to be impossible due to the harsh drilling environment. This limits the use of gyroscopes as they cannot sustain the severe shocks and vibrations downhole. This research aims to develop a solution for the directional drilling operation that integrates the RSS and the MWD tool into one drilling housing utilizing gyroscope technology. This is achieved by:

1. Developing a reliable real-time low cost MWD surveying system based on micro-electro-mechanical-system (MEMS) inertial sensors so that it can be miniaturized inside the RSS housing installed directly behind the drill bit;
2. Qualifying the MEMS accelerometers and gyroscopes for directional drilling applications;
3. Developing a methodology to detect shock and vibration levels while drilling based on the MEMS inertial sensors measurements;

4. Developing a denoising module to enhance the performance of MEMS inertial sensors under high shock and vibration environments;
5. Integrating some of the rig drilling parameters with MEMS inertial sensor measurements to develop a continuous surveying system in a drilling module based on Kalman filtering (KF).

1.4 Dissertation Outline

Current industrial technologies available for MWD and RSS are reviewed in chapter 2. MWD magnetic based technology and the various challenges that face magnetic sensors are discussed. In addition, this chapter presents an up-to-date development of the MWD gyroscope based technology as well as RSS technology and the motivation for this study.

In chapter 3 the qualification testing of MEMS gyroscopes and accelerometer sensors under severe drilling shock and vibration conditions is discussed according to drilling industry standards. Chapter 3 also includes a frequency analysis of sensors measurements under shock and vibration.

The MEMS inertial sensor performance enhancement module under severe drilling shock and vibration is discussed in chapter 4. The module is based on wavelet packet analysis and thus an introduction to the wavelet transform, wavelet multi-resolution analysis, and wavelet packets are described in this chapter. Additionally, a novel

methodology to detect the shock and vibration level while drilling based on MEMS inertial sensor measurements is introduced.

The continuous well trajectory while drilling based on Kalman filtering is presented and discussed in chapter 5. This chapter also discusses the integration of rig drilling parameters (e.g., drilling rate of penetration, draw-work measured depth) with MEMS inertial sensor measurements. Chapter 5 also gives details of the experimental work for drilling simulation through soft and hard formation experiments and presents the results analysis of position, velocity, and attitude angles of the simulated well trajectory. This chapter establishes the implementation of the synthetic inclination and toolface angles of the drill bit while drilling based entirely on accelerometer measurements. Furthermore, it introduces the zero integrated position and velocity error during periods of telemetry interruptions.

Chapter 6 concludes this study with a summary and description of thesis contributions. Recommendations for future enhancements of the technology developed here are provided. The dissertation outline is illustrated in Figure 1.1.

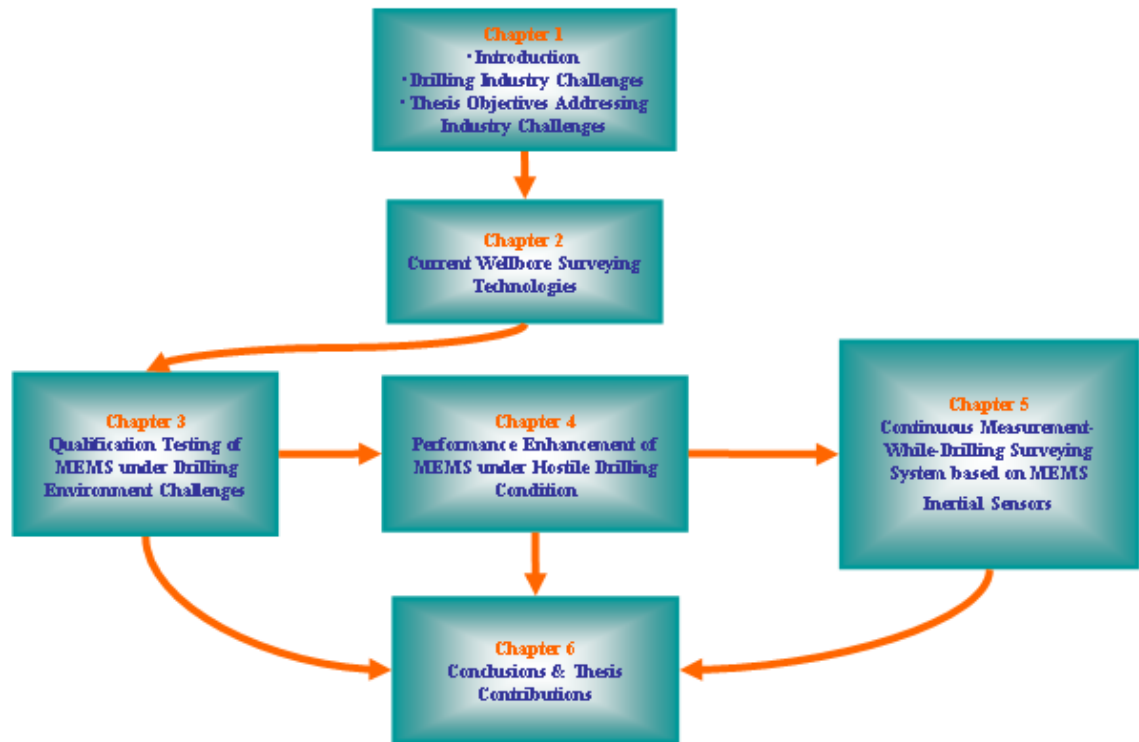


Figure 1.1: Dissertation Outline

CHAPTER TWO:

WELL BORE SURVEYING

TECHNOLOGIES

This chapter reviews current industrial technologies available for MWD and the RSS. MWD magnetic based technology and the various challenges that face magnetic sensors are discussed. In addition, this chapter presents an up-to-date development of the MWD gyroscope based technology and RSS technology and discusses the motivation for this study.

2.1 Hydrocarbon Well Life Cycle

All hydrocarbon wells share a similar life cycle [Bourgoyne et al., 2005]:

- Seismic data of the field of interest is acquired.
- The processed seismic images are interpreted and evaluated.
- A well trajectory that starts from the ground surface and extends to the desired hydrocarbon reservoir zone is designed.
- The well is drilled according to the designed well plan to reach the reservoir zone safely and efficiently. Three types of drilled wells are shown in Figure 2.1 and described below:

- a) In vertical wells the drilling rig is located on top of the reservoir zone.
- b) Deviated wells can be drilled to reach the hydrocarbon reservoir zone.
- c) Horizontal wells maximize hydrocarbon production.
- Wireline measurements are retrieved, including formation evaluation data. These provide an insight into how thick the reservoir is and how easy it will be to extract the oil or gas and send it to the surface.
 - The drilled well is cased and cemented in order to prevent collapse of the well bore and to create a barrier between the well walls and the flowing hydrocarbons.
 - The well is perforated by shooting holes into the wall of the well to enhance the oil flow up to the surface.

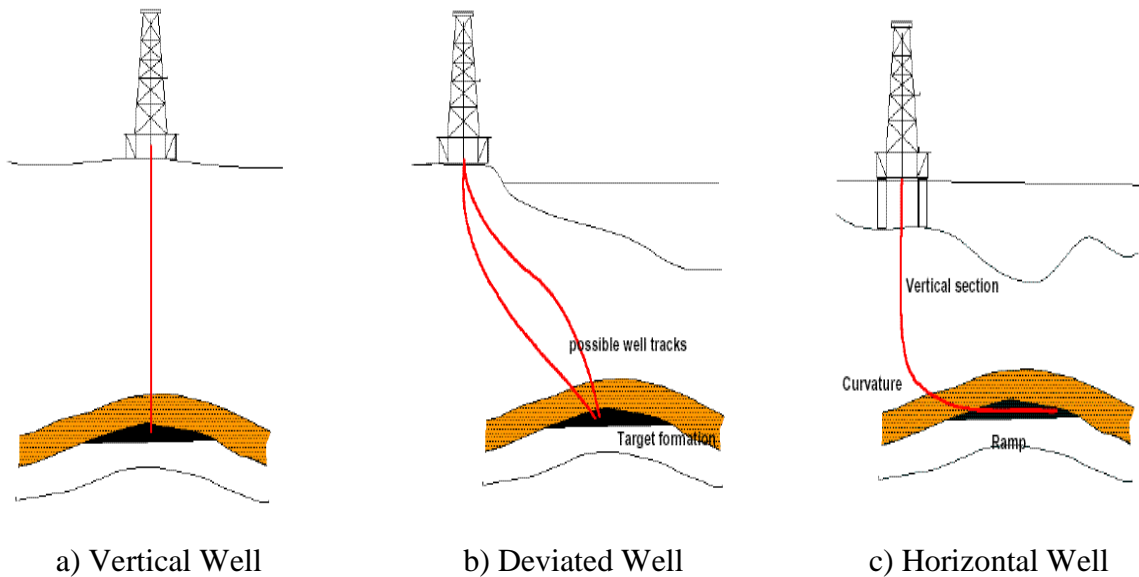


Figure 2.1: Drilling Well Types [Bourgoyne et al., 2005]

A drilling of any well bore starts at a surface location, which is represented by geographical coordinates. The well bore is drilled vertically to a kickoff point at a certain depth below the surface location. At the kickoff point directional drilling starts by deviating the well bore from the vertical direction according to the designed well profile. Information about the location of the bottom hole assembly (BHA) and its direction inside the well bore is determined by use of an MWD tool [Bourgoyne et al., 2005].

The BHA is a part of the drill string and consists of the following components in the same order:

- Drill bit;
- Drilling motor which can be a conventional positive displacement motor (PDM) with bent housing as shown in Figure 2.2 or a rotary steerable system (RSS);
- Stabilizer;
- MWD tool;
- Logging while drilling (LWD) tool;
- Drill collar;
- Drill pipe up to the surface.



Figure 2.2: Conventional PDM Motor behind the Drill Bit [Berger et al., 1999]

The MWD tool contains a direction and inclination sensor package in addition to a transmitter module that sends data to the surface while drilling. Interpretation of this data provides the necessary information to steer the well into the planned directions toward the target reservoir. Direction, inclination, and toolface are displayed at the driller console for this purpose. The available MWD tool takes downhole stationary surveys at regular intervals (e.g., 10 m), where each survey provides inclination and direction (azimuth) measurements at a given measured depth. Coordinates of the MWD tool in the well bore can then be computed using these measurements and the previous surveying station values for inclination, direction, and distance [Thorogood, 1989]. MWD sensors are crucial for drilling operations for three reasons:

1. To avoid collision with other wells in proximity, which can lead to a blowout of a well and a potential catastrophic impact on the environment;
2. To prevent crossing the boundary lines of leased land; it is extremely important to keep the well within the owner's legal boundaries;
3. To drill according to the designed well plan and hit the target reservoir providing a maximum contact area of the well through the reservoir.

In current directional drilling applications, the direction and inclination sensors package installed inside the MWD tools contains a set of three orthogonal accelerometers and a set of three orthogonal magnetometers [Thorogood, 1989]. The accelerometer measurements are first processed to compute the inclination and toolface angles of the MWD tool. The azimuth is then determined using the computed inclination and toolface angles and the magnetometer measurements [Russel and Russel, 1979]. The operation of magnetometers and their limitations are discussed in the following section.

2.2 Measurements-While-Drilling Magnetic Based System

2.2.1 Magnetometers

Present MWD tools employ three orthogonal fluxgate saturation induction magnetometers inside the direction and inclination sensors package [Bourgoyne et al., 2005] as demonstrated in Figure 2.3. The earth's magnetic field can be measured using magnetometers and the magnetic azimuth angle can be derived. Magnetometers require a nonmagnetic environment in order to function properly, as the measured azimuth is referenced to the magnetic north [Ripka, 2001]. Magnetometers are sensitive to the earth's magnetic field; each magnetometer has two primary coils and a pick up secondary coil surrounds the primary coils. An alternating current passes through the two primary coils; symmetrical voltage pulses are then generated in the secondary coil each time the AC current changes direction. However, if an external magnetic field exists, it can distort the voltage pulses in the secondary coil. The

magnetometer reacts by supplying a buckling current through the second coil to drive the voltage pulses back to their symmetric state. The magnitude of the buckling current is proportional to the earth's magnetic field strength and aligned to the axis of the magnetometers [Ripka, 2001].

The magnetic field at every location on earth has a specific strength and direction. The direction of the magnetic field line is defined by the dip angle, which is the angle between the magnetic field line and a line tangent to the earth's surface. Close to the earth's poles, the magnetic field line points down into or up out of the ground with a magnetic dip angle close to 90° . The magnetic field strength is significantly higher at the poles due to the fact that many magnetic field lines converge at the poles. At the earth's equator, the magnetic field lines are almost horizontal and point from magnetic north to magnetic south with a magnetic dip angle close to 0° . The magnetic field strength is weaker at the equator than at the poles as the magnetic field lines are more spread out.

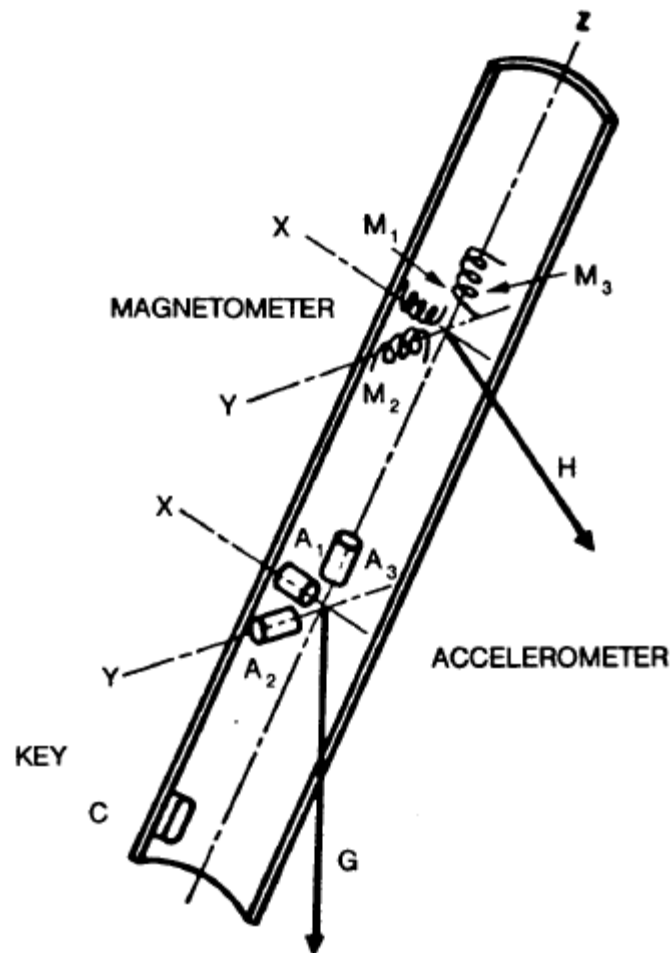


Figure 2.3: Arrangement of Sensors in an MWD Tool [Eickelberg, 1982]

The magnetic field strength has horizontal and vertical components. The horizontal component points from the magnetic north to the magnetic south, while the vertical component points down into or up out of the ground. We rely mainly on the horizontal component to calculate the magnetic azimuth direction of the BHA. The horizontal component is small close to the poles because the dip angle is close to 90° and most of the magnetic field is pointing down into the ground. This explains why errors introduced due to magnetic interference significantly affect magnetic azimuth

measurements. The opposite is true near the equator, where the total field strength is lower and the horizontal component is larger [Parkinson, 1983].

Three orthogonal magnetometers H_x , H_y , and H_z measure the components of the earth's magnetic field H along the x , y , and z axes, respectively. The magnetic azimuth of BHA can be derived by knowing the inclination and the toolface at this station; the magnetic azimuth of BHA is derived using accelerometer measurements with the following expression [Russel and Russel, 1979]:

$$A = \arctan\left(\frac{-(H_x \sin \phi + H_y \cos \phi)}{H_z \sin \theta + \cos \theta (H_x \cos \phi - H_y \sin \phi)}\right), \quad 2.1$$

where BHA inclination θ and toolface ϕ are derived using the three orthogonal accelerometer (f_x , f_y , and f_z) measurements as follows:

$$\theta = \arctan\left(\sqrt{\frac{f_x^2 + f_y^2}{f_z^2}}\right), \quad 2.2$$

$$\phi = \arctan\left(-\frac{f_y}{f_x}\right). \quad 2.3$$

The main advantage of using flux gate magnetometers is their solid state which allows them to sustain high vibration and shocks. Their electrical and environmental characteristics are presented in Table 2.1 [Lyons, and Plisga, 2005].

Table 2.1: Characteristics of a Flux Gate Magnetometer

Alignment	$\pm 0.5^\circ$
Scale Factor	5V / G $\pm 5\%$
Bias	± 0.005 G @ 25°C
Linearity	$\pm 2\%$ full scale
Vibrations	1.5 cm p – p, 2 to 10 Hz 20 g, 10 to 200 Hz
Shock	1000 g, 0.5 ms, 0.5 sine
Temperature	0 to 200°C

Any disturbance to the expected magnetic field value will lead to a significant deterioration of magnetic azimuth accuracy. Many factors contribute to such disturbance and this leads to a number of disadvantages of using magnetometers to determine the azimuth of the BHA. The following subsections summarize the challenges and error analysis of a MWD based magnetic azimuth in a drilling environment.

2.2.2 Magnetometer MWD Limitations

The most important challenge the current magnetometer MWD tools encounter is magnetic interference. Two types of magnetic interference disturb magnetometer

readings. The first is the drill string magnetic interference and the second is the external magnetic interference due to the surrounding environment.

2.2.2.1 Drill string magnetic interference

The drill string can be considered as a long slender magnet that has both ends acting as magnetic poles. As a result, drill string steel components become magnetized due to the presence of the earth's magnetic field lines. A magnetometer based MWD tool is therefore placed inside a nonmagnetic drill collar in an effort to eliminate this effect, but the nonmagnetic drill collar can only minimize the influence of the other steel components in the drill string [Thorogood, 1990; Grindord and Wolf, 1983]. As the inclination angle builds up from the vertical direction or the direction of the bore hole (azimuth angle) deviates away from the north-south direction, the effect of magnetic interference on magnetometer measurements due to the drill string increases significantly [Thorogood and Knott, 1989]. Drill string magnetic interference only affects magnetometer measurements aligned along the tool rotation axis, assuming the three magnetometers are orthogonal.

2.2.2.2 External magnetic interference

Unlike drill string magnetic interference that affects only one magnetometer, the external magnetic interference affects all three magnetometers in the triad. External magnetic interference can be introduced by the following:

- Presence of ferromagnetic material near the tool such as nearby casing collars of the previous section of the well or lost collars (fish) in the bore hole; sidetracking

around the fish is necessary in order to avoid this obstacle. Drilling close to either a casing or a fish greatly affects magnetometer measurements [Bourgoyne et al., 2005].

- Iron, pyrite, and hematite formations have magnetic characteristics which affect magnetometer measurements and lead to deterioration of magnetic azimuth accuracy [Bourgoyne et al., 2005].
- Solar storms can have a dramatic effect on the earth's magnetic field. These storms develop due to charged particles that escape from the sun and travel to the earth's upper atmosphere, significantly affecting the earth's magnetic field [El-Gizawy, 2003]. A less dramatic effect can be caused by the tidal motion of atmospheric gasses which produce a regular diurnal variation over a 24 hour period [Parkinson, 1983]. The variation in magnitude depends on the latitude of the affected point on the earth's surface, the season of the year, and the solar activity [Parkinson, 1983]. Solar storms and diurnal variations of the field greatly affect magnetic azimuth accuracy and hence magnetometer measurements must be corrected for these effects [Wolf and de Wardt, 1981; Thorogood and Knott, 1989].
- Drilling fluid can degrade the magnetic azimuth accuracy if it contains magnetized contaminants. Magnetic azimuth errors of 1–2 degrees have been reported under such conditions. In some unfavorable conditions, magnetic azimuth errors can be five to ten times larger for certain well bore directions [Wilson and Brooks, 2001; Torkildsen et al., 2004; Amundsen et al., 2008].
- When a nonmagnetic drill collar exceeds its magnetic tolerance, magnetic hot spots develop and the nonmagnetic drill collar has to be replaced [Zijsling and Wilson, 1989].

2.2.2.3 BHA sag effect

BHA sag refers to a misalignment along the MWD tool rotation axis and the well bore centre axis, where the MWD tool does not lie centrally inside the borehole. The MWD tool tends to lie on the low side of the borehole due to gravitational forces acting on the drill string. The sag relies on BHA design, number and sizes of stabilizers, position and degree of bend of the steerable motor, mud weight, and the borehole inclination angle. The effect of BHA sag on the direction and inclination sensors package can be significant and leads to a large system error especially in a wellbore with high inclination. Thus, measurements have to be corrected for this error [Berger and Sele, 1998; Ekseth, 1989].

2.3 Measurements-While-Drilling Gyroscope Based System

The word gyroscope is derived from the Greek words “gyro” which means revolution and “skopien” which means to view. A gyroscope measures angular velocity and is used for monitoring angular rotation along the sensitive axis of a MWD tool sensor. Gyroscope technology is used in some directional drilling applications, however, it is not utilized in RSS technology and it has limited use in MWD tools. The advantage of gyroscope technology is that interruptions in the earth’s magnetic field or surrounding magnetic interference has no effect on gyroscope performance. At present, gyroscopes are utilized in the following three applications.

2.3.1 In Hole Orientation Gyroscope Tool

The gyroscope is used to orient packers and whipstocks at the kickoff point in order to deviate from the existing casing into the oriented direction. Gyroscopes have to be used in this orientation process due to the failure of the magnetometer to provide an accurate azimuth. This is expected since the presence of a steel casing in the bore hole at the kickoff point affects magnetometer readings. It was reported that using a gyroscope as a reference tool to the magnetometer based MWD improves survey accuracy and reduces the lateral position uncertainty from 60 meters to 24 meters at the end of a well with a true vertical depth (TVD) of 3000 meters [Thorogood and Knott, 1990]. In spite of this, a considerable delay time is incurred by following this process. Each time the gyroscope reference tool is needed, drilling has to stop to run the tool to the bottom of the well using a wire to take surveys. The gyroscope is pulled out of the well as soon as the surveys are taken. Directional drilling can then commence relying on the magnetic based MWD tool in the bottom hole assembly.

2.3.2 Wireline Gyroscope Tool

Well bore mapping is achieved using a wireline gyroscope tool. It is needed after drilling of a certain section of the well is accomplished in order to make an accurate survey of the well and to evaluate the formation data. The entire drill string is pulled out of the bore hole, and then the wireline gyroscope tool is run into the bore hole using a wireline. One end of the wireline is anchored at the surface on the drilling rig floor or on a logging truck bed. The other end carries the gyroscope tool that runs in

the well to take the measurements [Lyons and Plisga, 2005]. The tool surveys the entire well bore section using one of the following two methods:

- In the gyro-compassing mode, the gyroscope tool is lowered in the bore hole to take stationary surveys at predetermined depths. This mode utilizes three accelerometers and either a single axis or dual axes north-seeking mechanical gyroscope with a low drift rate of $0.1^\circ/\text{h}$ [Kelsey, 1983; Noy and Leonard, 1997]. The well bore trajectory is computed based on azimuth and inclination angles at the stationary survey stations with an assumption of the trajectory geometry. The use of this mechanical type gyroscope achieves a satisfactory accuracy of 1 meter in vertical depth and 100 meters in lateral directions for a well of 3000 meters of TVD [Noy and Leonard, 1997]. However, the accuracy of mechanical gyroscopes is unacceptable in MWD applications.
- The continuous mode is based on deriving the well bore trajectory as the wireline gyroscope tool runs in the borehole. This is accomplished by integration of the measured azimuth, inclination, and toolface increments. Two fixtures of sensors are recognized. The first fixture includes three accelerometer and two mechanical gyroscopes in a gimballed structure to maintain a leveled stationary platform [Wright, 1988; Uttecht and deWardt, 1983]. The second fixture is based on the inertial navigation system and consists of three orthogonal accelerometers and three orthogonal mechanical or ring laser gyroscopes [Hulsing, 1989; Stephenson and Wilson, 1992]. A size limitation prevents the use of similar fixtures in MWD technology.

2.3.3 Single-Axis Gyroscope Based MWD Tool

The immense advantage of using gyroscopes instead of magnetometers for measuring the well bore direction makes this technology highly desirable, especially while drilling. Some of the limitations of using gyroscope technology while drilling are the large size of the instrument, the gyroscope's vulnerability to shocks and vibrations, and the inaccuracy of gyroscope measurements. These limitations are addressed in this research study.

Recent research has investigated three types of gyroscope sensors to be employed in MWD tools. They are the mechanical based gyro (MBG), the ring laser gyro (RLG), and the FOG. Performance of the MBG is unacceptable due to moving parts that are susceptible to shock and vibration while drilling. The RLG is a navigation grade gyroscope used mainly in commercial and military aircraft as a primary navigation sensor due to the high accuracy and the relatively small error drift rate of this sensor. The RLG gyroscope sensor is expensive and has limited use because its large size makes it difficult to install inside the MWD tool collar. Cost and size restrict the use of RLGs in measurement-while-drilling applications [Estes and Epplin, 2000]. The FOG is relatively smaller than the RLG, and the FOG's susceptibility to shocks and vibrations is lower than that of the MBG. However, a complete set of three orthogonal FOGs cannot be installed in a MWD tool collar due to the size of the instruments. Efforts have been made to solve this problem by using a single axis gyroscope with a dual axes gyroscope in MWD applications [Noureldin, 2002; Binder et al, 2005].

A single axis FOG gyroscope is integrated with three orthogonal accelerometers in order to continuously measure the azimuth, toolface, and inclination of the well bore. This provides a continuous well trajectory while drilling. The location of the single FOG gyroscope installed inside the bearing assembly is shown in Figure 2.4. It is based on the assumption that the changes in inclination and toolface are very small if they are monitored at a high rate. Because the sensitive axis of the gyroscope is along the MWD tool rotation axis, the tool can only detect the tool direction while the bore hole is vertical or nearly vertical. If the bore hole inclination is more than 20° , the single axis FOG cannot resolve the azimuth change along the sensitive axis. Stationary based surveying is suggested for the highly inclined section of the well bore [Noureldin et al., 2001].

A single axis gyroscope based MWD tool is designed under the assumption that the rate of penetration of the drill bit is small and the inclination build up rate angle is within a range of $10^\circ/\text{h}$. In faster drilling formations, the inclination build up rate angle can reach up to $40^\circ/\text{h}$ [Joshi and Ding, 1990]. The single axis gyroscope MWD tool cannot be relied on in such a condition [Noureldin, 2002]. In summary, a single axis gyroscope MWD tool is limited to drilling a bore holes in vertical and near vertical directions, with slow build up rate angles.

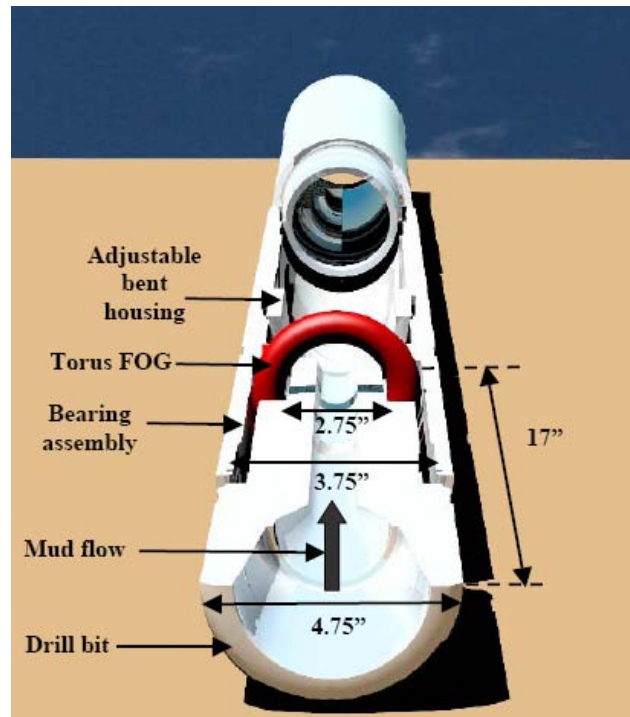


Figure 2.4: Single FOG Installed inside the Bearing Assembly [Noureldin, 2002]

2.3.4 Dual-Axes Gyroscope Based MWD Tool

An MWD tool with a dual-axes spinning mass gas bearing rate (GBR) gyroscope with a stepper motor-driven indexing mechanism has been developed [Estes and Epplin, 2000]. A limitation of this tool is the use of an indexing motor in order to rotate the gyroscope around its spin axis. The motor moves the sensors chassis to a set of positions to estimate the run to run bias of the sensor measurements. Field tests failed due to the failure of the indexing motor, where a coupling fracture between the indexing motor and the sensor chassis prevented the motor from rotating properly [Estes and Epplin, 2000]. A stationary based surveying technique was implemented at certain stations. The tool was not able to provide continuous azimuth, inclination, and toolface measurements while drilling, which imposed another limitation. A third

limitation is that dual-axes gyroscopes cannot resolve well bore azimuths for horizontal drilling; this is a problem when the inclination is 60° and higher [Estes and Epplin, 2000].

Another implementation of dual-axes gyroscopes MWD tools has been proposed, but with the use of two FOGs instead of GBR gyroscopes. The sensitive axes directions of accelerometers and gyroscopes inside the drill collar are presented in Figure 2.5. The study proposed an improved algorithm to derive the continuous azimuth at highly inclined and horizontal sections of the well [Noureldin, 2002]. This was accomplished by changing of the gyroscopes body axes orientation at high inclination sections.

In a different study, two dual-axes gyroscopes were integrated with three orthogonal accelerometers. However, the gyroscopes were arranged in the cross-section plane of the borehole, and an inclinometer system with a transverse gyroscope was developed [Binder, et al., 2005]. An indexing motor was utilized in the research to calibrate the gyroscope at surveying stations. The motor rotates the gyroscopes' housing about two mutually perpendicular axes. The last two studies have not been field tested yet.

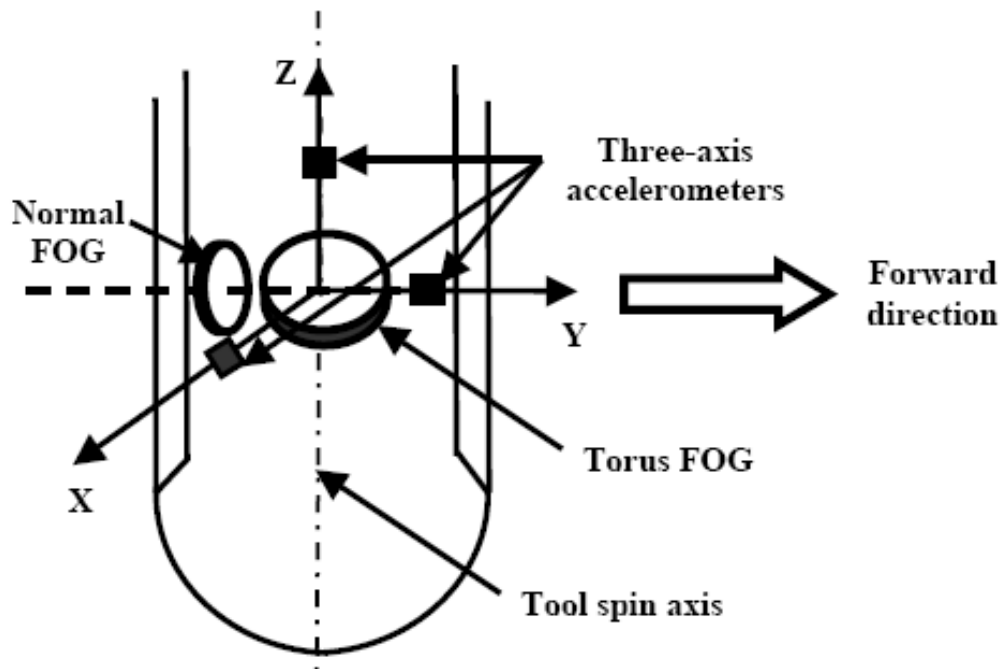


Figure 2.5: Dual-Axes Gyroscope MWD Tool [Noureldin, 2002]

2.4 RSS Technology

2.4.1 RSS Overview and Advantages

The rotary steerable system is a recent technology that allows drilling at faster rates by rotating the entire drill string all the time. This differs from conventional technology that uses a PDM with a bent housing to provide a side force to the bit to deflect the well bore in the desired direction. In conventional technology, drilling is done in sliding and rotary modes. A sliding mode is defined when the entire drill string is not rotating and only the drill bit is rotating. This takes advantage of the bent housing in the PDM to divert the well bore to a desired direction. As soon as the well bore direction and build angle are established, drilling enters into a rotary mode where the entire drill string rotates to hold direction.

The sliding mode is considerably slower than the rotary mode and is associated with many problems. The emerging RSS technology is highly desirable because it completely eliminates sliding problems and has several additional advantages [Edmondson et al., 2000]. RSS can:

- Increase the rate of penetration of the drill bit to allow faster directional drilling;
- Help optimize drilling parameters such as weight on bit and revolutions per minute (RPM), which optimizes drilling operation;
- Improve the wellbore quality and provide an in gauge hole with no ledges; it also reduces wellbore tortuosity [Weijermans et al., 2001];
- Reduce the torque and drag that cause fatigue of the drill string;
- Provide better wellbore cleaning, where the continuous rotation of the drill string agitates wellbore cuttings in the annulus; this facilitates moving the cutting out of the hole. If using the conventional PDM, additional wiper trips are needed for the hole cleaning after drilling is completed. Therefore, RSS eliminates the additional time required for wiper trips.
- Eliminate the time of the toolface orientation at each tool joint when using the conventional PDM;
- Eventually decrease the cost per foot of drilling operations.

An RSS can turn the wellbore while rotating by pushing or pointing the bit toward the desired direction using a shaft drive attached to the bit. Each directional drilling

service company has a unique design to mechanically control the bit direction while drilling.

2.4.2 RSS Challenges

Recent advances in RSS technology increased the demand for the use of MWD technology for directional control of the well bore. However, the RSS is installed directly behind the bit followed by the MWD tool. This leads to an offset of at least 15 meters between the current MWD surveying sensors package and the bit, as shown in Figure 2.6. The average drill bit length is 300 mm and the average length of an RSS (Figure 2.6, C) is 8 meters. The flex sub (Figure 2.6, B) and the spiral stabilizer extend for 6 to 9 meters. The MWD collar (Figure 2.6, A) length is approximately 9 meters. The surveying sensor package is usually installed on the lower part of the MWD tool collar.

Under these conditions drilling proceeds blindly for 15 meters, and the directional driller has to wait to drill 50 feet to know the location of the wellbore. An average formation can be drilled at a rate of 10 ft/hr, this counts for 5 hours of drilling blindly. This leads to a high cost if the wellbore is diverted significantly from the planned trajectory especially for offshore operations.

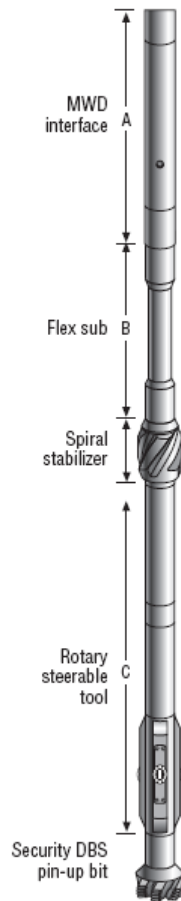


Figure 2.6: MWD Tool Installed behind RSS [www.halliburton.com]

Additionally, MWD tools available in the market cannot provide a continuous wellbore trajectory while drilling. Furthermore, the MWD tool does not communicate its measurements to the RSS while drilling. If the RSS does not deviate in the correct direction, drilling has to stop and different commands have to be down-linked to the RSS. This is indeed very time consuming and imposes constraints on the use of an RSS. Thus, the full advantages of the RSS are yet to be realized with the present implementation. This shortcoming of the current technology has motivated this research study.

2.5 Proposed Integrated RSS Technology

The aforementioned challenges of the current technologies available for the hydrocarbon drilling industry and the potential for significant improvements have motivated this research study. It aims to develop an integrated solution to enhance directional drilling by integrating an RSS with MWD direction and inclination sensors and packaging the two systems into one collar installed less than 1.5 meters behind the drill bit. This study proposes an advanced direction and inclination sensor package based on the inertial navigation system (INS).

The strict size limitation inside the RSS collar makes MEMS inertial sensors perfect candidates for this application. However, the small size of MEMS inertial sensors comes with a trade-off of lower measurement accuracy. The achieved accuracy of MEMS inertial sensors is discussed in later parts of this dissertation. The following two chapters present qualification testing of the MEMS inertial sensors in harsh shock and vibration environments and proposes an algorithm to mitigate the effects of severe shock and vibration on inertial sensors' measurements.

CHAPTER THREE:

SHOCK AND VIBRATION

CHALLENGE WHILE DRILLING

In today's market, the main cause of failure for MWD tools and the RSS is shock and vibration experienced downhole. This costs millions of dollars in repairs and nonproductive rig time [Akinniranye et al., 2007]. Gyroscopes and accelerometer sensors are very challenged during the drilling operation due to the harsh environments they have to survive in. Yet, they are expected to perform efficiently and monitor the way the BHA penetrates downhole. Additionally, shock and vibration disturbances should be isolated from other motion dynamics before processing sensor measurements with the INS mechanization algorithm. It is reported that the drilling environment, more than any other application, exposes electronic systems and sensors to severe shock and vibration [Steinberg, D. S., 2000].

The small size of MEMS sensors allows them to fit inside MWD or RSS tools. The ability of MEMS to perform under high shock and vibration motivated this research. We test MEMS inertial sensors in the following ways. First, we expose these sensors to harsh conditions and see if they continue to provide data throughout the

experiments. Second, we analyze the performance of the MEMS-based inertial measurement unit (IMU) in severe shock and vibration environments. Finally, we evaluate the effects of the surrounding environment on the MEMS inertial sensors' measurements. Additionally, we explore advanced signal processing techniques to enhance sensor performance and provide accurate inclination, toolface, and azimuth measurements of the drill bit at all times during drilling operations.

3.1 Characteristics of MEMS Inertial Sensors

Micromachined inertial sensors are of special interest to the automotive and biomedical industries, navigation guidance systems, robotics, vibration monitoring, seismic sensing, and military applications [Yazdi et al., 1998]. This is due to the small size, rigidity, and low cost of MEMS sensors. MEMS inertial sensor operation is based on Newton's laws. The accelerometers measure acceleration using Newton's second law of motion "the net force on an object is equal to the mass of the object multiplied by its acceleration." This law can be expressed as:

$$F = ma, \tag{3.1}$$

where a is the acceleration produced by force F in addition to the gravity acceleration, and m is the mass of the object under force [Titterton and Weston, 1997].

Three orthogonal accelerometers measure the drill bit acceleration along three orthogonal directions. Another three orthogonal gyroscope sensors measure the rotational motion with respect to an inertial reference frame, and thus are used to map

or transform the measured orthogonal accelerations in the inertial reference frame direction. The continuous position of the drill bit can then be derived by double integration of the projected accelerations on the inertial reference frame. The derived position accuracy is highly dependent on the accuracy of the inertial sensors, which is quantified relative to the following characteristics [Titterton and Weston, 1997]:

- **Bias:** consists of deterministic and random components. Deterministic components represent the offset of the sensor measurement from the true value, while the random components are known as the bias drift that accounts for the rate of error accumulation over time. Sensor calibration cancels the effect of the deterministic bias, and stochastic modeling minimizes the random bias.
- **Measurement Scale Factor:** represents the relationship between the output signals (usually measured in volts) and the true physical quantity (e.g., acceleration, angular acceleration). The scale factor has a unit of parts per million (ppm) and can be determined through a calibration process. The term “scale factor stability” or “nonlinearity” of the scale factor error is used to refer to any expected variation of its value during the run.
- **Output Stability:** refers to any variation of accelerometer bias or gyroscope drift during the same run or from run-to-run.
- **Thermal Sensitivity:** describes variation of the sensors’ bias or scale factor errors due to a change of temperature.
- **Shock Survivability:** shocks can lead to permanent damage of the sensor. Therefore sensors have to be qualified to make sure they are able to survive under shocks, especially for drilling applications.

- **Vibration Effect:** errors introduced due to vibrations. Minimizing such errors is essential. Errors can be detected by analyzing the noise characteristics of sensor signal output in a vibration environment.

This chapter investigates the shock survivability of and vibration effects on MEMS sensors during drilling operations. Three MEMS gyroscopes (ADXRS150) and three MEMS accelerometers (ADXL105) manufactured by Analog Devices Inc. were tested under severe shock and vibration in a testing facility located in Houston, Texas. The unit was developed by members of the mobile multisensor research group at the University of Calgary [El-Sheimy and Niu, 2007]. The gyroscopes operate on the principle of a resonator gyroscope, while the accelerometers are polysilicon surface micromachined sensors [Yazdi et al., 1989]. Performance characteristics of the gyroscopes and accelerometers are summarized in Table 3.1.

Table 3.1: Characteristics of MEMS Sensors Manufactured by Analog Devices Inc,

Parameter	Gyroscopes (ADXRS150)	Accelerometers (ADXL105)
Range	$\pm 150^\circ/\text{s}$	$\pm 5 \text{ g}$
Scale Factor	12.5 mV/(deg/s)	250 mV/g
Nonlinearity	0.1% of SF	0.2% of SF
Bias	+2.5 V \pm 0.3V	+2.5 V \pm 0.625V

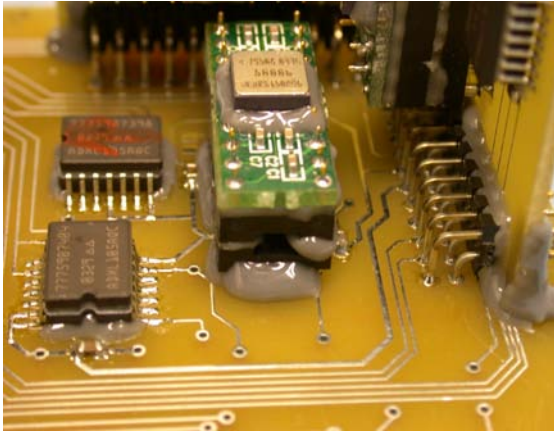
Noise	0.05°/s/√Hz	0.225 mg/√Hz
Bandwidth [2]	40 Hz	32 Hz
Temperature	8.4 mV/C;	8 mV/C;
Sensor	2.5V@25C	2.5V@25C
Power	+5V ± 0.25 V/25mA	
Temperature	-40 to +85 C	

3.2 Direction and Inclination Package Preparation

MEMS inertial sensors were placed in a special package filled with Nusil foam in order to absorb and reduce shocks and vibrations. This is illustrated in Figure 3.1. Packaging plays an important role in protecting gyroscopes and accelerometers from damage due to shock and vibration. The following is the procedure for packing and stacking the sensor package:

- Shield all sensitive electronic components, including MEMS sensor connections, with the electronic board as illustrated in Figure 3.1a and b.
- Install the inertial measurement unit (IMU) board inside the package and use a foaming material to support the electronic boards along the edges as shown in Figure 3.1c. This significantly reduces the transmission of vibrations and shocks to the IMU board.
- Seal the IMU package with the IMU board inside.
- Inject Nusil foam inside the package through various holes on the surface as in Figure 3.1d.

- Allow the injected foam to cure for 5 hours at 85°C. The IMU package is now ready for testing in harsh drilling environments.



a)



b)



c)



d)

Figure 3.1: MEMS Inertial Measurements Unit Stacked and Foamed before Testing

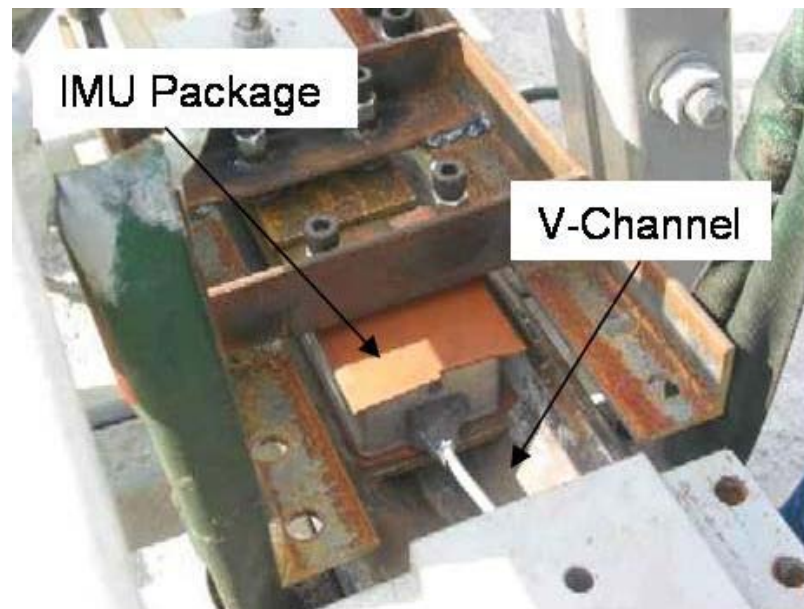
3.3 Shock Qualification Testing

Shock is a large impulsive force that acts for a very short period. Shocks are common while drilling and result from the impact of the drill bit while cutting into the hard

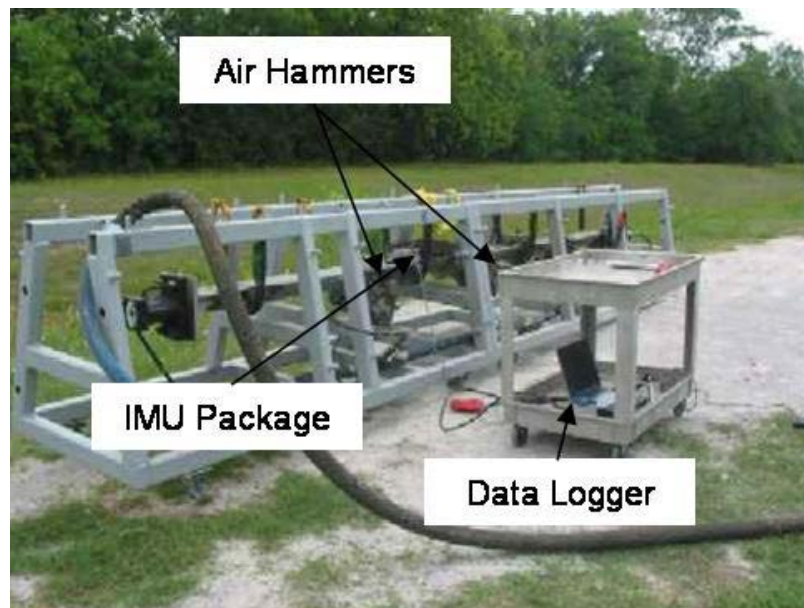
formation [Thomson, 1965]. It is an industry standard to qualify any proposed electronics or sensors under the drilling environment. This test was conducted at an oil service industry partner testing facility in Houston, Texas following procedures similar to those used to qualify the MEMS sensors under severe shock. MEMS sensors were exposed to severe shock forces of 1400 g over 0.017 s at a frequency of 3400 vibrations per minute (vpm) for 4 h. Sensors that were fully functional at the end of this test were qualified to be used in drilling applications.

3.3.1 Test Setup

A steel V-beam with 8 attached air hammers is used for this test. The air hammers (model BH3, manufactured by NOVAC) are pneumatic vibrators that operate using air pressure. The action of the piston in a pneumatic piston vibrator generates high amplitude repetitive impulse with unidirectional force when the piston strikes the base of the bore sharply on each cycle. Therefore, three air hammers are attached on each side of the V-beam and one is attached at each end. This guarantees that the shock forces act along the three orthogonal axes of the sensors. The MEMS sensors package was installed on a V-beam as shown in Figure 3.2a. Cables and air hoses are all checked and made ready for the test.



a)



b)

Figure 3.2: a) IMU Installed in the V-Channel; b) Shock Test Fixture

3.3.2 Sensors Qualification under Drilling Shock

An air pressure of 60 psi is applied to the air hammers for a period of 4 hours, with a piston area of influence of 52.5 inch². The pressure is defined as the acting force per unit area; thus the acting force can be computed as:

$$\begin{aligned}
 F &= P \times Ar = 60 \text{ psi} \times 52.5 \text{ inch}^2 = 3150 \text{ lbf} \\
 F &= 3150 \text{ lbf} = 14011.9 \text{ N} = 1401.19 \text{ g} \approx 1400 \text{ g}
 \end{aligned}
 \tag{3.2}$$

The air vibrator has an impacting frequency of 3400 vpm, which translates into an impacting time of 0.017 sec. The MEMS sensors were subjected to a physical shock of 1400 g at 3400 vpm for 4 hours. Accelerometer measurements throughout the test are presented in Figure 3.3. Shock forces were applied 6 minutes after the beginning of the test in order to compare viability of the sensors before and after applying the shock forces. As soon as the shock forces began, constant biases with magnitudes of 2.5 g, 2 g, and 1 g appeared in the measurements of accelerometers x, y, and z, respectively. The bias magnitudes were dependent on the sensor axis of orientation; sensors x and y were exposed to more shock forces and hence contained higher bias values. Furthermore, it was noted that high frequency components contaminated the background of the measurements.

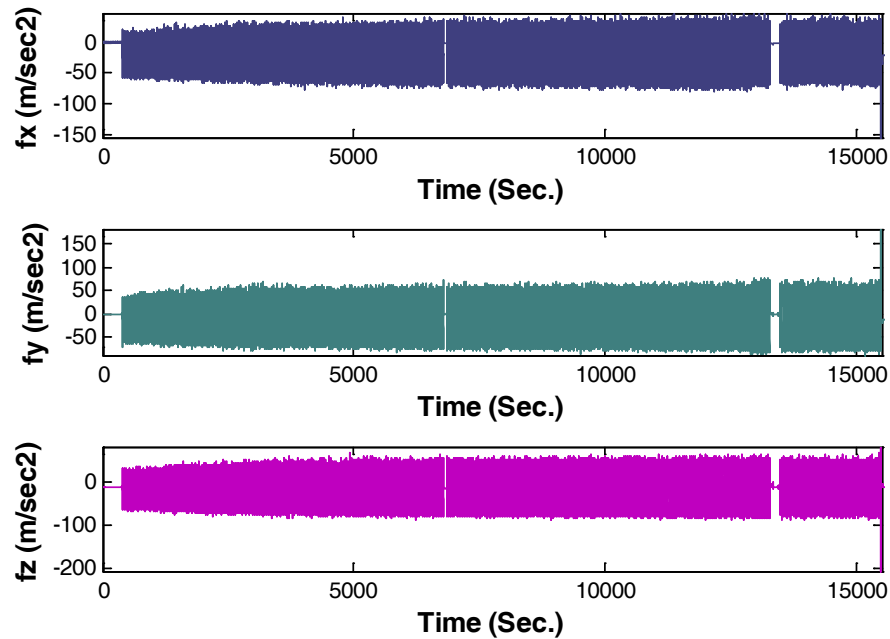


Figure 3.3: Orthogonal Accelerometers Measurements under 1400 g Shocks

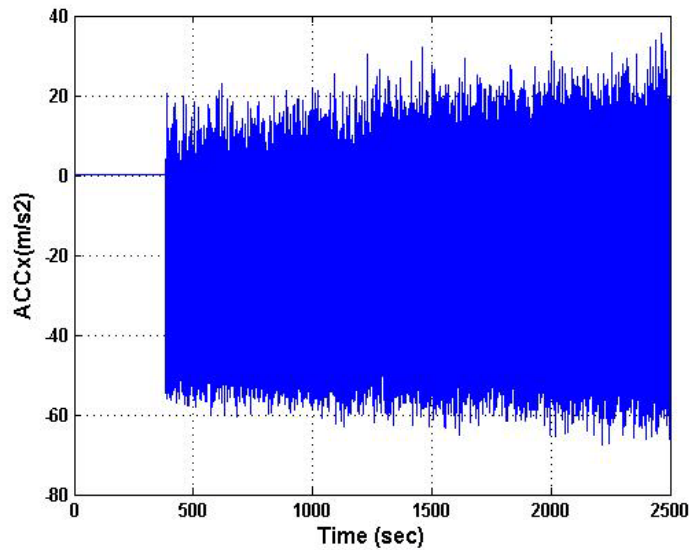
The sensor package and the v-channel were inspected every 30 minutes for damage during the test. There were two occasions when the pressure of air hammers of the test fixtures restarted due to loose air hoses. The two occasions can be observed in Figure 3.3 at $t = 6780$ sec and $t = 13260$ sec. The sensors are considered rugged enough for drilling applications if during and after the test they show no damage and are still fully operational. Fortunately, the sensors survived the entire test and were fully functional at the end of the test. This qualified the MEMS sensors to perform under drilling shock. However the effect of the shock forces on the sensor measurements had to be examined and analyzed in order to mitigate their effects. The next section provides a detailed analysis of the sensor measurements under severe drilling shock.

3.3.3 Analysis of Shock Impact

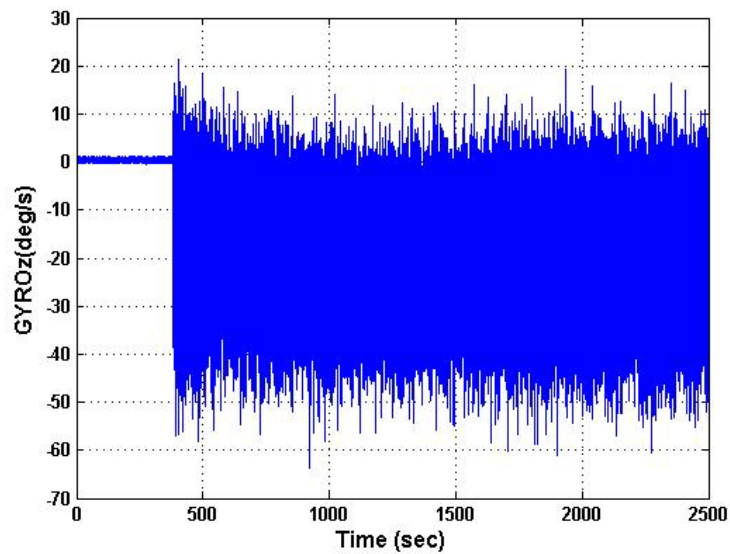
The shock test was repeated for a period of one hour at different shock forces in order to allow a thorough analysis of various scenarios. A total of 5 tests was conducted where air hammer pressure was set to 20 psi, 30 psi, 40 psi, 50 psi, and 60 psi. This corresponds to shock forces of 467 g, 700 g, 934 g, 1167 g and 1400 g, respectively. For each test, raw measurements at 200 Hz were logged while the MEMS sensors were under shock forces, and were examined in the frequency domain. Six channels of measurements were run simultaneously. Three channels represented the three orthogonal accelerometers, and three channels represented the three orthogonal gyroscopes. The accelerometer measurements channel in the forward direction (x-axis) was selected for this analysis along with the gyroscope measurements of the up direction (z-axis). These two channels had the most shock forces impact. The accelerometer in the forward direction was aligned on the horizontal plane where the shock forces had the maximum magnitude. This accelerometer senses the linear acceleration in the forward direction along the horizontal plane. Similarly, the up direction gyroscope senses the rotation rate due to shock forces along the horizontal plane.

Raw measurements of selected accelerometer and gyroscope channels are presented in Figure 3.4 for the shock test of 1400 g. The plots represent the first 2500 seconds (41 min) of the test. The test began with a stationary period of 381 seconds (6.35 min). The shock forces were then applied and their effects can be noted in Figure 3.4. The

demonstrated shock impact is an accurate representation of the impulsive forces that transfer along the drill string to inertial sensors and are produced while the drill bit grinds through the hard formation.



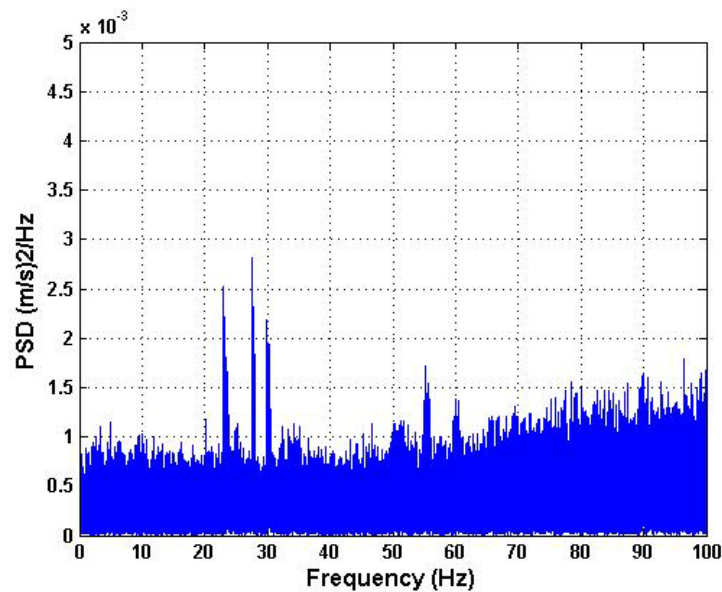
a) Accelerometer X – Channel



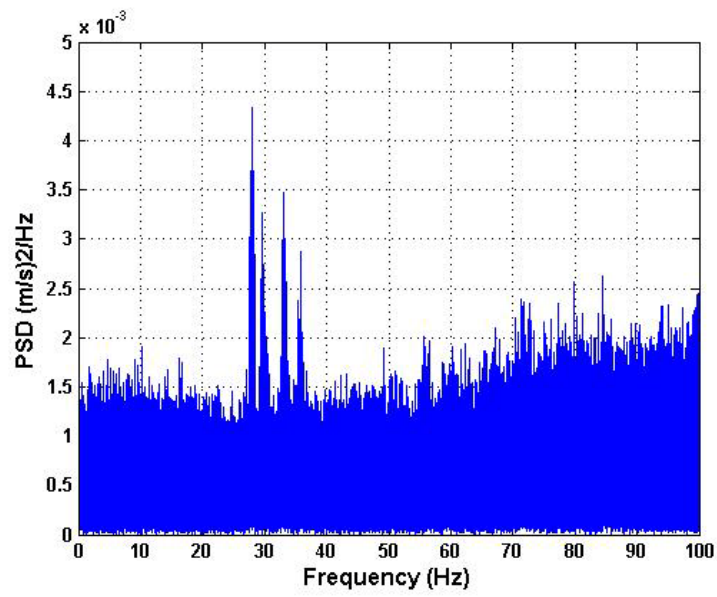
b) Gyroscope Z- Channel

Figure 3.4: Raw Measurements of Two Channels

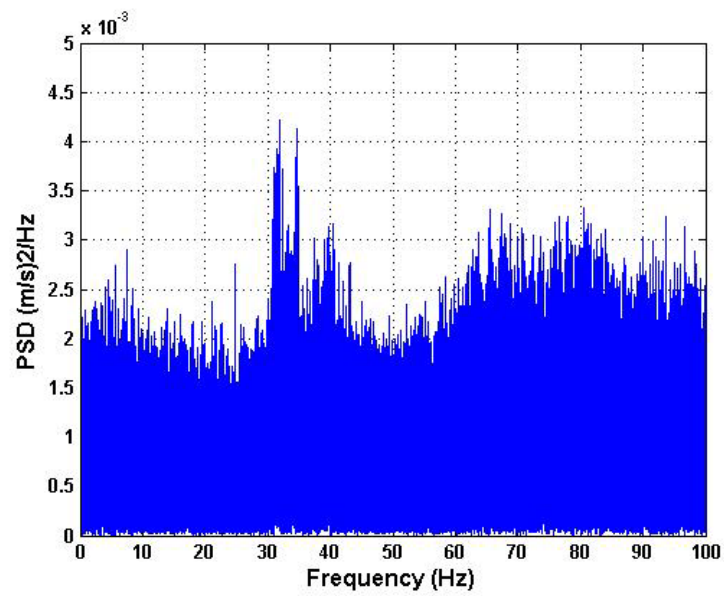
The mixed frequency components were analyzed in order to better characterize the shock effects on the sensor measurements. The power spectral density (PSD) analysis was employed for this purpose. The PSD represents the signal spectral decomposition in the frequency domain. In other words, it describes how the signal power is distributed with frequency. This allows a better understanding of shock effects on sensor signals while drilling. The PSD was derived for the forward accelerometer and the upward gyroscope signals while applying different shock forces, and the results are presented in Figure 3.5 and Figure 3.6, respectively. The computed PSD was normalized with a maximum of $9.2809 \times 10^{+006}$ (m/s)²/Hz for accelerometer measurements and a maximum of $7.9867 \times 10^{+006}$ (deg/s)²/Hz for gyroscope measurements.



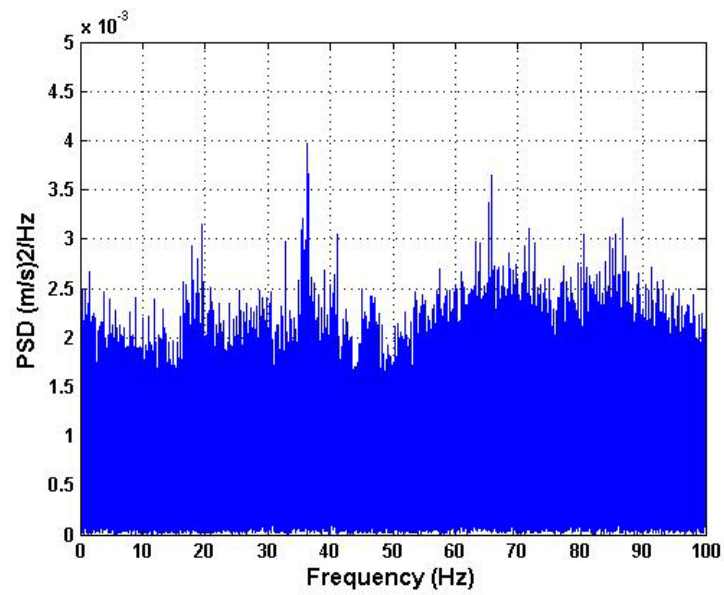
a) Shocks of 467 g



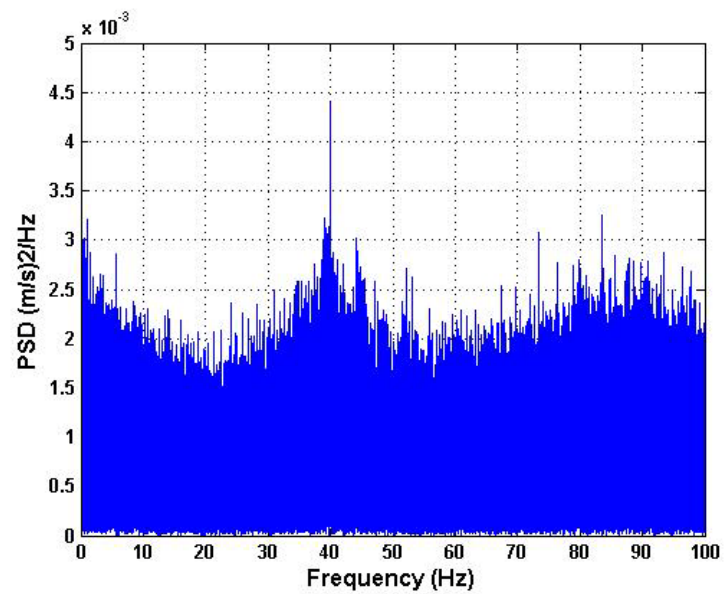
b) Shocks of 700 g



c) Shocks of 934 g



d) Shocks of 1167 g

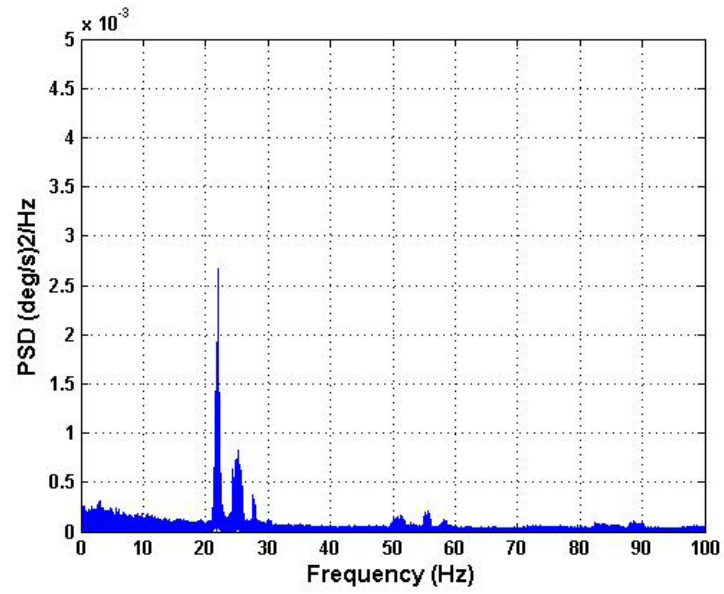


e) Shocks of 1400 g

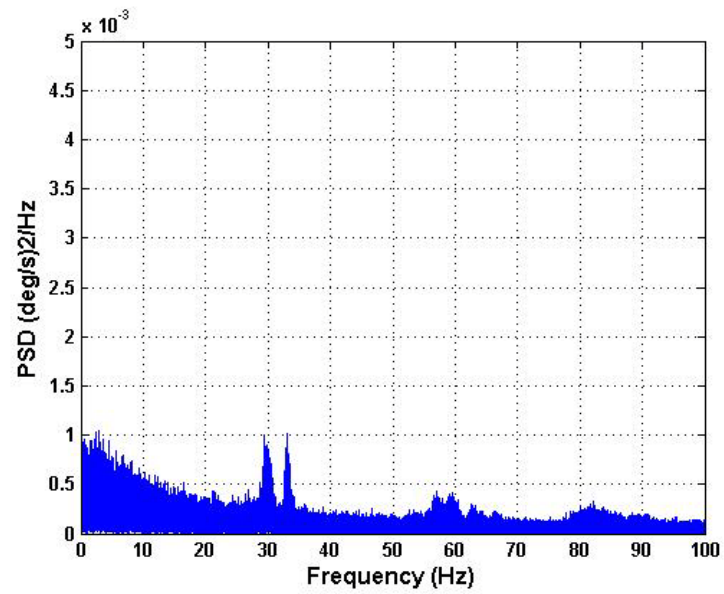
Figure 3.5: PSD of Forward Accelerometer Measurements at Different Shock Levels

By examining Figure 3.5 and Figure 3.6 it can be determined that the shock forces are manifested in both accelerometer and gyroscope measurements as:

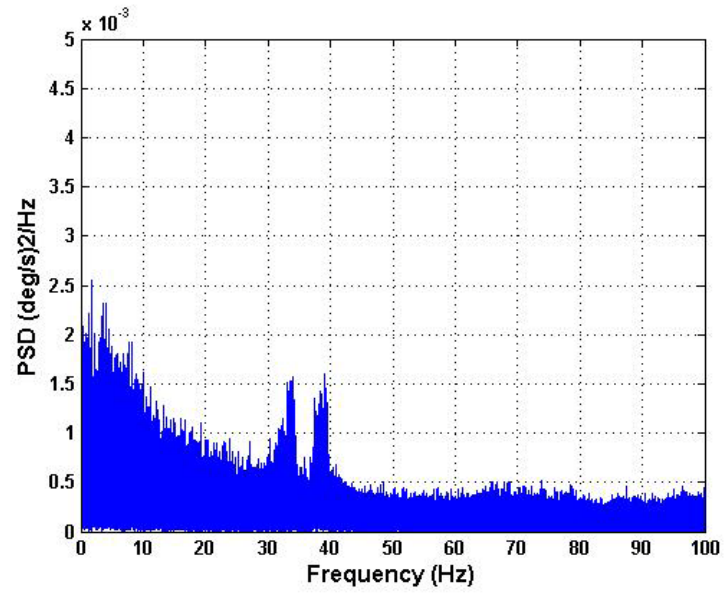
- Frequency components (sharp peaks) that depend on the magnitude of the applied shock forces. These components exist between 30 Hz and 40 Hz for the accelerometers and between 20 Hz and 45 Hz for the gyroscopes. The magnitude and the frequency of these components differ from one shock force to another. They agree in a frequency range that is high compared to the range of frequencies expected from the motion dynamics experienced while the drill bit penetrates the downhole formation.
- Background noise that has disturbance of relatively high magnitude and broadband characteristics. Both gyroscope and accelerometer measurements were highly contaminated with this broadband noise along the entire frequency spectrum. The increase in shock forces led to an increase of background noise for both accelerometer and gyroscope measurements. Filtering or separation of the background noise becomes essential under these conditions. Slow drilling rates of 10 ft/hr make a separation of such effects rather challenging using traditional techniques. In chapter 4 a proposed signal processing technique based on wavelet analysis was applied to these measurements to limit their effects.



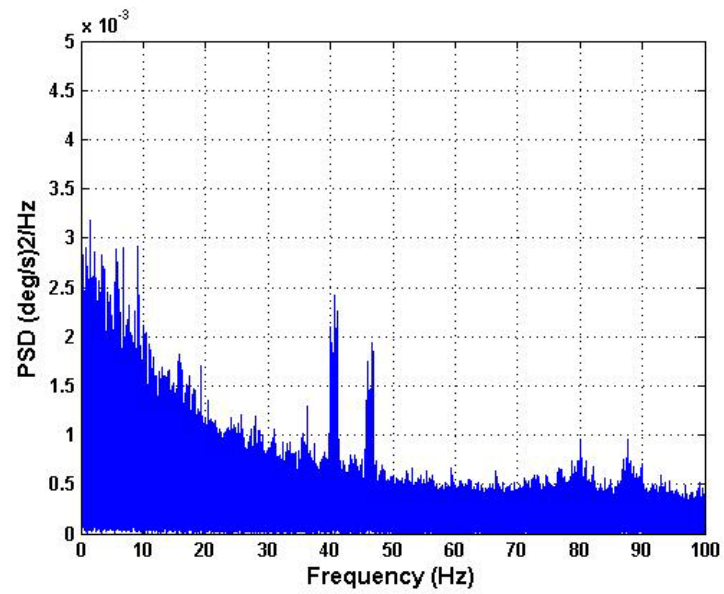
a) Shocks of 467 g



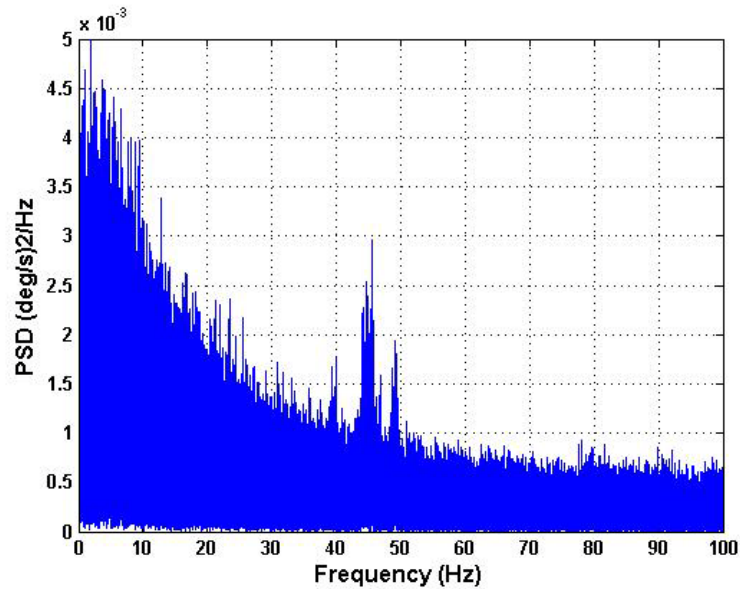
b) Shocks of 700 g



c) Shocks of 934 g



d) Shocks of 167 g



e) Shocks of 1400 g

Figure 3.6: PSD of Upward Gyroscope Measurements at Different Shock Levels

3.4 Vibration Qualification Testing

Vibration while drilling is produced from two main sources. The first source is the mud pump that circulates the drilling fluid through the hollow drill string and out of the annulus. The mud pump vibration produces a noise with a sinusoidal harmonic nature that can easily be detected and modeled. The second source of vibration results when the drill bit grinds through the formation to drill and results in three types of vibrations [Lyons and Plisga, 2005]:

- Vibration along the tool rotation axis results from bouncing of the drill bit on the bottom of the hole.
- Transverse vibration in a direction perpendicular to the tool rotation axis is produced from the drill string buckling or the mechanical resonance.

- Angular vibration results from the side biting of the stabilizers on the well walls.

In this qualification test, the MEMS gyroscopes and accelerometers were tested under conditions similar to the drilling vibration environment. A horizontal vibration table was employed to produce vibrations in the horizontal plane. Sensors are qualified for drilling application only if they survive the test and are fully functional at the end of the test.

3.4.1 Test Setup

MEMS sensors were tested under conditions similar to vibration conditions observed while drilling. The test was conducted at an oil service company testing facility. Vibration was generated using a vibration test table manufactured by Team Corporation with maximum frequency of 500 Hz. The MEMS sensor package was installed on the horizontal vibration table as illustrated in Figure 3.7.

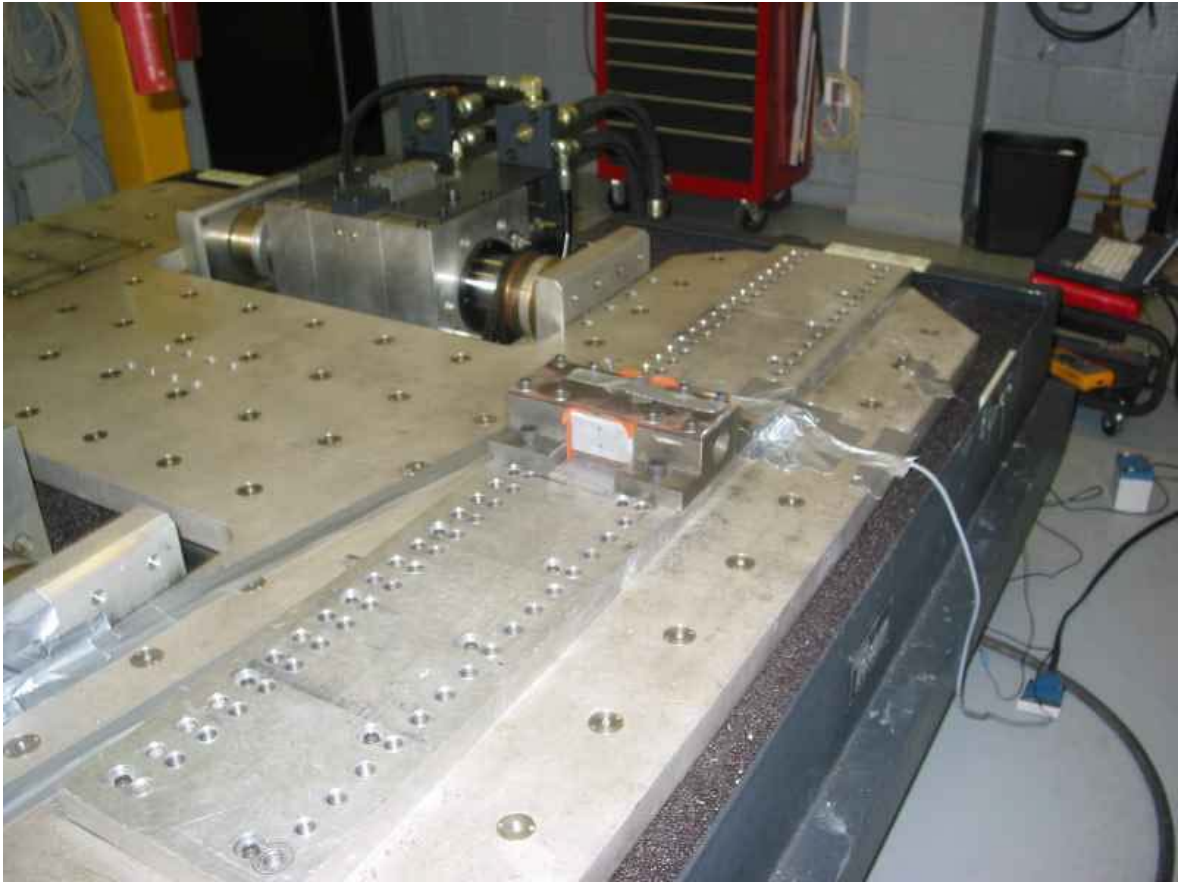


Figure 3.7: Sensors Package Installed on the Vibration Table

3.4.2 Sensor Qualification under Drilling Vibration

The vibration test was run for 45 minutes with vibration frequencies ranging from 5 Hz to 400 Hz and an acceleration peak magnitude of 14 g. A random vibration profile was implemented in order to cover the entire range from the low frequency beginning, 5–30 Hz, and moving up to 400 Hz [Weatherford, 2006]. This efficiently mimics the vibration environment experienced while drilling.

Accelerometer and gyroscope sensors were fully functional at the end of the test, which qualified the MEMS sensors to perform under the drilling vibration environment. Measurements of three gyroscopes and three accelerometers were collected during the test. Accelerometer measurements that were contaminated with vibration effects throughout the test are presented in Figure 3.8. The three orthogonal accelerometer measurements were collected for a period of 45 minutes. Measurements were logged for a period of 6 minutes before the vibration profile started. An increase in the high frequency background during the vibration test and the presence of constant biases that offset the measurements from the expected values can be noted.

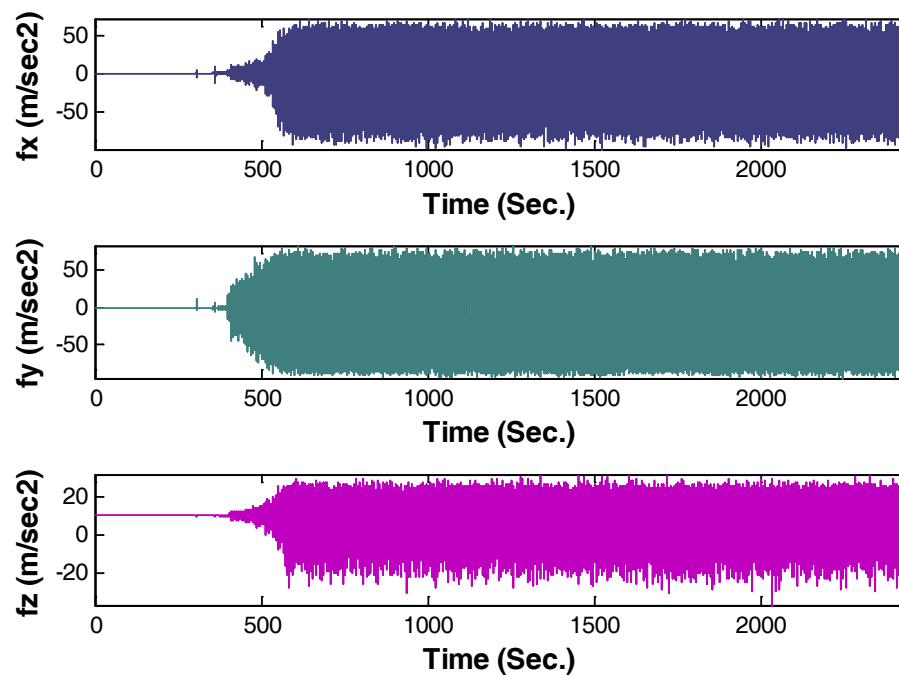


Figure 3.8: Accelerometer Measurements throughout Vibration Test

The magnitude of the biases were 0.6 g, 1.3 g, and .08 g for accelerometers x, y, and z, respectively. This agrees with the fact the two horizontal accelerometers x and y are exposed to a vibrations due to the use of a horizontal vibration table. Moreover, this accurately simulates the drilling vibration environment where the lateral vibration is greater in magnitude than the vertical vibration along the drill collar rotation axis [Lyons and Plisga, 2005]. The analysis of the vibration effects on MEMS sensor measurements are discussed in the following section.

3.4.3 Analysis of Vibration Effect

Two tests with different parameters were conducted. The vibration frequency ranged from 5 Hz to 400 Hz for the two tests, but the acceleration peak magnitude was 12 g for the first test and 14 g for the second test. A screen caption of the first test parameters can be viewed in Figure 3.9. The generated vibration had a random nature and ranged in frequency from 5 Hz to 400 Hz.

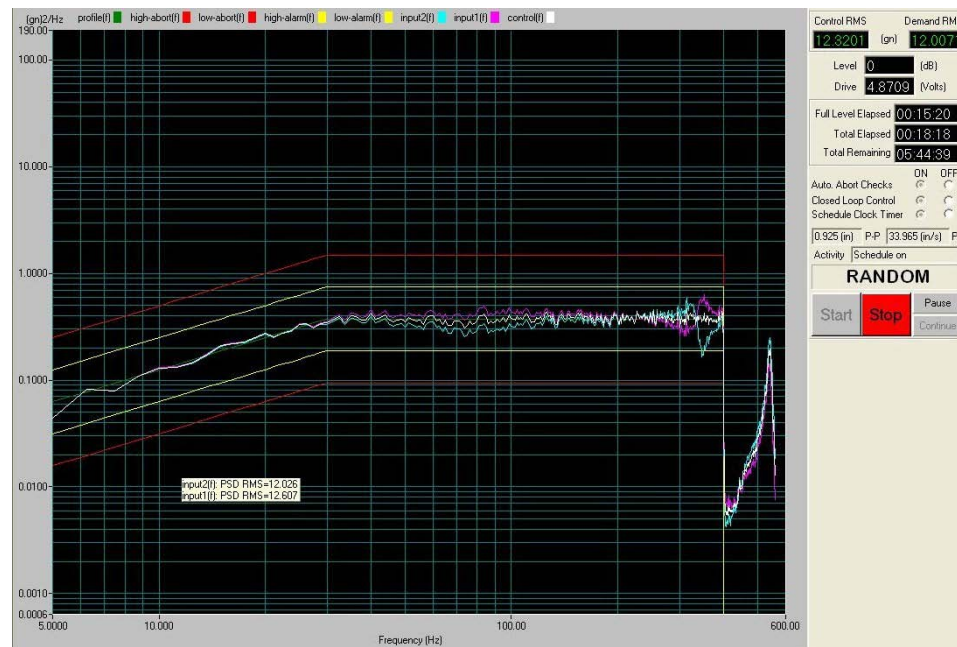
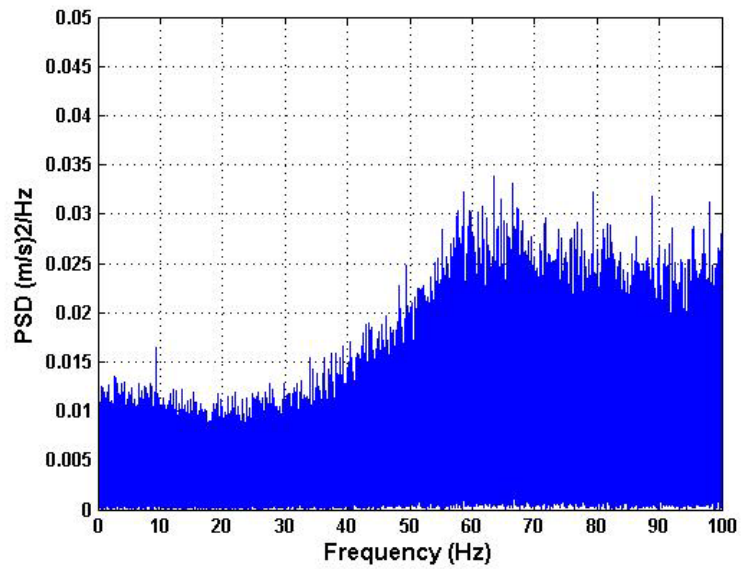


Figure 3.9: Screen Capture of Vibration Test Parameters

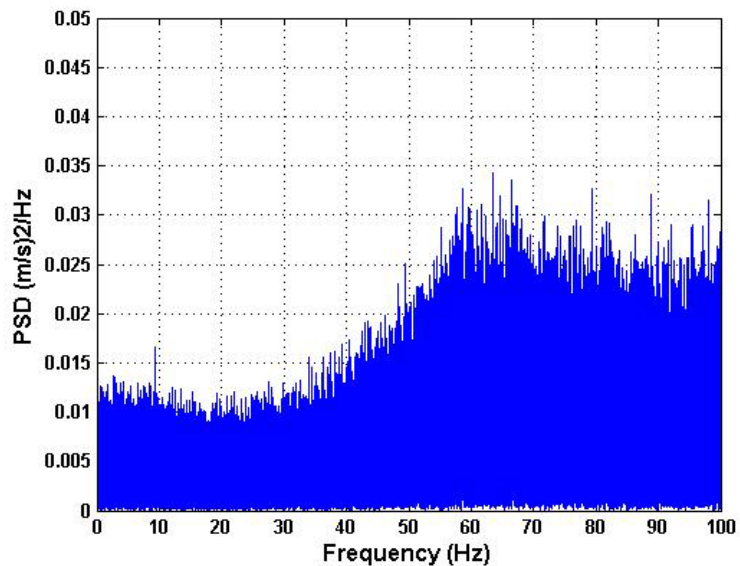
For comparison, measurements from the two tests were examined in the frequency domain. PSD measurements from accelerometer x and gyroscope z were derived and presented in Figure 3.10 and Figure 3.11, respectively. The computed PSD was normalized with a maximum of $1.6614 \times 10^{+006}$ (m/s)²/Hz for accelerometer measurements and a maximum of $3.7815 \times 10^{+004}$ (deg/s)²/Hz for gyroscope measurements.

Vibration had stronger effects in the high frequency region of accelerometers (40 Hz and above), while the opposite was true for gyroscope measurements. The background noise contaminating accelerometer measurements was approximately similar for the two tests. However it slightly increased in the gyroscope measurements with

increasing vibration magnitude. The severity of the vibration effects and previously discussed shock impacts on MEMS sensor measurements, and the need to reduce these effects in order to enhance the performance of the MEMS inertial sensors under drilling shock and vibration was evident.

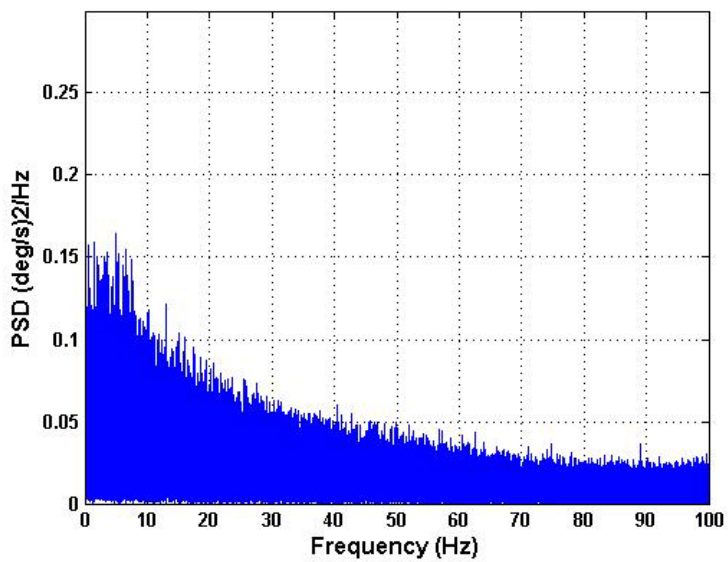


a) At 12 g

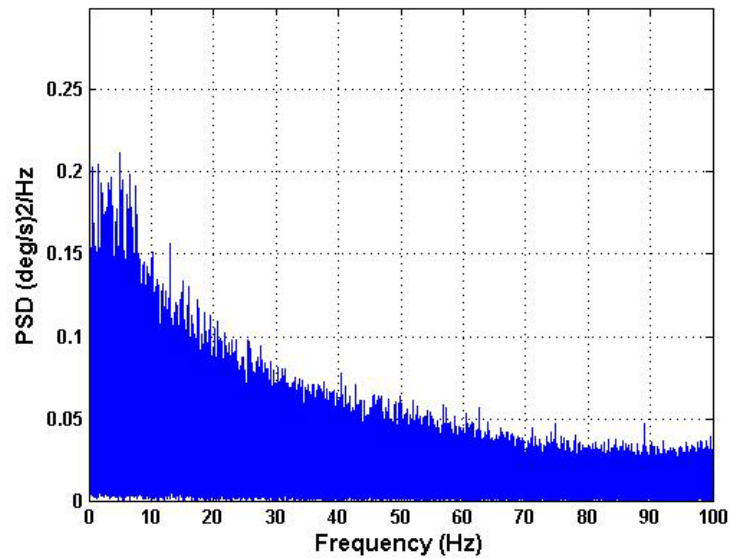


b) At 14 g

Figure 3.10: PSD of Accelerometer X Output Signal Contaminated by Vibration Effects



a) At 12 g



b) At 14 g

Figure 3.11: PSD of Gyroscope Z Output Signal Contaminated by Vibration Effects

3.5 Summary

Inertial MEMS sensors are proposed for directional drilling applications as a complete solution to provide a continuous trajectory of the wellbore while drilling. The continuous trajectory position accuracy is limited to MEMS sensors characteristics. They are sensor bias, scale factor, output stability, thermal sensitivity, shock survivability, and the induced noise due to vibration effects. In the hostile drilling environment, MEMS sensors are exposed to severe shock and vibration. The survivability of the MEMS sensors under drilling shock and vibration were investigated in this chapter.

MEMS inertial sensors successfully passed the two shock and vibration qualification tests conducted at an industry partner facility in Houston, Texas. The first qualification test was conducted under shock forces of 1400 g at 3400 vpm for a period of 4 hours, while the second test was performed under vibrations ranging from 5 Hz to 400 Hz with a peak acceleration of 14 g. Additionally, sensor output signals were analyzed using PSD. Shock and vibration can damage high frequency components; the extent of damage depends on the magnitude of the applied shock or vibration. Background noise of a relatively high magnitude and broadband characteristics contaminated gyroscope and accelerometer measurements along the entire frequency spectrum; background noise increased with an increase in intensity of shock forces.

In the following chapter, a discussion of wavelet packet transform analysis is presented in order to detect shock levels and wavelet multi-resolution analysis is introduced to drilling applications to separate the vibration effects from the MEMS output signals.

CHAPTER FOUR:

PERFORMANCE ENHANCEMENT

UNDER DRILLING SHOCK AND VIBRATION

Inertial sensor measurements have a limited accuracy due to measurement errors. Errors produced due to shock and vibration while drilling are categorized as short term errors. Wavelet transform (WT) analysis was proposed to analyze and mitigate short term errors induced by shock and vibration.

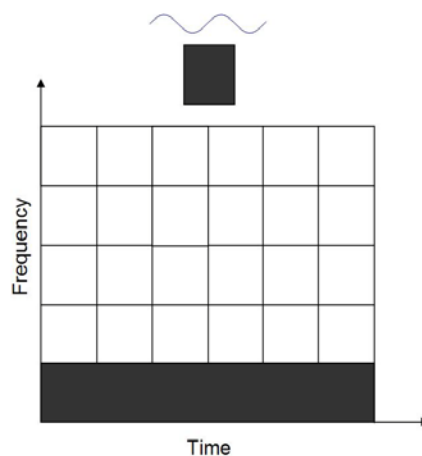
The Fourier transform (FT) was implemented to decompose a time-domain sequence in terms of a set of basis functions. The complex sinusoids set $\{ e^{i\omega n}, -\infty < \omega < \infty \}$ forms the set of these basis functions where i is a complex number ($i = \sqrt{-1}$), ω is the frequency and n is the discrete time variable. The expression of a discrete Fourier transform (DFT) of a discrete time signal $x(n)$ is given as:

$$x(\omega) = \sum_{n=-\infty}^{\infty} x(n)e^{-i\omega n} . \quad 4.1$$

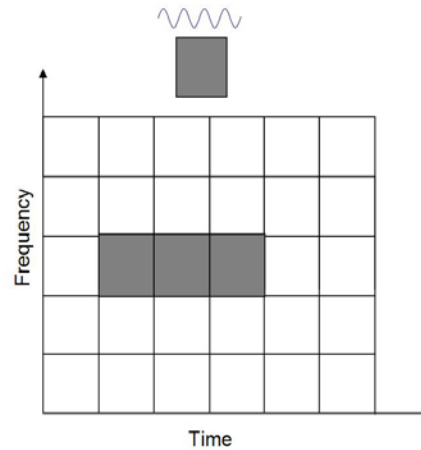
The transform of FT is the result of summation over the entire signal length. Thus it has a limitation that the result cannot indicate at what time a specific transient signal occurred. A better time resolution can be accomplished by applying a short time Fourier transform

(STFT). This utilizes a window function that is multiplied by the input signal before computing the FT [Robertson et al., 1996]. The time-frequency representation of the signal by STFT has the drawback that the window width is fixed. Illustration of the STFT of a signal is presented in

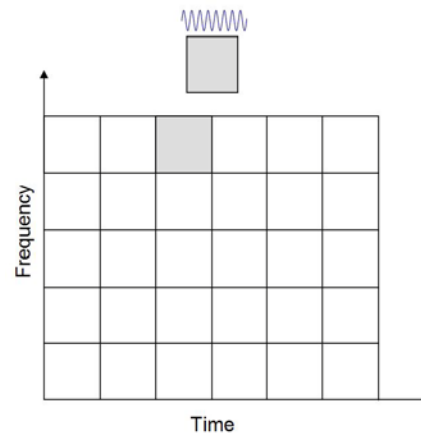
Figure 4.1, where the STFT is represented in a two dimensional grid. The divisions in the horizontal direction are the time extent for each window, while the divisions in the vertical direction are the frequencies. The shade of each rectangle is proportional to the frequency of the monitored signal component, where the shade of the rectangle is darker for the lower observed frequency component. The width of the window function represents the accuracy of the information about the different frequencies within the window. As the width of the window function increases, more accurate information about the different frequencies within the window are obtained, however the ability to determine when those frequencies occur is lost [Ogden, 1997].



(a) Wide Window (low frequency)



(b) Medium Window (medium frequency)



(c) Narrow Window (high frequency)

Figure 4.1: Time-Frequency Representation of Short Time Fourier Transform STFT [Robertson et al., 1996].

Wavelet transform provides multiple resolutions; a fine time resolution for short duration, high frequency signals, and a fine resolution for long duration, low frequency signals. Thus, wavelet transform was proposed in this research to analyze and enhance the performance of the inertial MEMS sensors under severe drilling shock and vibration environments.

4.1 Wavelet Transform

Wavelet transform (WT) is based on a windowing technique with variable sized regions. WT analysis is capable of utilizing long time intervals where precise low frequency information is needed, and shorter intervals where high frequency information is considered. WT therefore will provide an accurate location of the transient signals while simultaneously reporting the fundamental frequency and its low order harmonics.

WT can measure the time evolution of frequency transients. This requires using a complex analytic wavelet. Analytic wavelets are usually used to measure instantaneous frequencies in contrast to “real” wavelets which are used to detect sharp signal transitions [Mallat, 1999 and Burke, 1998]. WT output is represented in a two dimensional grid similar to the STFT, but with different divisions in time and frequency as shown in Figure 4.2.

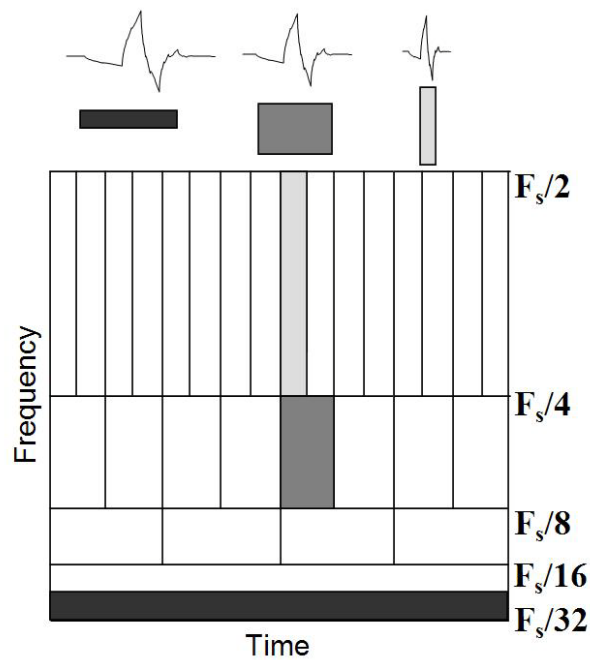


Figure 4.2: Time Frequency Representation of Wavelet Transform WT

[Robertson et al., 1996].

In Figure 4.2, the rectangles have an equal area or a constant time-bandwidth product such that they narrow at the low scales that present high frequencies and widen at the high scales that present low frequencies. In contrast to the STFT, the WT isolates transient high frequency components in the top frequency band at the time of their occurrence while the continuous low frequency components are presented as a continuous magnitude. The localized wavelet coefficients are useful tools for analyzing nonstationary events.

The WT of a time-domain signal is defined in terms of the projections of this signal onto a family of functions that are normalized dilations and translations of a wavelet

function. The wavelet basis functions $\psi(t)$ are not limited to exponential or sinusoidal basis functions as in FT. This can be achieved by restricting $\psi(t)$ to be short and oscillatory. Furthermore, it must have zero average and decay quickly at both ends. These admissibility conditions ensure that the integration in the WT equation is finite [Mallat, 1999]. The function $\psi(t)$ has been given the name wavelet or “small wave” and is referred to as the “mother wavelet”; it dilates (scaled) and translates (shifted) simply as “wavelets” or “daughter wavelets” [Daubechies, 1998]. Schematic representation of a few mother wavelet functions is presented in Figure 4.3.

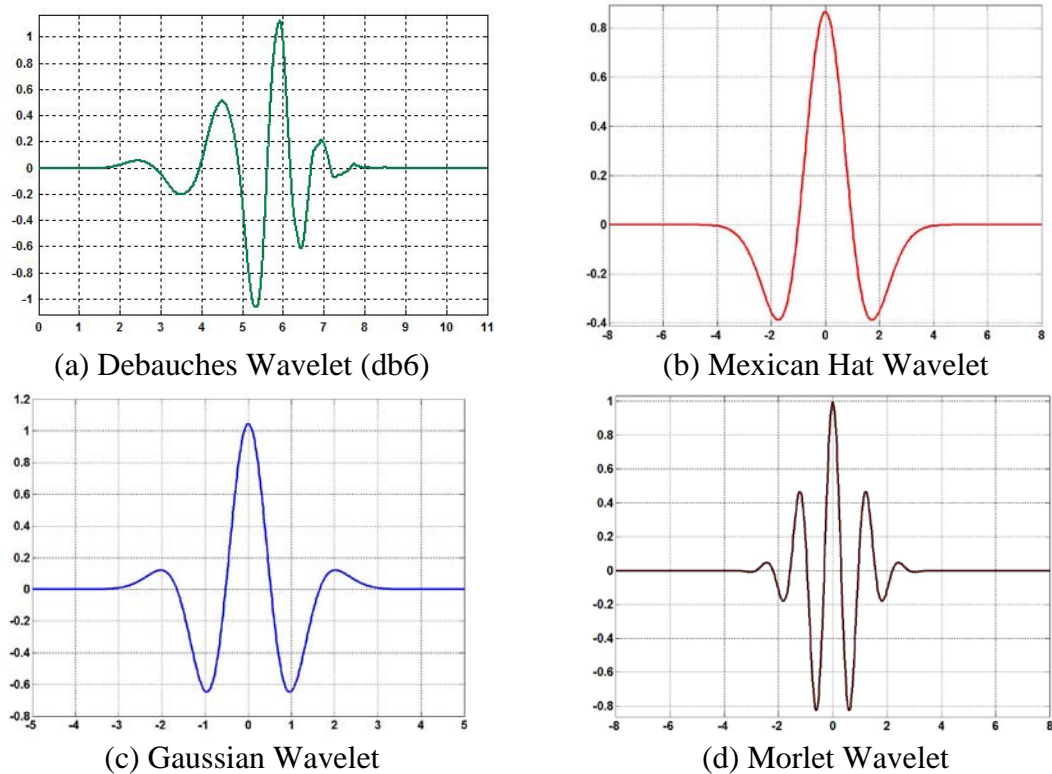


Figure 4.3: Mother Wavelets [Misiti et al., 2000]

4.1.1 Continuous and Discrete Wavelet Transform

The expression of the continuous wavelet transform CWT of a time domain signal $x(t)$ is:

$$CWT(a, \tau) = \frac{1}{\sqrt{a}} \int_{-\infty}^{\infty} x(t) \psi\left(\frac{t-\tau}{a}\right) dt, \quad 4.2$$

where a is the scaling parameter and τ is the shifting parameter of the wavelet function $\psi(t)$. The time domain signal $x(t)$ is multiplied by the shifted and scaled versions of the wavelet function for each scale a and shift τ . With the use of digital computers, the discrete wavelet transform DWT is used, where the DWT of a discrete time sequence $x(n)$ is expressed as:

$$C_{j,k} = 2^{(-j/2)} \sum_n x(n) \psi(2^{-j} n - k), \quad 4.3$$

where $\psi(n)$ is the basis function utilized in the wavelet transform, while $2^{(-j/2)} \psi(2^{-j} n - k)$ are the scaled and shifted versions of $\psi(n)$ where j is the scaling coefficient and k is the shifting coefficient. Finally, $C_{j,k}$ represents the corresponding wavelet coefficient.

4.1.2 Wavelet Multi-Resolution Analysis WMRA

Wavelength multi-resolution analysis (WMRA) is a technique to perform discrete WT. It allows the decomposition of signals into various resolution levels. The data with coarse resolution contains information about low frequency components and retains the main features of the original signal. The data with fine resolution retains information about the high frequency components. Scaling a wavelet simply means stretching or compressing it in the time domain. The smaller the scale the more the wavelet will be compressed while the larger the scale the more the wavelet will be stretched. Therefore, low scales allow analysis of rapidly changing details (high frequency components) and high scales allow analysis of slowly changing features (low frequency components) [Burrus et al., 1997]. The low frequency component of the signal identifies the long term variation of the signal and is capable of providing a very good approximation of it. The approximations correspond to the high scale low frequency part.

On the other hand, the high frequency content carries few details about the signal [Burrus et al., 1997]. The details correspond to the low scale high frequency part. Wavelet analysis therefore decomposes the signal into various resolution levels. The data with coarse resolution contains information about low frequency components and retains the main features of the original signal. The data with fine resolution retains information about the high frequency components [Chui, 1992].

For an input digital signal $x(n)$, the approximation coefficient $a_{j,k}$ at the j^{th} resolution level is computed as [Chui, 1992; Burrus et al., 1997]:

$$a_{j,k} = 2^{(-j/2)} \sum_n x(n) \phi(2^{-j}n - k), \quad 4.4$$

where ϕ is a scaling function similar to the wavelet scaling function except that it has only positive values. Scaling functions are designed to smooth the input signal and thus operate in a manner equivalent to a low pass filter which rejects high frequency components of the signal [Mallat, 1999; Burrus, 1997]. The approximation of $x(n)$ at the j^{th} resolution level can then be computed as:

$$x_j(n) = \sum_{k=-\infty}^{\infty} a_{j,k} \phi_{j,k}(n). \quad 4.5$$

The details coefficient $d_{j,k}$ at the j^{th} resolution level and the detail signal $g_j(n)$ are then computed as:

$$d_{j,k} = \sum_n x(n) \psi_{j,k}(n), \quad 4.6$$

$$g_j(n) = \sum_{k=-\infty}^{\infty} d_{j,k} \psi_{j,k}(n), \quad 4.7$$

where $\psi_{j,k}(n)$ is the wavelet basis function. The original discrete signal $x(n)$ can be reconstructed using all the details obtained during the decomposition process at all resolution levels as presented in the following expression:

$$x(n) = \sum_{j=-\infty}^{\infty} g_j(n) = \sum_{j=-\infty}^{\infty} \sum_{k=-\infty}^{\infty} d_{j,k} \psi_{j,k}(n). \quad 4.8$$

This expression implies that the original signal has to be processed at an infinite number of resolutions, which is not practical. Alternatively, the analysis can stop at the J^{th} resolution level and the signal can be reconstructed using the approximation at that level and all the details starting from the first resolution level until the J^{th} resolution level. This can be presented in the following expression:

$$x(n) = \sum_{j=-\infty}^{\infty} a_{j,k} \phi_{j,k}(n) + \sum_{j=1}^J \sum_{k=-\infty}^{\infty} d_{j,k} \psi_{j,k}(n). \quad 4.9$$

The first term represents the approximation at level J and the second term represents the details at resolution level J and lower. Thus, multi-resolution analysis builds a pyramidal structure that requires an iterative application of scaling and wavelet functions, respectively. These filters initially act on the entire signal band at the high frequency first and gradually reduce the signal band at each stage. Illustration of the WMRA pyramid structure is presented in Figure 4.4.

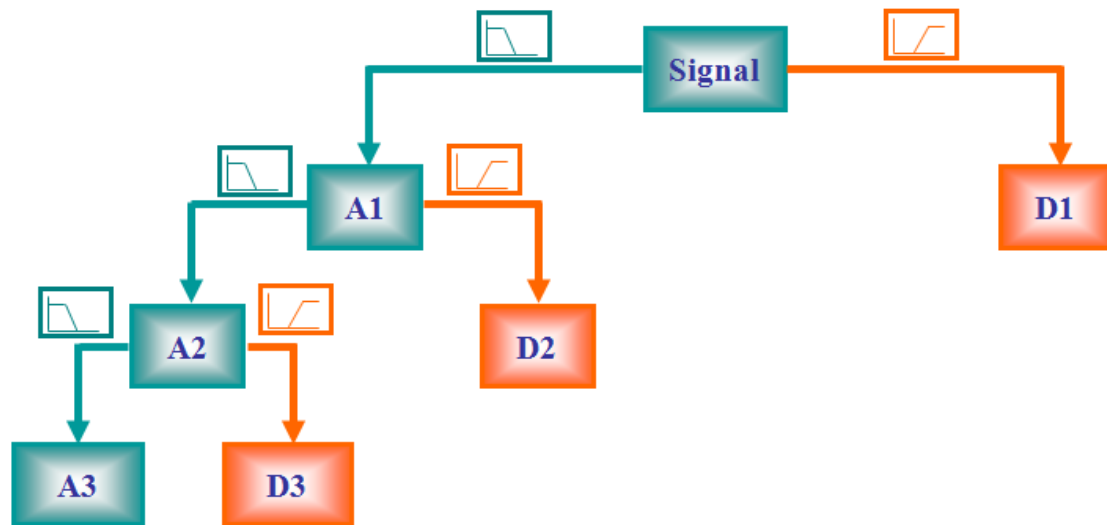


Figure 4.4: WMRA Structure at 3 Levels of Decomposition of the Input Signal

The high frequency band outputs are taken as the detail coefficients D1, D2, D3, and the low frequency band outputs are taken as the approximation coefficients A1, A2, A3.

4.1.3 Wavelet Packet Transform WPT

The main difference between the WPT and WMRA is that wavelet packets apply the decomposition not only to the approximation but also to the details. The flexibility of the wavelet packet decomposition where it provides more bases allows an efficient analysis of the monitored dynamics to be performed. The wavelet packet $\psi_{j,k}^i(t)$ is a function of the modulation i , the scale coefficient j , and the shifting coefficient k . It can be expressed as:

$$\psi_{j,k}^i(t) = 2^{j/2} \psi^i(2^j t - k), \quad i = 1, 2, 3, \dots \quad \mathbf{4.10}$$

The mother wavelet ψ^i is obtained from the following recursive relationships:

$$\psi^{2i}(t) = 2^{1/2} \sum_{k=-\infty}^{\infty} h(k) \psi^i(2t - k), \quad 4.11$$

$$\psi^{2i+1}(t) = 2^{1/2} \sum_{k=-\infty}^{\infty} g(k) \psi^i(2t - k), \quad 4.12$$

where $h(k)$ and $g(k)$ represent discrete filters that solve each equation. The WPT starts by deriving the wavelet packet decomposition of the discrete input signal at level N using the mother wavelet. At each level N of decomposition, there are a number of 2^N packets. This provides the ability to analyze the input signal at different frequency bandwidths and determine the actual time of occurrences. WPT decomposition of the signal provides an efficient analysis of MEMS measurement dynamics under the effects of shocks and vibration while drilling. An illustration of the WPT of the input signal is shown in Figure 4.5 for 3 levels of decomposition.

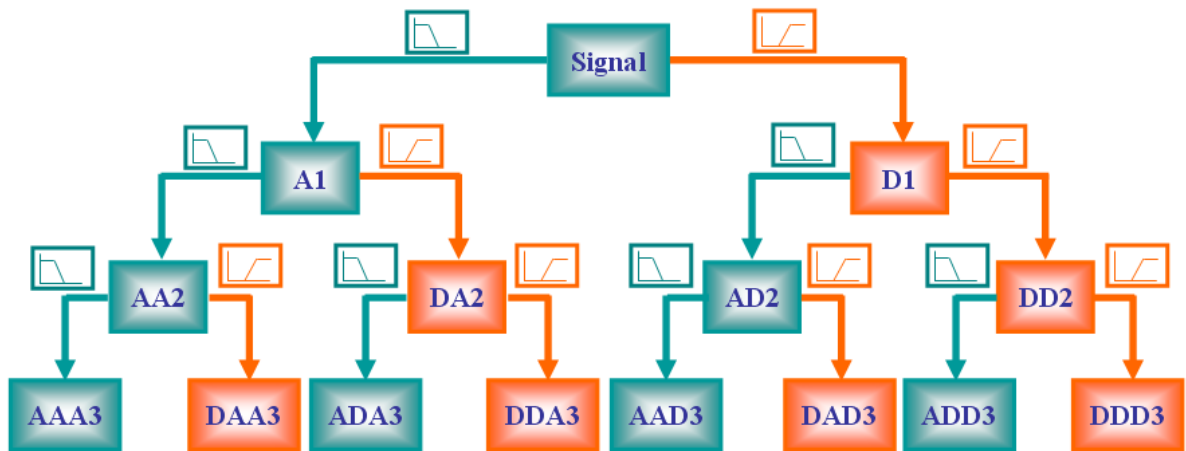


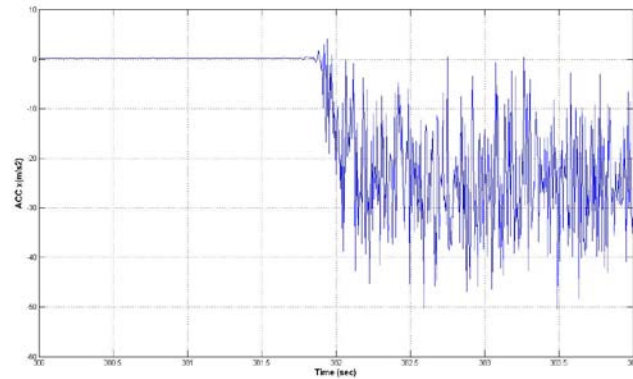
Figure 4.5: WPT of 3 Levels of Decomposition of the Input Signal

Two objectives were reached by processing the measurements of the MEMS sensors through WPT and WMRA modules. The first objective was to analyze the different characteristics of the signal components under a harsh drilling environment, and to detect the impact of this harsh environment on the measurements. The second objective was to separate the frequency components corresponding to shock and vibration from the monitored motion dynamics of the drill string, and hence obtain reliable inertial sensor measurements to derive the drill bit position and attitude angles.

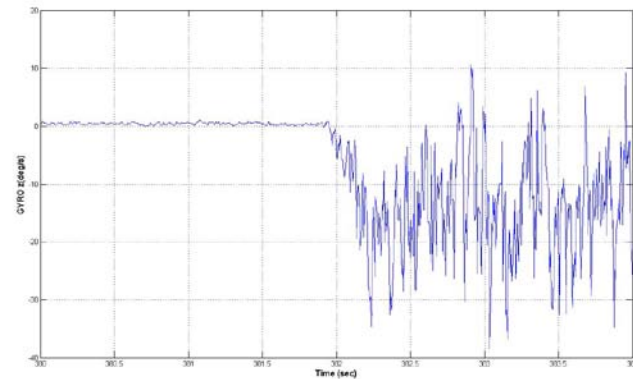
4.2 Shock Effects on MEMS Sensors

4.2.1 WPT analysis of shock forces

The wavelet packet analysis technique was implemented to separate and analyze shock and vibration from the motion dynamic components. The MEMS inertial sensor measurements were processed through a WPT module. The accelerometer x and gyroscope z measurements were selected where they were exposed to the most shock forces. The raw measurements of accelerometer x and gyroscope z are presented in Figure 4.6 for the selected 4 sec window. Figure 4.6 shows that measurements of both accelerometer and gyroscope became biased and noisy when shock forces were implemented at 382 seconds; the noise continues throughout the rest of the test as shock forces are continuously applied.



a) Accelerometer (X) Raw Measurements



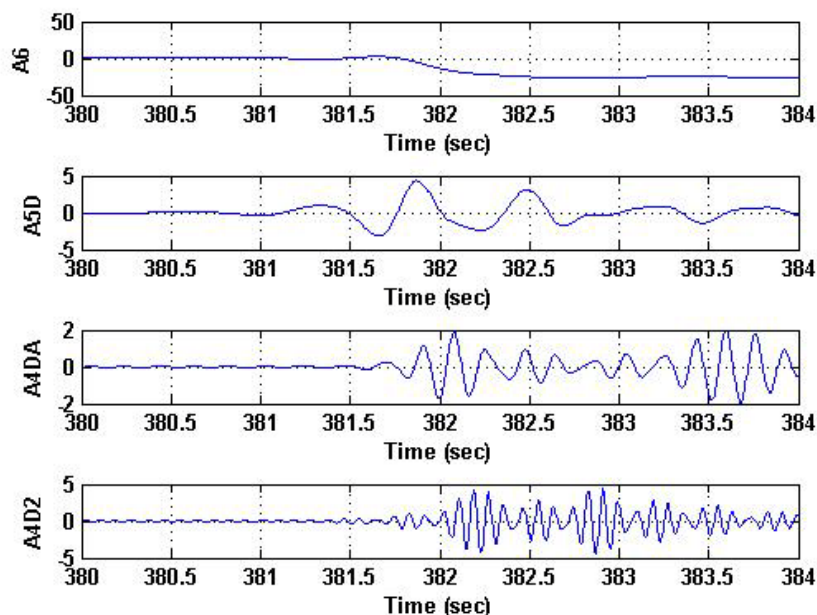
b) Gyroscope (Z) Raw Measurements

Figure 4.6: Raw Measurements under 1400 g Shock Forces

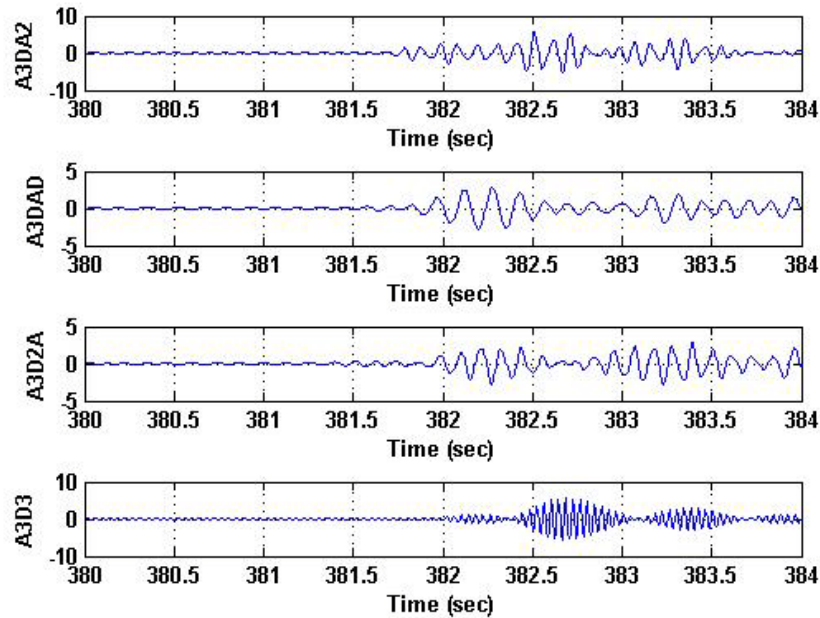
The WPT was utilized in order to decompose the raw input signal of each sensor at 6 levels of signal decomposition. Level 6 of the WPT consists of 64 packets dividing the entire 100 Hz frequency band width into small packets, each of 1.56 Hz bandwidth. Figure 4.7 shows the first 8 packets of the WPT of the 6th level of decomposition for accelerometer x measurements over a 4 sec window. The analyzed period captures the 1400 g shock forces when commenced after 2 sec of the test period. The first

approximation A6 in the upper panel of Figure 4.7 presents accelerometer measurements within the frequency bandwidth 0–1.56 Hz. This packet includes all the useful motion information of the drilling and efficiently separates all undesirable dynamics due to shock.

At the beginning of the shock forces at 382 seconds, the WPT was able to provide a clean signal (denoised) with the desired information only. However the signal was biased as soon as the shock started due to the fact the shock forces were applied continuously throughout the test. In practice, shock forces impact the measurements as impulses over very short periods. Therefore, as soon as the impacted signal is denoised by utilizing a WPT module, the measurement should not include a bias.



a) Approximation Signals of Accelerometer X



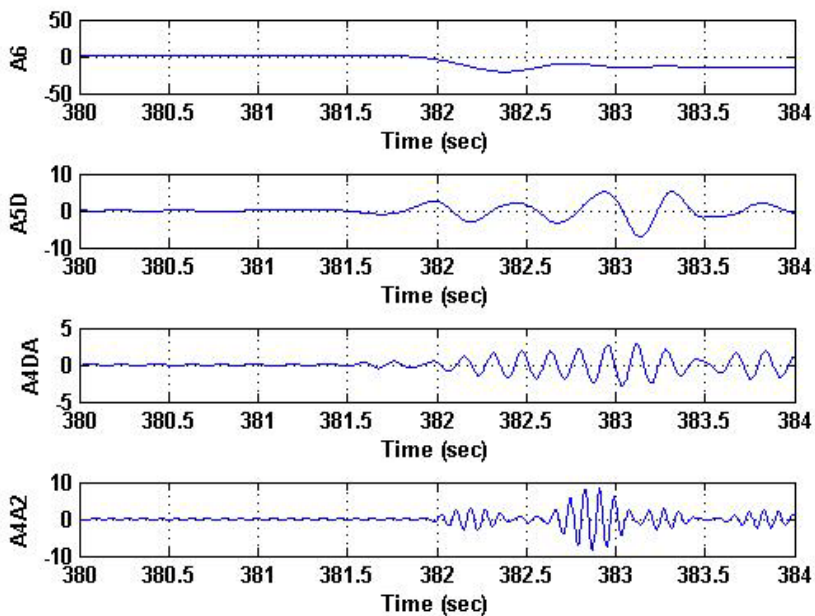
b) Details Signals of Accelerometer X

Figure 4.7: WPT Accelerometer Signal Decomposition at Level 6 under Shock

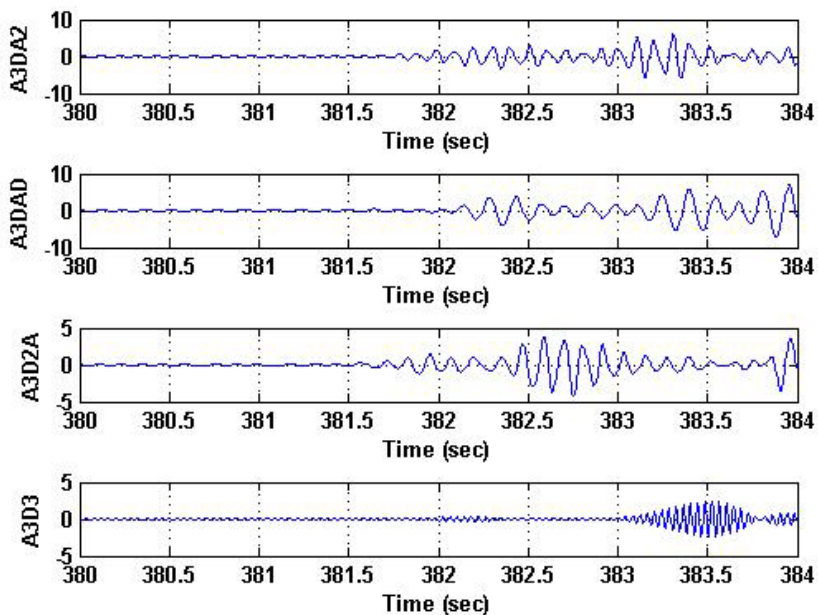
The second panel from the top A5D in Figure 4.7a presents the second packet with a frequency band from 1.56 Hz to 3.125 Hz. The PSD was performed and a peak frequency was observed at 1.58 Hz. The third panel from the top A4DA in Figure 4.7a presents a packet with a frequency band from 3.125 Hz to 4.68 Hz that includes a peak frequency at 3.2 Hz, while packet A4D2 (fourth panel, Figure 4.7a) presents a frequency band from 4.68 Hz to 6.25 Hz with a peak frequency at 4.859 Hz.

The wavelet packets presented in Figure 4.7b cover a frequency band from 6.25 Hz to 12.5 Hz with a similar packet bandwidth of 1.56 Hz. The fifth packet at the 6th level of signal decomposition A3DA2 includes a frequency band from 6.25 Hz to 7.81 Hz,

and has a peak frequency of 6.4 Hz. The following packet A3DAD presents a frequency band from 7.81 Hz to 9.37 with an observed peak frequency at 7.92 Hz. The seventh packet at the 6th level of signal decomposition A3D2A includes a frequency band from 9.37 Hz to 10.93 Hz with a peak frequency at 9.52 Hz. The lower panel of Figure 4.7b presents the eighth packet at the 6th level of decomposition that has a frequency band from 10.93 Hz to 12.5 Hz with an observed peak frequency at 11.32 Hz. By examining the eight wavelet packets in Figure 4.7, it can be concluded that as soon as shock forces started, frequencies with different magnitudes and wavelengths were induced at frequencies higher than 1.56 Hz. Similar observations are true for the gyroscope signals, which were decomposed to the 6th level of signal decomposition using a WPT. The first eight wavelet packets at the lower frequency end are presented in Figure 4.8.



a) Approximation Signals of Gyroscope Z



b) Details Signals of Gyroscope Z

Figure 4.8: WPT Gyroscope Signal Decomposition at Level 6 under Shocks

The PSD of each packet was measured in order to explore the frequency domain. The observed peak frequencies at each packet corresponded to the ones observed in the accelerometer measurement. The similarity between peak frequencies of gyroscope and accelerometer measurements at wavelet packets higher than 1.56 Hz is not surprising as they were affected by the same shock forces at similar magnitudes.

4.2.2 Detection of Shock Impact

Severe shock while drilling limits the drilling speed (rate of penetration) significantly. In addition, it is a main reason for tool failure as it causes the BHA to twist off and be lost in the well hole. Therefore, if the driller has an indication of the shock level while drilling, mitigating actions can be taken to reduce the shock effects. Reducing the weight on the bit and torquing and operating (moving up and down while the bit is off bottom) the drill string can release stress or stuck pipes. Drilling can be optimized if there is information available about the shock level while drilling. In this section, a shock detection methodology based on the WPT is suggested.

Shock and vibration produce high frequency components in the measurement signal. A WPT can extract such high frequency components. The WPT further includes these components in the first level detail package D1. It was proposed that for each 4 sec window, the WPT decomposes the sensor output signals into six levels of decomposition. High frequency components are included in D1 and are monitored

while drilling. Shock can be detected by observing the energy of the detail packet D1 by deriving the norm $\|D1\|$ and comparing it to a predefined threshold.

$$\|D1\| = \left[\sum_{k=1}^{n_d} D1^2(k) \right]^{1/2}, \quad 4.13$$

where n_d is the number of the coefficients of the packet D1. Shock occurs if $\|D1\|$ is higher than the threshold. The threshold is selected such that the shock detector has a fast transient response that can inform the driller within 4 sec of the commencement of shock. It is essential to be able to monitor the shock level; in a severe shock environment the drilling operation has to be altered or entirely stopped if the environment becomes too harsh. The shock level can be identified by observing the change in the energy of the 6th level approximation wavelet packet A6, which includes the desirable low frequency components. This packet contains signals which are affected significantly by the bias induced by shock. Similarly, the energy of A6 is observed by monitoring the norm of this packet $\|A6\|$. The level of shock is identified relative to the energy magnitude of this packet.

$$\|A6\| = \left[\sum_{k=1}^{n_d} A6^2(k) \right]^{1/2}. \quad 4.14$$

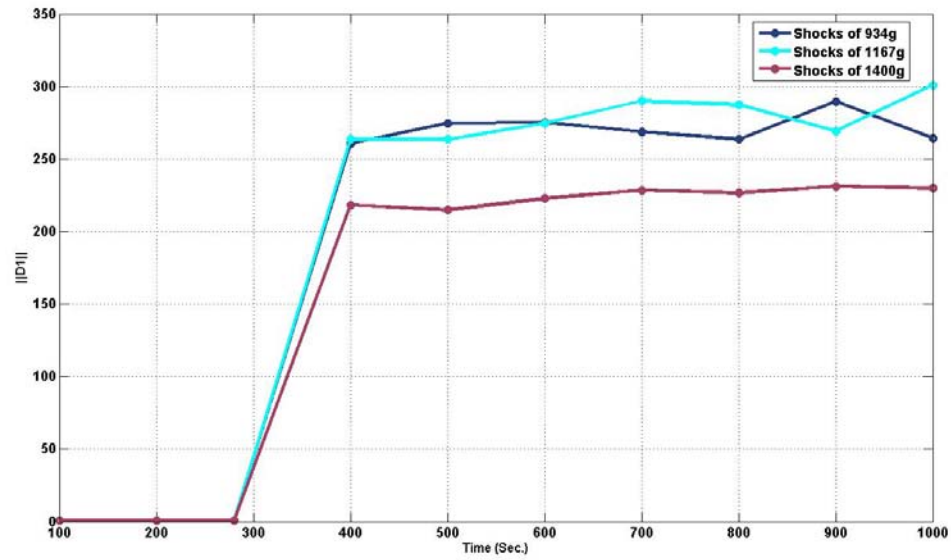
An illustration of shock detection and shock level identification is presented in Figure 4.9. In this analysis, data from three shock tests were examined over a period of a 1000 sec. Shock forces of 934 g, 1167 g, and 1400 g were applied in the three tests. For each test data set, the WPT was applied at 10 separate windows with a window size of 4 sec. Location of the selected windows are indicated by the marker location on the plots in Figure 4.9.

The WPT decomposed the signal at each window; the norm of the level 1 detail $D1$ packet was derived. As soon as the algorithm observed $\|D1\|$ to be larger than 5, shock was observed and the WPT decomposed the signal further to level 6. The norm of the level 6 approximation packet $\|A6\|$ was derived and is presented in Figure 4.9b. The shock level was then identified by comparing $\|A6\|$ to the predefined threshold T according to Table 4.1. The threshold was selected by examining the energy of the packets in Figure 4.9. Threshold values are expected to change when the examined window size changes.

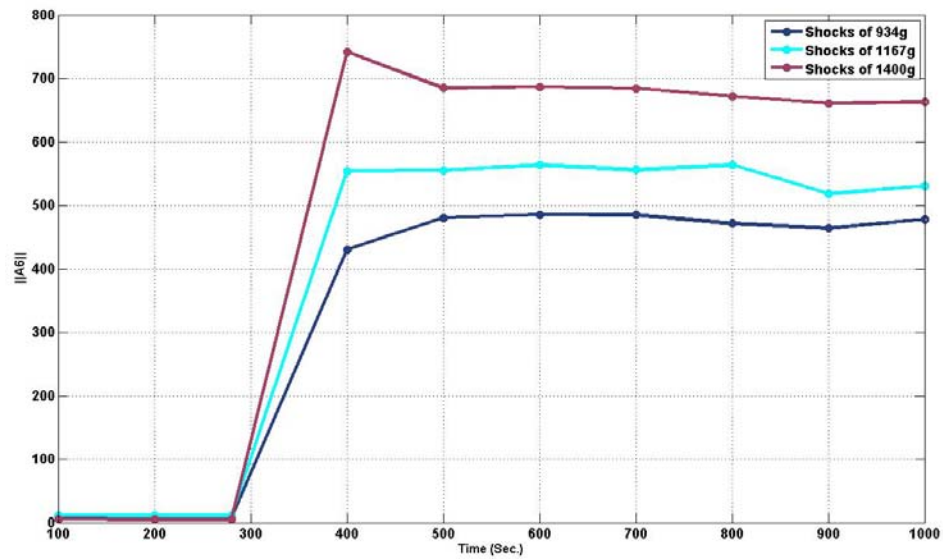
Table 4.1: Threshold of Shock Levels

Shock Level	No Shock	Low Shock	Medium Shock	High Shock
Threshold T	$T < 100$	$100 < T < 400$	$400 < T < 600$	$600 < T$

The drilling operation will take advantage of the information about shock levels and adjust drilling parameters to optimize the operation.



a) Detail D1



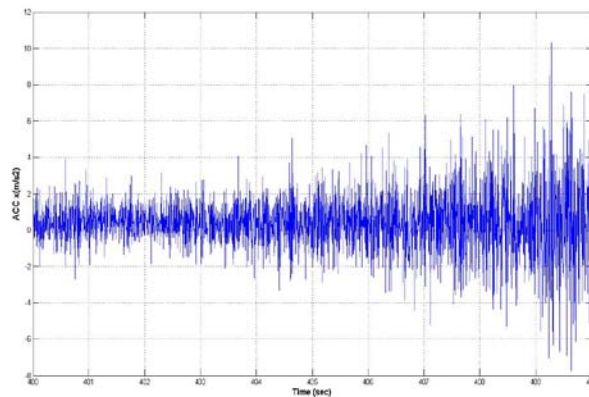
b) Approximation A6

Figure 4.9: Energy of Extracted Packet Detail D1 (a), and Approximation A6 (b)

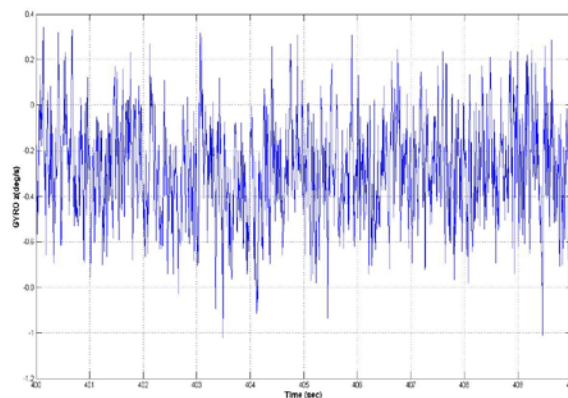
4.3 Vibration Effects on MEMS Sensors

4.3.1 WPT Analyses of Vibration Effects

Accelerometer x and gyroscope z measurements were processed through a WPT module at 6 levels of signal decomposition. Measurements were collected during the vibration test while the vibration frequency ranged from 5 Hz to 400 Hz with an acceleration peak magnitude of 14 g. The raw measurements over 10 sec are presented in Figure 4.10a and b for accelerometer x and gyroscope z, respectively.



a) Accelerometer (X) Raw Measurements

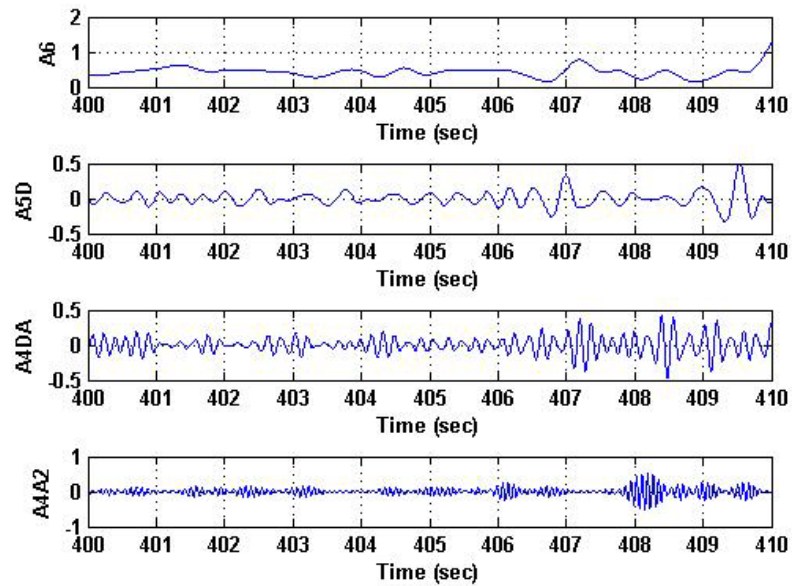


b) Gyroscope (Z) Raw Measurements

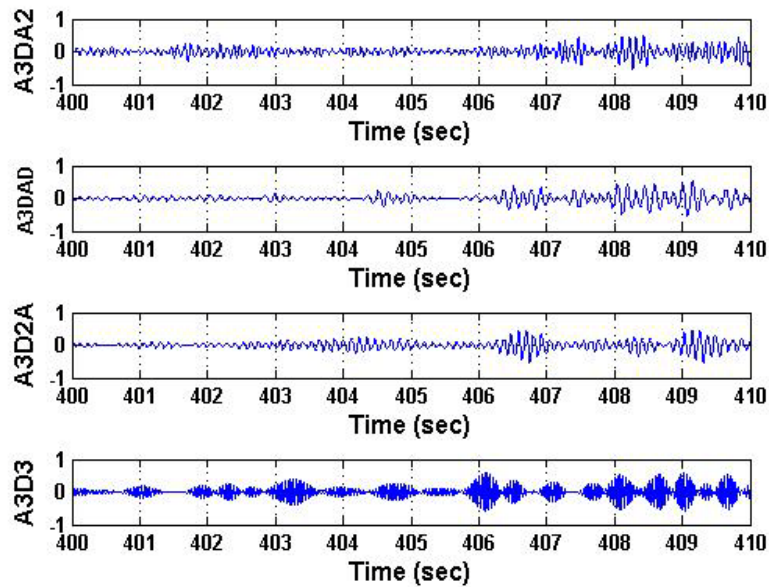
Figure 4.10: Raw Measurements under Vibration Effects

The raw measurements were decomposed in Figure 4.11, which presents the first 8 packets of the 6th level of the signal decomposed by WPT for accelerometer x measurements over a 10 sec interval when the vibration had already commenced. Similarly, the gyroscope z signal decomposition is presented in Figure 4.12.

As the packet A6 represents frequency components lower than 1.56 Hz, both accelerometer and gyroscope measurements contain a low frequency component that is a part of sensor inherent random errors. This component is modelled by applying a specific stochastic model to the Kalman filtering in order to be optimally estimated and removed. Higher wavelet packets (A5D, A4DA, A4D2, A3DA2, A3DAD, A3D2A, and A3D3) contain higher frequency components; the higher the wavelet packet bandwidth, the higher are the included frequency components. Such high frequency components can be isolated while processing the sensor measurements by WPT.

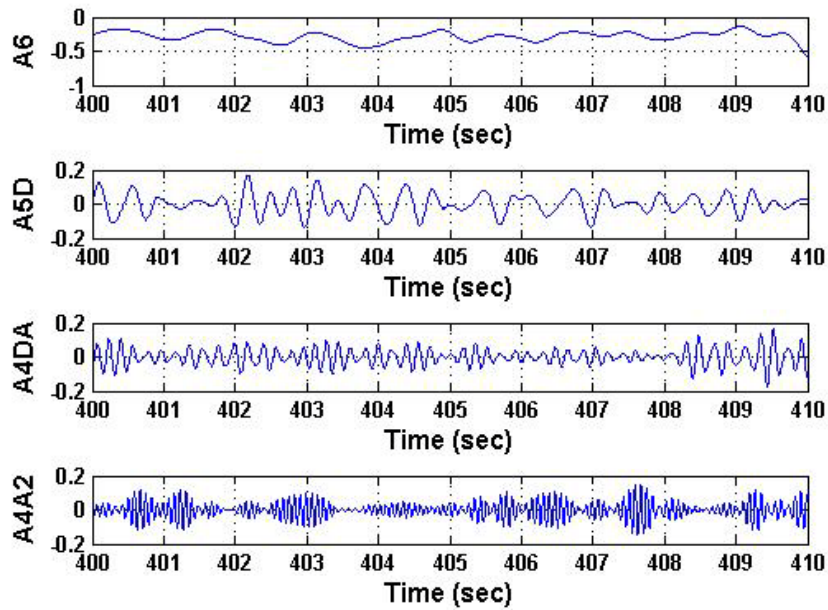


a) Approximation Signals of Accelerometer X

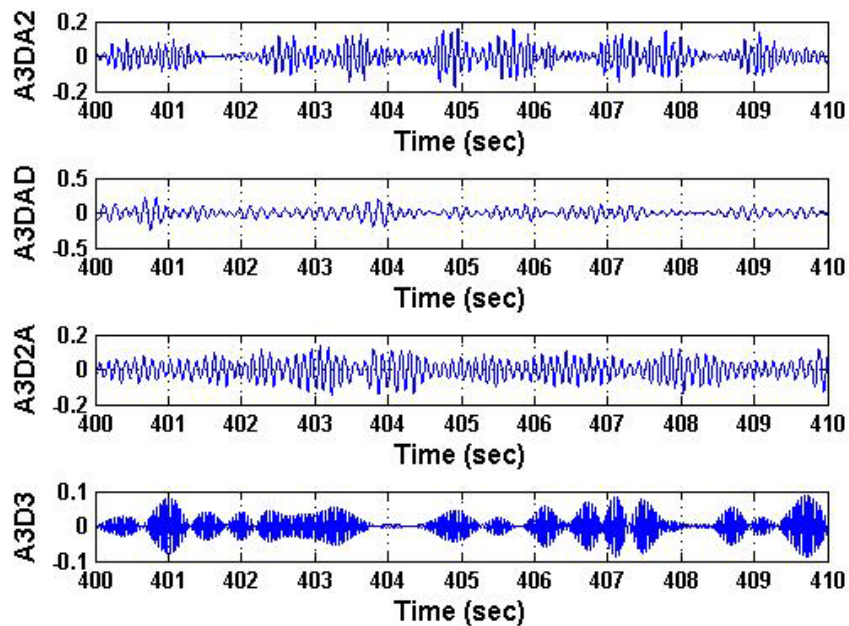


b) Details Signals of Accelerometer X

**Figure 4.11: WPT Accelerometer Signal Decomposition at Level 6 under
Vibration**



a) Approximation Signals of Gyroscope Z

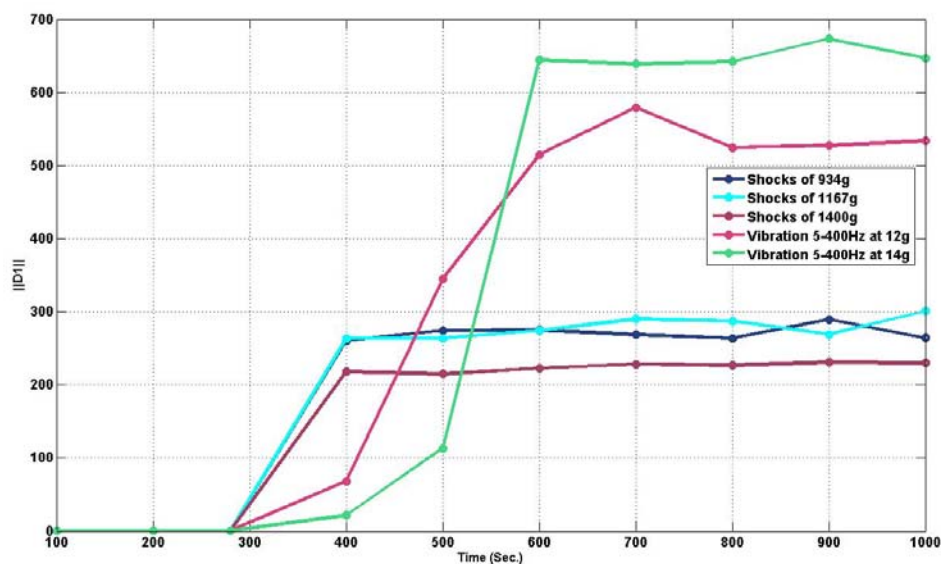


b) Details Signals of Gyroscope Z

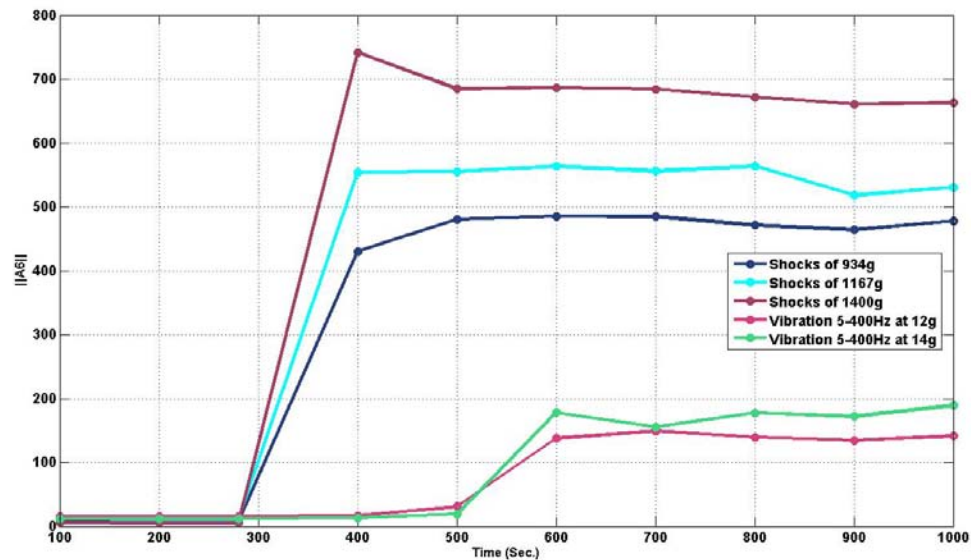
Figure 4.12: WPT Gyroscope Signal Decomposition at Level 6 under Vibration

4.3.2 Detection of Vibration Effects

Data from two vibration tests were examined. The vibration frequency ranged from 5 Hz to 400 Hz for the two tests. An acceleration peak magnitude of 12 g for the first test and 14 g for the second test were applied. The data analysis procedure applied for shock detection in section 4.2.2 was applied in this section for the vibration detection. Data for the two tests were processed using a WPT module, where the first level detail package D1 and the 6 level approximation package A6 were extracted for 10 sec windows located at the start of every 100 sec of the presented period. The norm $\|D1\|$ and $\|A6\|$ were derived and are presented in Figure 4.13 along with the previous results from the shock tests for comparison.



a) Detail D1



b) Approximation A6

Figure 4.13: Energy of Extracted Packet Detail D1 (a) and Approximation A6 (b)

It can be seen in Figure 4.13a that the norms $\|D1\|$ of the vibration tests are significantly higher than the norms of the shock tests. This is anticipated because vibration produces considerably more high frequency components than drilling shock. The higher the vibration, the higher the energy of the first level detail packet D1. However, examining the norm $\|A6\|$ in Figure 4.13b, it can be concluded that the vibration has less effect on contaminating the low frequency band of the measurements than the shock. This is implied by an energy value of less than 200 for the vibration compared to a value of higher than 600 for the high shock. It must be noted that the energy of packet A6 represents the energy of the desired useful signal as

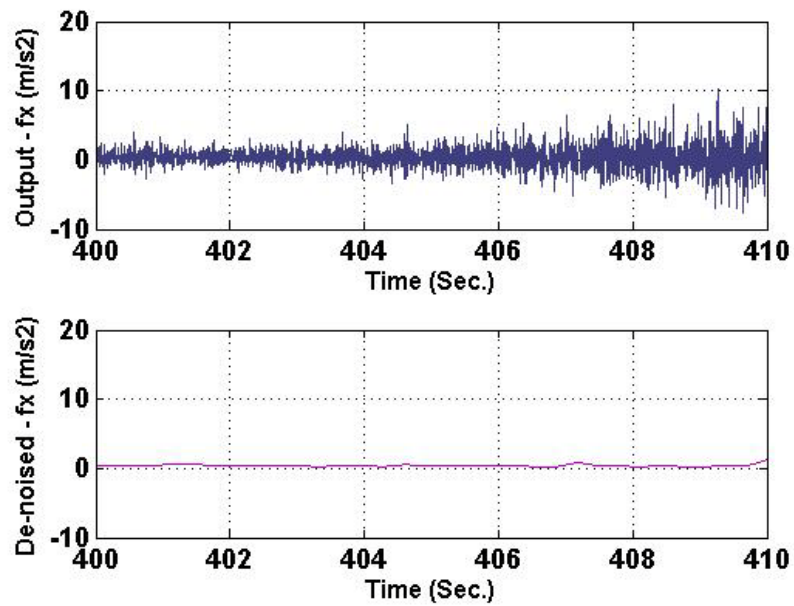
well as any undesired components. The mitigation of vibration effects is presented in the following section.

4.4 Mitigation of Harsh Drilling Environment Effects

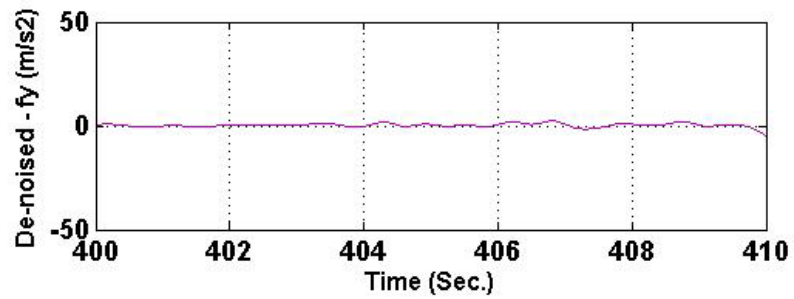
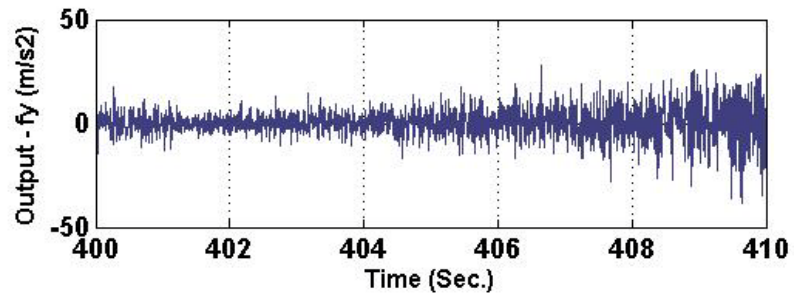
It is essential to separate and remove undesired components associated with the desired sensor signal. Drilling occurs at an average penetration rate of 10 ft/hr. Thus, it is anticipated that useful drilling motion lies within a low frequency bandwidth of 0–1 Hz. It is proposed to utilize WMRA for this purpose, where it is employed as a low-pass band filter in order to filter out high frequency components. The main difference between WMRA and the WPT is that WMRA decomposes the approximation only at a given level. A WPT decomposes both the approximation and the detail which is more suitable for analysis of the decomposed signal.

For sensor data sets collected at a data rate of 200 Hz, WMRA was set to decompose the signal into 6 levels. The reconstructed signal included only the approximation signal at the 6th level A_6 . This guaranteed that only frequency components of less than 1.56 Hz would be considered and higher frequency components would be filtered out. Measurements from the 3 accelerometers and 3 gyroscopes' MEMS sensors were analyzed over a 10 sec interval. The analyzed period captured the beginning of the applied vibration with a frequency range of 5 Hz to 400 Hz and an acceleration peak magnitude of 14 g.

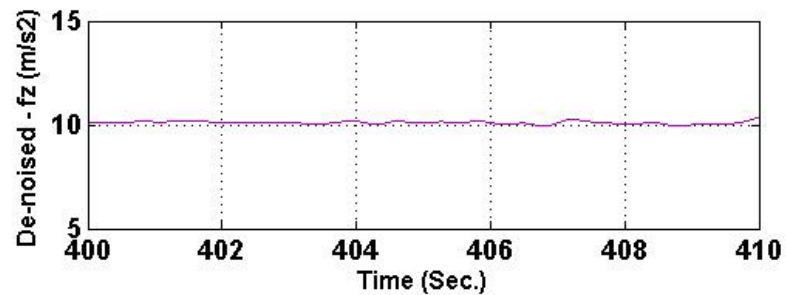
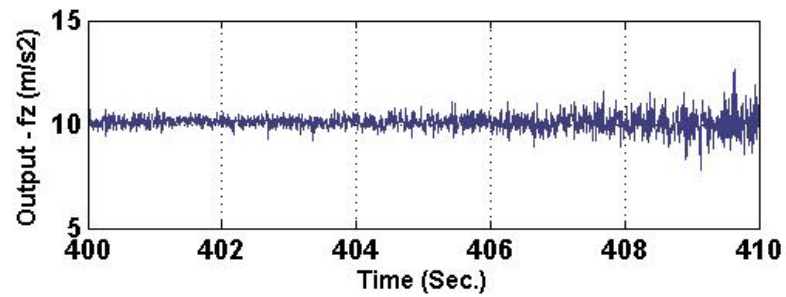
Results for the accelerometer measurements are shown in Figure 4.14, while results for the gyroscope measurements are presented in Figure 4.15. For each plot, the upper panel represents the raw signal over the analyzed interval. The lower panel represents the WMRA reconstructed signal based on the 6th level approximation window A_6 .



a) Accelerometer X



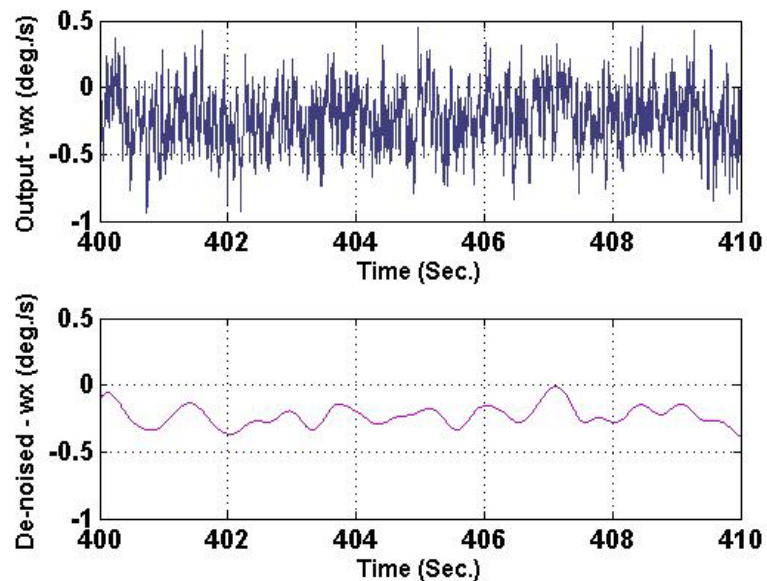
b) Accelerometer Y



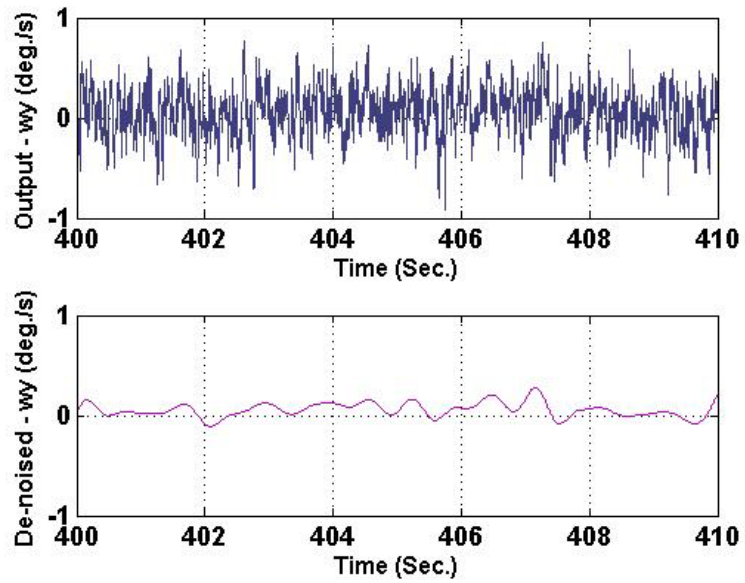
c) Accelerometer Z

Figure 4.14: MEMS Accelerometer Output Signals Under Vibration (upper panel), Denoised Signals (lower panel)

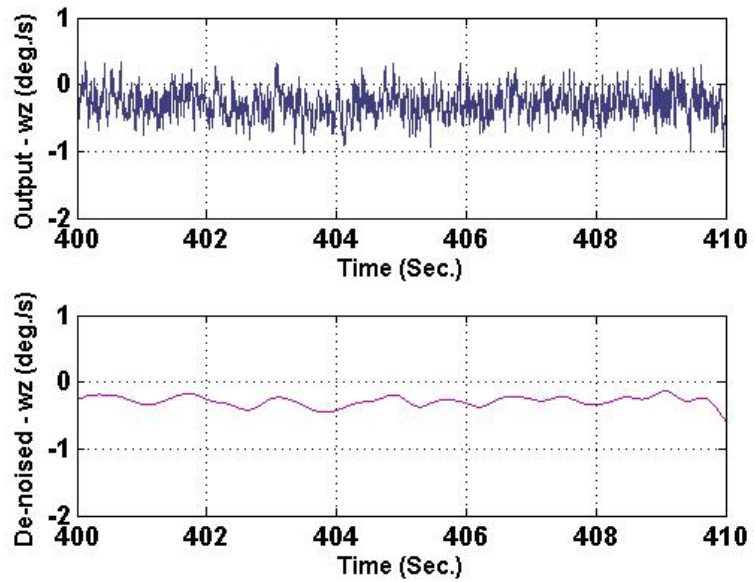
During the 10 sec period analyzed, the standard deviations (σ) of the raw measurements from the 6 sensors were compared to the standard deviation of the same measurements after WMRA processing. Results are summarized in Table 4.2, and they show a significant improvement in the signal σ for both gyroscopes and accelerometers. The signal output uncertainties of the gyroscopes was reduced to 0.075 %/s, 0.071 %/s, and 0.072 %/s from 0.224 %/s, 0.244 %/s, and 0.216 %/s for gyroscopes x, y, and z, respectively. Accelerometer signal output uncertainties before applying the WMRA algorithm were 1.72 m/s², 7.02 m/s², and 0.36 m/s². These values were reduced to 0.13 m/s², 0.86 m/s², and 0.06 m/s² after applying the WMRA algorithm. Reducing the sensor output uncertainty is vital in order to minimize the attitude errors as well as to minimize the derived position of the well bore trajectory.



a) Gyroscope X



b) Gyroscope Y



c) Gyroscope Z

**Figure 4.15: MEMS Gyroscope Output Signals under Vibration (upper panel),
Denoised Signals (lower panel)**

The utilized horizontal vibration table for this test produces vibration on the horizontal plane, particularly in the y-direction. Therefore, accelerometer y observed the most vibration, while accelerometer x observed relatively less vibration. Accelerometer z observed the least vibration. The vibration had similar effects on each of the three gyroscopes as the vibration table induces rapid linear accelerations that do not affect any particular gyroscope more than the others.

Table 4.2: Signal Output Uncertainty of Raw and Filtered Measurements

	Gyro- x°/s	Gyro- y°/s	Gyro- z°/s	Acc- x m/s ²	Acc- y m/s ²	Acc- z m/s ²
Raw signal σ	0.224	0.244	0.216	1.72	7.02	0.36
Filtered Signal σ	0.075	0.071	0.072	0.13	0.86	0.06
% Improvement	66	70	66	91	87	81

4.5 Summary

Shock and vibration are the main causes of MWD and RSS tool failure while drilling. They cost drilling operations millions of dollars in repairs and in nonproductive rig time. When shock and vibration occur while drilling, there is not much information about them on the surface at the driller consol. If information is available about shock and vibration levels while drilling, mitigating actions can be taken to reduce their costly effects. This study introduced a technique to detect shock and vibration levels

based on wavelet packet transform analysis of sensor measurements. Low, medium, and high shock levels can be detected. Drilling parameters such as weight-on-bit and torque can then be adjusted accordingly. In a case of vibration, MEMS sensor measurements can be processed through a WMRA module to filter out high frequency components and to reduce sensor output uncertainty. This technique improved accelerometer measurements by an average of 87%; gyroscope measurements were improved by an average of 67% using WMRA. In the following section, measurements from gyroscopes and accelerometers are integrated to provide a continuous well trajectory while drilling based on strap down inertial navigation systems and Kalman filtering.

CHAPTER FIVE:

CONTINUOUS WELL TRAJECTORY WHILE

DRILLING BASED ON KALMAN FILTERING

5.1 Current Industrial Well Trajectory Computation while Drilling

Current MWD surveying is performed along the well path at stationary survey stations. The well path computation is based on three measurements repeated at each surveying station. They are the drilled length, inclination, and azimuth. In addition, the orientation of the survey instrument inside the hole (toolface) is determined after deviating from the vertical direction of the well. At each surveying station, the azimuth and inclination define a vector tangent to the well path at that point. Between the two surveying points, the different computation methods include different hypotheses about the shape of the well between the two points. The position of the second survey is computed if the position of the first survey is known. The most common well path computation methods are [FOGIA, 1990]:

Tangential method: This assumes the wellbore course is tangential to the lower survey station, and the wellbore course is a straight line. It was reported that this method gives the lowest level of accuracy [FOGIA, 1990].

Average angle method: The inclination and azimuth at the lower and upper survey stations are mathematically averaged, while the wellbore course is assumed to be tangential to the average inclination and azimuth.

Balanced tangential method: This method assumes the wellbore course is tangential to both the lower and upper survey stations.

Radius of curvature method: This is considered one of the most accurate methods, and it is a preferred approach to well-path calculations because of its relative simplicity and general use in the industry [McMillian, 1981]. This method assumes the wellbore course between the two survey stations is a smooth arc. The curvature of the arc is determined by measuring inclinations and azimuths at the two survey stations.

Minimum curvature method: This method is based on the same assumption as the radius of curvature method. The difference is that the minimum curvature method uses the same equations as the balanced tangential method multiplied by a certain ratio.

The position of the drill bit is determined, afterwards, by incorporating the drill bit orientation angles and assuming a certain trajectory between the surveying stations.

The two most accurate and common approaches are the radius of curvature method [McMillian, 1981] and the minimum curvature method (MCM) [Mason and Taylor, 1971]. The radius of curvature method assumes the well bore course between the two survey stations is a smooth arc. The minimum curvature method assumes the two

surveying stations lie on a circular arc and this arc is located in a plane for which the orientation is known at both ends by knowing the inclination and direction angles.

Figure 5.1 illustrates the MCM.

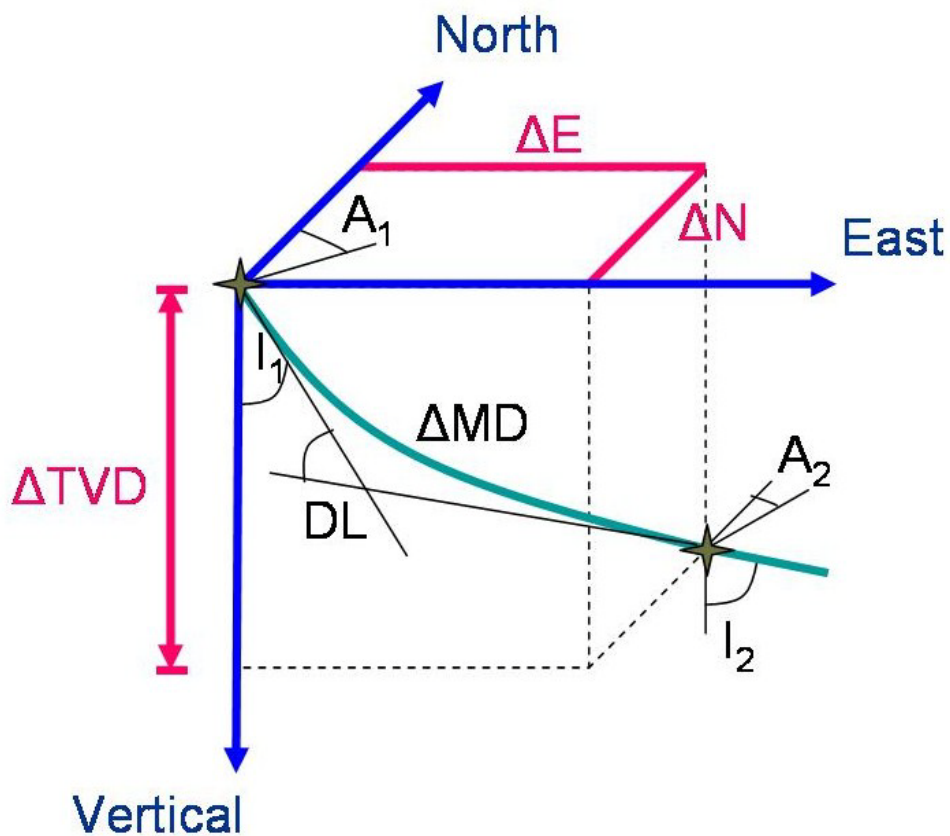


Figure 5.1: MCM Stationary Survey

When the drilling operation stops to connect a new pipe stand, the stationary surveying takes place in order to drive the inclination and direction of the drill bit. In Figure 5.1, inclination and direction at station 1 are denoted as I_1 and A_1 , respectively, while the inclination and direction at station 2 are denoted as I_2 and A_2 , respectively. The drilled distance (measured depth) is denoted ΔMD . The MCM fits a

spherical arc between the two stations by calculating the curvature “DL” from the 3D vectors and scaling by a ratio factor (RF). When the first station coordinates are known, the second station coordinates can be computed using the following expressions [Mason and Taylor, 1971]:

$$DL = \arccos(\cos(I_2 - I_1) - \sin I_1 \sin I_2 (1 - \cos(A_2 - A_1))), \quad 5.1$$

$$RF = 2 \tan(DL/2) / DL, \quad 5.2$$

$$\Delta TVD = 1/2 \Delta MD (\cos I_1 + \cos I_2) RF, \quad 5.3$$

$$\Delta N = 1/2 \Delta MD (\sin I_1 \cos A_1 + \sin I_2 \cos A_2) RF, \quad 5.4$$

$$\Delta E = 1/2 \Delta MD (\sin I_1 \sin A_1 + \sin I_2 \sin A_2) RF, \quad 5.5$$

where ΔTVD is the difference in the true vertical depth between the two stations, ΔN and ΔE are the difference in the north and east directions, respectively. This is used in a later stage of this research as a continuous position update. Additionally, it is used as a stationary position update when the drilling operation frequently stops.

5.2 Continuous Well Trajectory while Drilling Based on the INS Mechanization

As described in the previous section, the current method to compute the well trajectory in the industry is based on stationary surveys at the desired station. This is done by measuring the inclination and the azimuth of the borehole between the current and the previously surveyed stations. Using a mathematical model based on assumptions of the shape of the drilled section, the coordinates of the borehole can be derived. This

current method neglects the actual trajectory between the two surveying stations. This is due to the limitation of the magnetometers in providing a continuous survey.

Exploration and production companies demand cost effective drilling operations. Thus in the recent years, demand has been rising for a continuous survey that captures the actual trajectory between the stationary surveying stations. This allows a better estimation of the casing and cementing of the borehole. In addition, it provides an actual estimate of the curvature “doglog” along the well trajectory. Therefore, in this research the wellbore trajectory between the two surveying stations is continuously surveyed using a triad of accelerometers and a triad of gyroscopes. The computation algorithm is based on strapdown INS mechanization and Kalman filtering.

5.2.1 Mechanization Equations

INS mechanization equations are implemented to derive a continuous wellbore trajectory. The inputs to the mechanization equations are the accelerometer and gyroscope sensor measurements, while the outputs are position, velocity, and attitude of the platform where the inertial sensors are installed [Titterton and Weston, 1997]. INS mechanization equation outputs are derived with respect to a specific reference frame.

When installing the inertial sensors inside the rotary steerable system closely behind the drill bit, the accelerometer triad measures the accelerations of the drill bit in three orthogonal directions, the directions of the sensitive axes of the accelerometers which

coincide with the axes of the rotary steerable system. At this stage, all measurements will be taken in reference to these axes which are known as the body frame.

In addition to accelerometer measurements, gyroscope measurements are essential to determine the orientation of the drill bit with respect to the navigation frame. This is achieved by integration of the gyroscope measurements and knowledge of the initial attitude angles which are the pitch, roll, and azimuth [Titterton and Weston, 1997]. The attitude angles need to be known in order to transform the accelerometer measurements from the body frame to the navigation frame. If the initial velocity of the drill bit in the three orthogonal directions is known, the continuous velocities in the navigation frame can be determined by the time integral of each transformed acceleration component. The second integration derives the drill bit position in the navigation frame with respect to the initial position.

It must be noted that accelerometer readings are contaminated by the earth's gravitational field. The acceleration of gravity is added to the accelerometer measurements. Therefore, it is crucial to know the exact acceleration of the earth's gravity at the location where the accelerometer will be run. This will separate the acceleration due to the earth's gravitational force from the acceleration due to the drill string motion.

5.2.2 Computational Coordinates Frames

The accelerometer and gyroscope sensors are mounted inside the rotary steerable system collar and their sensitive axes are aligned toward the forward direction (y), the transverse direction (x), and the (z) direction perpendicular to the xy plane. These three axes form the body frame (b-frame). Illustration of the b-frame inside the rotary steerable system collar is presented in Figure 5.2. Therefore, the original accelerometer and gyroscope measurements represent the linear acceleration and angular velocities in the b-frame. However, the measurements have to be transformed into another coordinate frame (reference frame) in order to provide the position, velocity, and attitude of the moving drill bit and drill collars.

Three reference frames are frequently used in the inertial navigation. They are the navigation frame (local level frame), the earth-fixed terrestrial frame, and the inertial frame [Salychev, 1998; Schwarz and Wei, 1999]. The earth-fixed terrestrial frame X^e -axis points toward the Greenwich meridian direction in the equatorial plane. The Y^e -axis points at 90° east of the Greenwich meridian direction in the equatorial plane. Finally, the Z^e -axis points along the earth's polar axis. The earth-fixed frame is illustrated in Figure 5.3.

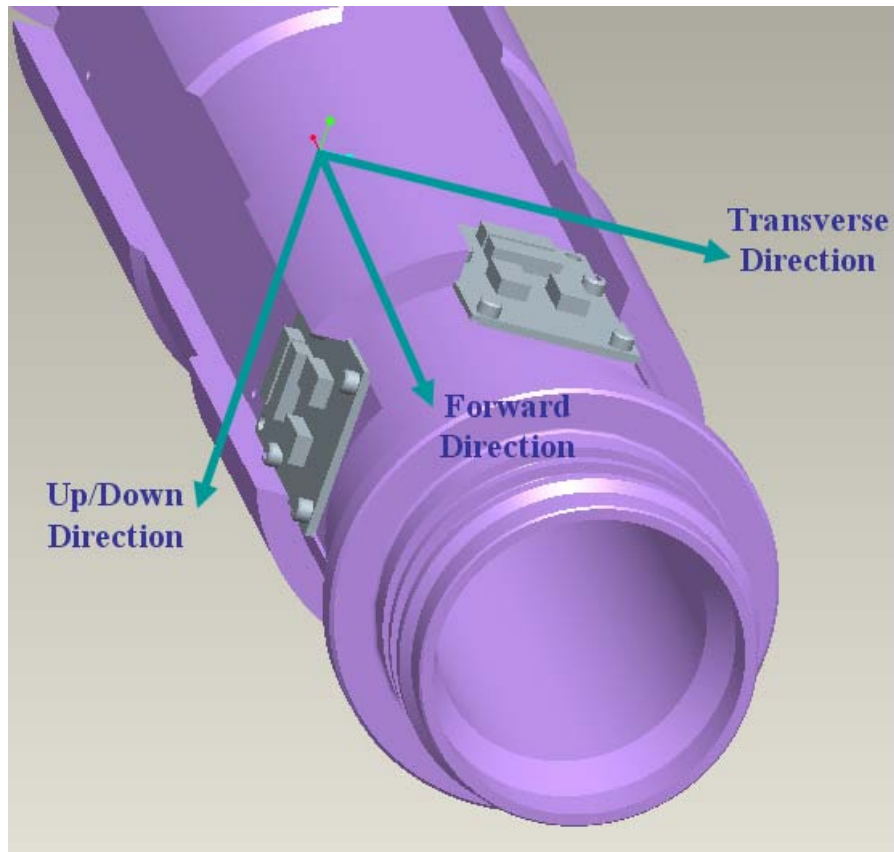


Figure 5.2: Body Frame (Drill String Frame) Axes of the Rotary Steerable System

The navigation reference frame n-frame is used for the position, velocity, and attitude computations, because its axes are aligned to the local north, east, and vertical directions. The Y^n -axis of the n-frame points toward the geodetic north, the X^n -axis points toward the east direction, and the Z^n -axis points upward and orthogonal to the reference ellipsoid of the earth. Figure 5.3 presents the n-frame relative to the earth-fixed frame where λ represents the longitude angle and φ represents the latitude angle.

By selecting the n-frame, the azimuth, inclination, and toolface angles of the drill collar are obtained directly as outputs of the INS mechanization equation in the n-frame. Another advantage of using the n-frame is the effect of the Schuler loop in the n-frame. The computational errors of the navigation parameters in the north-east plane are bound [Titterton and Weston, 1997; Schwarz and Wei, 1999; Mohammed, 1999] where they are coupled together and produce the Schuler loop. These errors oscillate with a Schuler frequency of 1/5000 Hz.

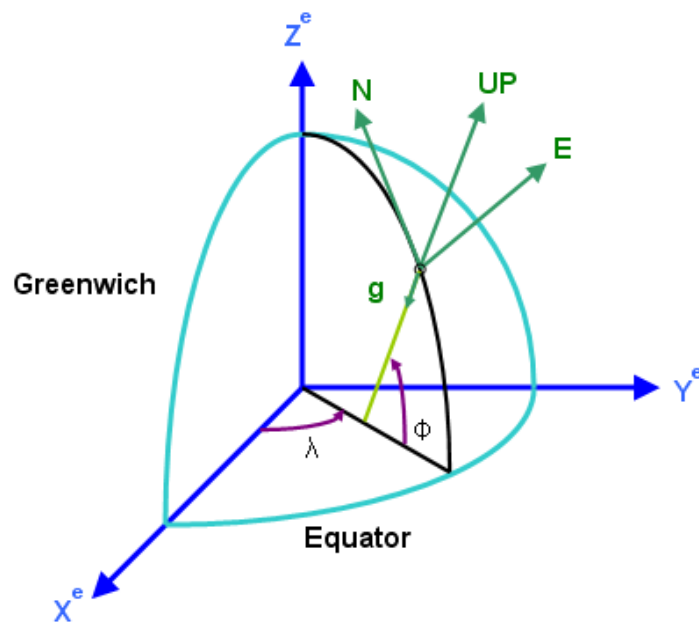


Figure 5.3: Navigation Frame (N, E, and UP) of a Given Point relative to the Earth-Fixed Frame

5.2.3 Transformation between Navigation Frame and Body Frame

As stated earlier, accelerometer and gyroscope measurements are taken in the body frame (b-frame). The matrix R_b^n is used to transform these measurements into the navigation frame. R_b^n is a combination of azimuth (ψ), pitch (θ), and toolface (ϕ) angles; it is expressed as follows [Schwarz and Wei, 1999]:

$$R_b^n = \begin{pmatrix} \cos \psi \cos \phi + \sin \psi \sin \theta \sin \phi & \sin \psi \cos \theta & \cos \psi \sin \phi - \sin \psi \sin \theta \cos \phi \\ -\sin \psi \cos \phi + \cos \psi \sin \theta \sin \phi & \cos \psi \cos \theta & -\sin \psi \sin \phi - \cos \psi \sin \theta \cos \phi \\ -\cos \theta \sin \phi & \sin \theta & \cos \theta \cos \phi \end{pmatrix}. \quad 5.6$$

Accordingly, transformation of the measurements from n-frame to b-frame can be implemented by using the inverse of the transformation matrix R_b^n .

$$R_n^b = (R_b^n)^{-1} \quad 5.7$$

5.2.4 Modeling Motion in Navigation Frame

The INS mechanization equations in the navigation frame are obtained as follows [El-Sheimy, 2004]:

$$\begin{pmatrix} \dot{r}^n \\ \dot{V}^n \\ \dot{R}_b^n \end{pmatrix} = \begin{pmatrix} D^{-1}V^n \\ R_b^n f^b - (2\Omega_{ie}^n + \Omega_{en}^n)V^n + g^n \\ R_b^n (\Omega_{ib}^b - \Omega_{in}^b) \end{pmatrix}. \quad 5.8$$

solution of INS mechanization equations by the quaternion approach is discussed in Appendix B.

5.2.5 Directional Drilling Parameter Computations

This section provides a step by step computation of the continuous drill collar position, velocity, and attitude angles at any time while drilling based on the previous mathematical relationships. The inertial measurements unit provides three angular velocity $\omega_{ib}^b = (\omega_x, \omega_y, \omega_z)^T$ and three acceleration $f^b = (f_x, f_y, f_z)^T$ measurements measured in the tool body frame. The angular increments $\theta_{ib}^b = (\Delta\theta_x, \Delta\theta_y, \Delta\theta_z)^T$ can then be determined using the angular velocity measurements as follows:

$$\theta_{ib}^b = \begin{pmatrix} \Delta\theta_x \\ \Delta\theta_y \\ \Delta\theta_z \end{pmatrix}_{ib}^b = \begin{pmatrix} \omega_x \\ \omega_y \\ \omega_z \end{pmatrix} \Delta t, \quad \mathbf{5.9}$$

where Δt is the inverse of the data rate. The linear velocity increments $(\Delta v_x, \Delta v_y, \Delta v_z)$ are obtained similarly using the three acceleration measurements as follows:

$$\Delta v^b = \begin{pmatrix} \Delta v_x \\ \Delta v_y \\ \Delta v_z \end{pmatrix} = \begin{pmatrix} f_x \\ f_y \\ f_z \end{pmatrix} \Delta t. \quad \mathbf{5.10}$$

The derived angular increments capture the drill collar angular increments in addition to the earth's rotation and the change of orientation of the navigation frame with respect to the earth-fixed frame. The last two effects must be taken into account. Their expression ω_{in}^b is derived in Equation 5.11. The angular increments can then be presented at a given time t_k as in the following expression:

$$\theta_{in}^b(t_k) = \omega_{in}^b(t_k)\Delta t = R_n^b(t_k) \begin{pmatrix} \frac{-V^n(t_k)}{M+h} \\ \frac{V^e(t_k)}{N+h} + \omega^e \cos \varphi \\ \frac{V^e(t_k) \tan \varphi}{N+h} + \omega^e \sin \varphi \end{pmatrix} \Delta t. \quad 5.11$$

It is possible now to determine the actual angular increment of the drill string at a given time $\theta_{nb}^b(t_k)$ by subtracting and compensating for $\theta_{in}^b(t_k)$ from the original $\theta_{ib}^b(t_k)$ as follows:

$$\theta_{nb}^b(t_k) = \theta_{ib}^b(t_k) - \theta_{in}^b(t_k) = \begin{pmatrix} \Delta\theta_x \\ \Delta\theta_y \\ \Delta\theta_z \end{pmatrix}. \quad 5.12$$

The following step updates the quaternion vector. The initial quaternion vector $Q(t_0)$ is computed using the initial rotation matrix $R_b^n(t_0)$ derived from the initial alignment

during a stationary period. The quaternion vector is updated by using Equation 5.13 applied as:

$$\begin{pmatrix} q_1(t_{k+1}) \\ q_2(t_{k+1}) \\ q_3(t_{k+1}) \\ q_4(t_{k+1}) \end{pmatrix} = \begin{pmatrix} q_1(t_k) \\ q_2(t_k) \\ q_3(t_k) \\ q_4(t_k) \end{pmatrix} + \frac{1}{2} \begin{pmatrix} 0 & \Delta\theta_z & -\Delta\theta_y & \Delta\theta_x \\ -\Delta\theta_z & 0 & \Delta\theta_x & \Delta\theta_y \\ \Delta\theta_y & -\Delta\theta_x & 0 & \Delta\theta_z \\ -\Delta\theta_x & -\Delta\theta_y & -\Delta\theta_z & 0 \end{pmatrix} \begin{pmatrix} q_1(t_k) \\ q_2(t_k) \\ q_3(t_k) \\ q_4(t_k) \end{pmatrix}. \quad 5.13$$

The updated rotation matrix R_b^n is determined afterward from the direct relationship with the updated quaternion vector in Equation 5.13. Finally the azimuth Ψ , tool face ϕ , and pitch θ (90 - inclination I) of the drill string can be derived using the relationship explained previously in section 5.2.3. As a result they are obtained using the following expressions:

$$\Psi = \arctan\left(\frac{-r_{12}}{r_{22}}\right), \quad 5.14$$

$$\phi = \arctan\left(\frac{r_{31}}{r_{33}}\right), \quad 5.15$$

$$I = 90 - \theta = 90 - \arctan\left(\frac{r_{32}}{\sqrt{r_{12}^2 + r_{22}^2}}\right). \quad 5.16$$

The following step updates the velocity components at t_{k+1} . This can be accomplished by using Equation 5.10 and Equation 5.17 to determine drill string velocity changes along the navigation frame as follows:

$$\Delta V^n(t_{k+1}) = R_b^n \Delta v^b - (2\Omega_{ie}^n + \Omega_{en}^n) V^n \Delta t + g^n \Delta t. \quad 5.17$$

Finally, the updated velocity components $V^n = (V^{east} \quad V^{north} \quad V^{up})$ at t_{k+1} are derived using a direct relationship with $\Delta V^n(t_{k+1})$:

$$V^n(t_{k+1}) = V^n(t_k) + \frac{1}{2} (\Delta V^n(t_k) + \Delta V^n(t_{k+1})). \quad 5.18$$

The updated positions (latitude φ , longitude λ , and true vertical depth h) of the drill string at t_{k+1} are computed using modified Euler formulas. h is computed using the relationship with the vertical component of the velocity vector in Equation 5.18. It is expressed as:

$$h(t_{k+1}) = h(t_k) + \frac{1}{2} (V^{up}(t_k) + V^{up}(t_{k+1})) \Delta t. \quad 5.19$$

Equations 5.20 and 5.21 compute the drill string latitude φ , longitude λ , at t_{k+1} :

$$\varphi(t_{k+1}) = \varphi(t_k) + \frac{1}{2} \frac{(V^{north}(t_k) + V^{north}(t_{k+1}))}{M + h} \Delta t, \quad 5.20$$

$$\lambda(t_{k+1}) = \lambda(t_k) + \frac{1}{2} \frac{(V^{east}(t_k) + V^{east}(t_{k+1}))}{(N + h)\cos\varphi} \Delta t. \quad 5.21$$

The continuous update of the drill string position, velocity, and attitude angles are computed using the measurements from the accelerometer triad and the gyroscope triad without regard to contaminating errors. However, the long term accuracy deteriorates due to integration of accelerometer and gyroscope sensor errors and computational errors. Modelling of these errors is discussed in section 5.3.

5.2.6 Drill Bit Synthetic Attitude Angles

In a stationary mode, the pitch and toolface of the drill bit can be derived using only accelerometer measurements based on the following relationship between the accelerometer measurement vector f^b and the gravity vector g^n :

$$f^b = \begin{pmatrix} f_x \\ f_y \\ f_z \end{pmatrix} = R_n^b g^n = R_n^b \begin{pmatrix} 0 \\ 0 \\ -g \end{pmatrix}, \quad 5.22$$

where gravity vector g^n is derived from the normal gravity model described in Appendix A, Equation A.8. The rotation matrix R_n^b transforms the gravity vector

defined in the n-frame into the b-frame and it is expressed as in Equation 5.7.

Accelerometer measurement vector f^b can be written as:

$$f_x = g \cos \theta \sin \phi, \quad 5.23$$

$$f_y = -g \sin \theta, \quad 5.24$$

$$f_z = -g \cos \theta \cos \phi. \quad 5.25$$

According to Equations 5.23, 5.24, and 5.25, the pitch θ and toolface ϕ angles can be derived as:

$$\sin \theta = -\frac{f_y}{g}, \quad 5.26$$

$$\tan \phi = -\frac{f_x}{f_z}. \quad 5.27$$

When the drill bit rate of penetration is very slow, synthetic pitch and toolface angles can be derived by using only the accelerometer measurements as shown in Equations 5.26 and 5.27. The comparison with drill bit pitch and toolface reference angles is presented and discussed in a later section of this chapter.

5.3 Surveying Error Modelling Using Linear State Equations

Surveying errors must be estimated to a certain level in order to achieve an acceptable system performance. Given the nonlinear nature of the system, the system is perturbed

in order to derive a set of linear differential equations. This is done using the linearization approach of the nonlinear dynamic system [Schwarz and Wei, 1999; Jekeli, 2000]. Derivation of the surveying errors of the coordinate errors $(\delta\varphi, \delta\lambda, \delta h)$, velocity errors $(\delta V^e, \delta V^n, \delta V^u)$, and attitude errors $(\delta\theta, \delta\phi, \delta\psi)$ is discussed in Appendix C.

Inertial sensor measurements contain biases and constant drifts defined as the deterministic parts, which are determined by field calibration. The remaining errors are considered random and modelled as stochastic processes, where these errors are correlated in time and modelled as first order Gauss-Markov (GM) processes. Sensor random errors are discussed in Appendix C. Measurement errors of the inertial sensors are known to drift with time in the absence of external measurement updates. This error growth is limited by applying an optimal estimation tool such as Kalman filtering.

5.4 Kalman Filtering to Limit Error Growth of Inertial Sensor Measurements

5.4.1 Kalman Filtering Algorithm

The Kalman filter is a computational algorithm that deduces a minimum error estimate of the state of a system by considering the dynamics of the system, characteristics of the system noise, measurements errors, and the initial condition information [El-Sheimy, 2003]. Inertial sensor errors and surveying errors are combined to form the error state vector χ_k at time t_k :

$$\chi_k = (\delta\varphi \quad \delta\lambda \quad \delta h \quad \delta V^e \quad \delta V^n \quad \delta V^u \quad \delta\theta \quad \delta\phi \quad \delta\psi \quad \delta\omega_x \quad \delta\omega_y \quad \delta\omega_z \quad \delta f_x \quad \delta f_y \quad \delta f_z)$$

5.28

The random processes associated with the components of the error state vector χ are modelled using the following discrete state space representation:

$$\chi_k = F_{k,k-1}\chi_{k-1} + G_{k-1}w_{k-1},$$

5.29

where $F_{k,k-1}$ is the state transition (dynamics) matrix that relates χ_{k-1} to χ_k . The system noise is defined by w_{k-1} , while G_{k-1} is the noise coefficient matrix. In order to provide an optimal estimation of the error states χ_k , external measurements or observations Z of high accuracy have to be utilized. The observation of the discrete system can be represented in the following relationship:

$$Z_k = H_k\chi_k + v_k,$$

5.30

where H_k is the design matrix that holds a noiseless relationship between the observation vector Z_k and the error state vector χ_k . The observations random noise vector v_k is assumed to be a white sequence not correlated with the system

measurement noise w_k . The covariance matrices of the measurement noise sequence w_k and the observation noise sequence v_k are expressed as:

$$E[w_k w_i^T] = \begin{cases} Q_k & i = k \\ 0 & i \neq k \end{cases}, \quad 5.31$$

$$E[v_k v_i^T] = \begin{cases} R_k & i = k \\ 0 & i \neq k \end{cases}, \quad 5.32$$

$$E[w_k v_i^T] = 0 \text{ for all } i \text{ and } k. \quad 5.33$$

The error covariance matrix of the estimate of the error state vector χ_k is given as:

$$E[(\hat{\chi}_k - \chi_k)(\hat{\chi}_k - \chi_k)^T] = P_k, \quad 5.34$$

where $\hat{\chi}_k$ is the estimated error state at time t_k . The mean square estimation error (MSEE) of each error state is presented along the diagonal elements of the error covariance matrix P_k .

While drilling, the diagonal elements of P_k are checked to verify the convergence of error states toward the minimal MSEE. If the error state is strongly observed by external observations, errors are optimally estimated by the Kalman filter and convergence to the minimum MSEE occurs in a short time. However, if the error state is weakly observed by external observations, errors might be optimally estimated but it

takes a long time to converge toward the minimum MSEE. In some cases, the error state cannot be optimally estimated if the state is unobservable by external observations; thus the corresponding MSEE diverges because there is no optimal estimate of this error state [Brown and Hwang, 1997].

The sequential recursive algorithm of Kalman filtering for the optimal least mean variance estimation of the error states is best described by the following block diagram:

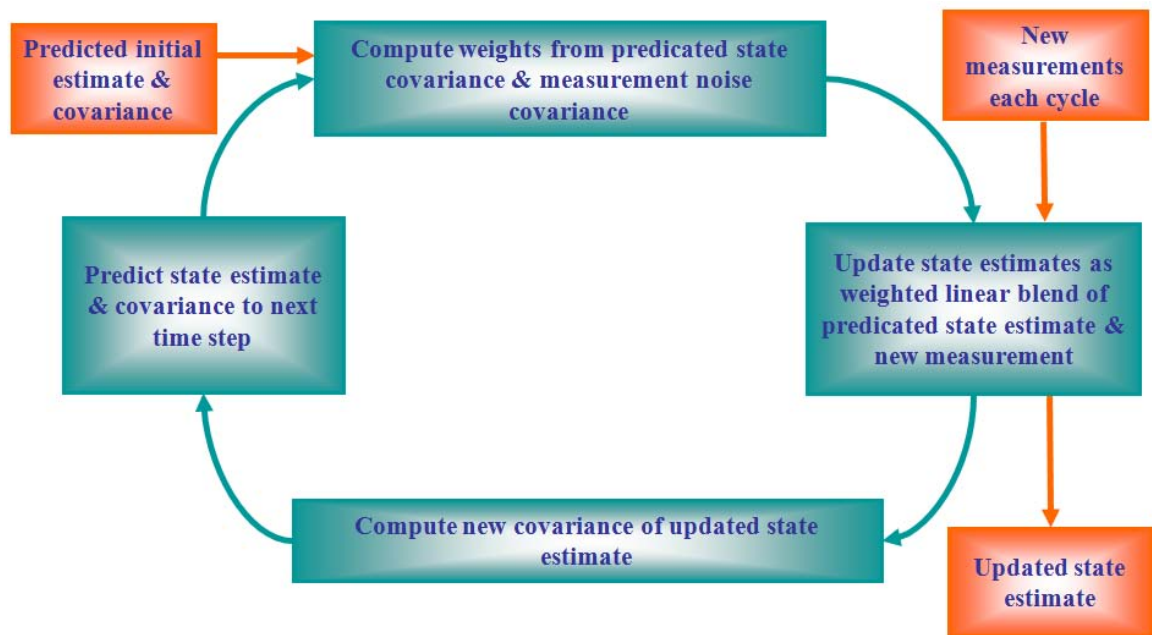


Figure 5.5: Block Diagram of the Kalman Filtering Sequential Recursive Algorithm

Kalman filtering starts by obtaining a prediction $\hat{\chi}_k(-)$ of the error state χ_k based on the estimation of previous error states $\hat{\chi}_{k-1}(+)$. The error estimate $\hat{\chi}_k(+)$ at the present time instant t_k is estimated by updating the apriori estimate $\hat{\chi}_k(-)$ using the following relationship [Gelb, 1974]:

$$\hat{\chi}_k(+) = \hat{\chi}_k(-) + K_k(Z_k - H_k \hat{\chi}_k(-)), \quad 5.35$$

where K_k is the Kalman gain matrix computed as:

$$K_k = P_k(-)H_k^T(H_k P_k(-)H_k^T + R_k)^{-1}. \quad 5.36$$

The error covariance matrix $P_k(+)$ of the estimate $\hat{\chi}_k(+)$ is derived using the following expression:

$$P_k(+) = [I - K_k H_k] P_k(-). \quad 5.37$$

The updated error covariance matrix $P_k(+)$ depends on the predicted error covariance matrix $P_k(-)$ associated with the predicted error state $\hat{\chi}_k(-)$. The error covariance matrix $P_k(-)$ relies on the error covariance matrix $P_{k-1}(+)$ determined at instant time t_{k-1} , and is predicted using the following expression:

$$P_k(-) = F_{k,k-1} P_{k-1}(+) F_{k,k-1}^T + G_{k-1} Q_{k-1} G_{k-1}^T. \quad \mathbf{5.38}$$

As mentioned earlier, during drilling, the diagonal elements of the error covariance matrix $P_k(+)$ are checked to determine either the MSEE convergence toward a minimum or divergence.

The major contributor to MSEE values is the change in the Kalman gain matrix K_k , whereas the design matrix H_k is constant throughout the drilling process. The Kalman gain K_k is directly proportional to the estimate error covariance and inversely proportional to the variance of the measurement noise [Brown and Hwang, 1997]. Thus, the Kalman gain K_k presents a ratio between the uncertainty in the state estimate and the uncertainty in observations.

If the external updates observations are of high accuracy, the observation uncertainty is small and yields a high Kalman gain and a smaller error covariance matrix $P_k(+)$. If there are no external observation updates available, measurement noise grows extremely high causing instability of error estimates and reducing the accuracy of the surveying parameters. The drilling observation updates are discussed in the following subsection.

5.4.2 Drilling Observation Updates for Kalman Filtering

The proposed drilling surveying system will exhibit an unlimited growth of position, velocity, and attitude errors if there are no external observations to update the surveying system. Two external update schemes can limit the error growth of the inertial sensor measurements while drilling. The first is based on the continuous source of drilled pipe length measurements which can be used to determine the drill bit rate of penetration. This can be further translated to the continuous velocity measurements' update of the inertial sensor measurements. Additionally, a continuous position is applied based on the position computed by the MCM as expressed in Equations 5.3–5.5. The second external update scheme is based on stationary measurements taken when the drilling operation stops on a regular basis to connect a new stand of pipes. Stationary updates are zero velocity updates (ZUPT), stationary MCM position updates, as well as magnetic heading angle updates.

The inertial sensor measurements and the observation updates are processed through the Kalman filter algorithm to optimally estimate the surveying parameters. An illustration of the directional drilling surveying system based on Kalman filtering is presented in Figure 5.6. The efficiency of these observation updates depends on the accuracy of these observations and on the how often they are available.

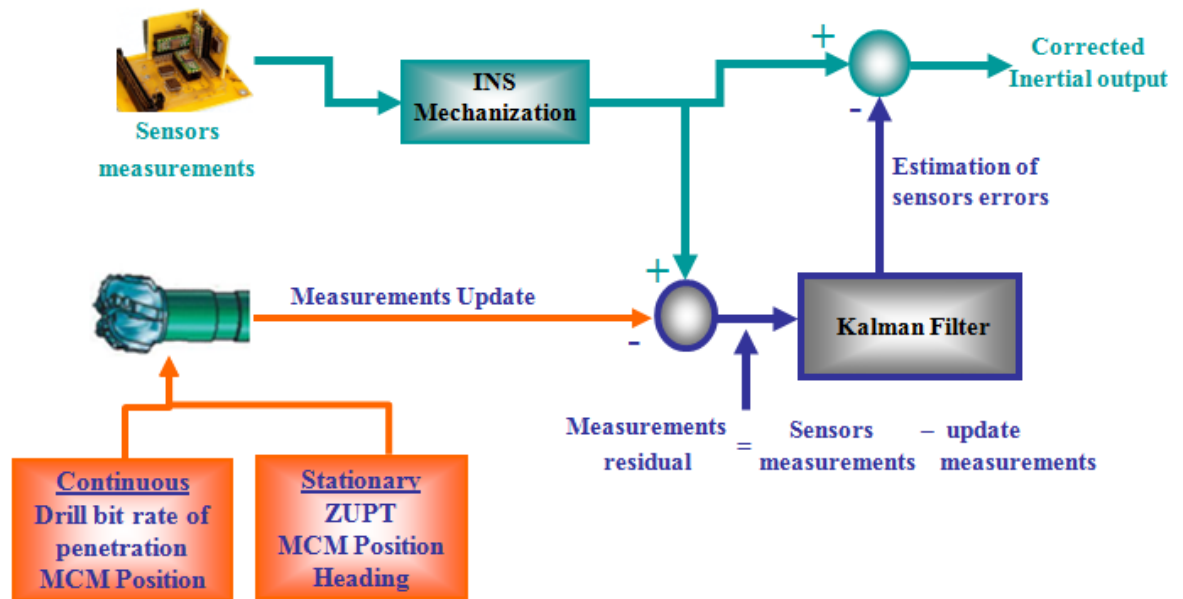


Figure 5.6: Drilling Scheme of Kalman Filtering

5.4.2.1 Continuous surveying observations updates while drilling

The rate of penetration of the drill bit while drilling is available continuously by making use of the information of the drilled pipe length and time. The drilled pipe length measurement is based on the measurements of the drill line movements by monitoring revolutions of the draw works drum to record incremental additions to the drill string. This is done with an optical encoder installed on the drum of the draw works. The pulses per foot measured by the encoder vary at each wrap on the draw works. This is compensated for by calibrating the total number of pulses per wrap to the corresponding depth variation as the block is pulled up. Depth is incremented only

when the drill pipes are moving. When making a connection while the drill string is stationary, depth updates stop [Bourgoyne et al., 2005].

The velocity obtained from the INS $(V_{INS}^e, V_{INS}^n, V_{INS}^u)$ is compared to the drill bit rate of penetration $(V_{update}^e, V_{update}^n, V_{update}^u)$. The continuous MCM position updates are based on a valid assumption that the well trajectory between the two surveying stations lies on a circular arc and position computations are based on the minimum curvature method [Mason and Taylor, 1971]. Details of MCM position computations $(\varphi_{update}, \lambda_{update}, h_{update})$ are discussed in section 5.1. Based on this information, the Kalman filter estimates the random errors within the INS output. In turn, it enhances the performance of the surveying system while drilling by removing the estimated errors from the inertial sensor measurements [El-Gizawy et al., 2006]. The observation vector Z_k is presented as:

$$Z_k = \begin{pmatrix} \varphi_{INS} - \varphi_{update} \\ \lambda_{INS} - \lambda_{update} \\ h_{INS} - h_{update} \\ V_{INS}^e - V_{update}^e \\ V_{INS}^n - V_{update}^n \\ V_{INS}^u - V_{update}^u \end{pmatrix}. \quad 5.39$$

The design matrix H_k that exhibits the noiseless relationship between the observation vector Z_k and the error state vector χ_k is written as:

$$H_k = \begin{pmatrix} \begin{pmatrix} 1 & 0 & 0 \\ 0 & 1 & 0 \\ 0 & 0 & 1 \end{pmatrix} & \mathbf{0}_{3 \times 3} & \mathbf{0}_{3 \times 3} & \mathbf{0}_{3 \times 3} & \mathbf{0}_{3 \times 3} \\ \mathbf{0}_{3 \times 3} & \begin{pmatrix} 1 & 0 & 0 \\ 0 & 1 & 0 \\ 0 & 0 & 1 \end{pmatrix} & \mathbf{0}_{3 \times 3} & \mathbf{0}_{3 \times 3} & \mathbf{0}_{3 \times 3} \end{pmatrix}. \quad 5.40$$

Substituting the values of the observation vector Z_k and the design matrix H_k into Equation 5.30 provides the Kalman filtering measurement update equation of the drill bit rate of penetration and the MCM position:

$$\begin{pmatrix} \varphi_{INS} - \varphi_{update} \\ \lambda_{INS} - \lambda_{update} \\ h_{INS} - h_{update} \\ V_{INS}^e - V_{update}^e \\ V_{INS}^n - V_{update}^n \\ V_{INS}^u - V_{update}^u \end{pmatrix}_{6 \times 1} = \begin{pmatrix} \begin{pmatrix} 1 & 0 & 0 \\ 0 & 1 & 0 \\ 0 & 0 & 1 \end{pmatrix} & \mathbf{0}_{3 \times 3} & \mathbf{0}_{3 \times 3} & \mathbf{0}_{3 \times 3} & \mathbf{0}_{3 \times 3} \\ \mathbf{0}_{3 \times 3} & \begin{pmatrix} 1 & 0 & 0 \\ 0 & 1 & 0 \\ 0 & 0 & 1 \end{pmatrix} & \mathbf{0}_{3 \times 3} & \mathbf{0}_{3 \times 3} & \mathbf{0}_{3 \times 3} \end{pmatrix}_{6 \times 15} \begin{pmatrix} \delta\varphi \\ \delta\lambda \\ \delta h \\ \delta v^e \\ \delta v^n \\ \delta v^u \\ \delta\theta \\ \delta\phi \\ \delta\psi \\ \delta\omega_{3 \times 1} \\ \delta f_{3 \times 1} \end{pmatrix}_{15 \times 1} + v_{6 \times 1} \quad 5.41$$

The second term on the right hand side represents the uncertainty of the drill bit rate of penetration and MCM position measurements. When the drilling stops in order to connect new pipe stands, stationary external observations are utilized; they are discussed in the following subsection.

5.4.2.2 Stationary surveying observation updates

In large drilling rigs, drilling has to stop every 30 meters for at least 5–10 minutes in order to connect a new drill pipe stand. In smaller drilling rigs, drilling stops every 10 meters for the same purpose. During this period, stationary measurements are applied as observations updates to the INS.

The first stationary update is the zero velocity update (ZUPT). In reality, the drill string is stationary; any velocity output of the inertial surveying system is accelerometer bias errors. This information is fed into the Kalman filter in order to estimate and remove the velocity errors. The design matrix H_k of the observations update equation is expressed in Equation 5.42, while the observation vector Z_k is expressed in Equation 5.43.

$$H_k = \begin{pmatrix} 1 & 0 & 0 & 0_{3 \times 3} & 0_{3 \times 3} & 0_{3 \times 3} \\ 0_{3 \times 3} & 0 & 1 & 0 & 0_{3 \times 3} & 0_{3 \times 3} \\ 0 & 0 & 0 & 1 & 0_{3 \times 3} & 0_{3 \times 3} \end{pmatrix} \quad \mathbf{5.42}$$

$$Z_k = \begin{pmatrix} V_{INS}^e - V_{ZUPT}^e \\ V_{INS}^n - V_{ZUPT}^n \\ V_{INS}^u - V_{ZUPT}^u \end{pmatrix} = \begin{pmatrix} V_{INS}^e - 0 \\ V_{INS}^n - 0 \\ V_{INS}^u - 0 \end{pmatrix}. \quad 5.43$$

Drill string heading observations are obtained from a magnetometer triad that is able to provide heading observations only while the drill string is stationary ($\psi_{magnetic}$). The magnetic heading is referenced to the magnetic north and the gyroscope heading is referenced to the true north, therefore, the magnetic heading has first to be corrected to reference to the true north before it is compared to the heading derived from the gyroscope. This is done by applying a magnetic declination correction to the magnetic heading. The magnetic declination is defined as the angle between the true and magnetic north as measured from the true north. Its value depends on the location and time of applying the correction; the correction is usually obtained from the British Geological Survey Global Geo-Magnetic (BGGM) Model.

The heading observation after referencing to the true north ψ_{update} is used as a direct observation update in Kalman filtering to estimate the random errors in the measurement of the inertial derived heading ψ_{INS} . The relationship between the observation vector Z_k and the error state vector χ_k are contained within the design matrix H_k as:

$$H_k = \begin{pmatrix} 0_{1 \times 3} & 0_{1 \times 3} & 0 & 0 & 1 & 0_{1 \times 3} & 0_{1 \times 3} \end{pmatrix}. \quad 5.44$$

In addition to utilizing the heading observation as a direct update, it is utilized along with the inclination of the drill string during the stationary period to compute the position coordinates of the drill string in a manner similar to the continuous MCM position update. However, during stationary periods whenever the drilling stops for addition of a new pipe stand, the MCM position $(\varphi_{update} \quad \lambda_{update} \quad h_{update})$ is computed. The design matrix H_k that conveys the relationship between the observation vector Z_k and the error state vector χ_k is:

$$H_k = \begin{pmatrix} 1 & 0 & 0 & 0_{3 \times 3} & 0_{3 \times 3} & 0_{3 \times 3} & 0_{3 \times 3} \\ 0 & 1 & 0 & 0_{3 \times 3} & 0_{3 \times 3} & 0_{3 \times 3} & 0_{3 \times 3} \\ 0 & 0 & 1 & 0_{3 \times 3} & 0_{3 \times 3} & 0_{3 \times 3} & 0_{3 \times 3} \end{pmatrix}. \quad 5.45$$

The Kalman filter performs an estimation of the random errors contaminating the inertial sensor measurements. This in turn enhances the performance of the surveying system while stationary and before commencing the drilling after the connection. For updates, the MCM position, ZUPT, and heading while stationary, the observation vector Z_k , and update expression are presented as follows:

$$\begin{pmatrix} \varphi_{INS} - \varphi_{update} \\ \lambda_{INS} - \lambda_{update} \\ h_{INS} - h_{update} \\ V_{INS}^e - V_{update}^e \\ V_{INS}^n - V_{update}^n \\ V_{INS}^u - V_{update}^u \\ \psi_{INS} - \psi_{update} \end{pmatrix}_{7 \times 1} = \begin{pmatrix} \begin{pmatrix} 1 & 0 & 0 \\ 0 & 1 & 0 \\ 0 & 0 & 1 \end{pmatrix} & \mathbf{0}_{3 \times 3} & \mathbf{0}_{3 \times 3} & \mathbf{0}_{3 \times 3} & \mathbf{0}_{3 \times 3} \\ \mathbf{0}_{3 \times 3} & \begin{pmatrix} 1 & 0 & 0 \\ 0 & 1 & 0 \\ 0 & 0 & 1 \end{pmatrix} & \mathbf{0}_{3 \times 3} & \mathbf{0}_{3 \times 3} & \mathbf{0}_{3 \times 3} \\ (0 \ 0 \ 0) & (0 \ 0 \ 0) & (0 \ 0 \ 1) & \mathbf{0}_{1 \times 3} & \mathbf{0}_{1 \times 3} \end{pmatrix}_{7 \times 15} \begin{pmatrix} \delta\varphi \\ \delta\lambda \\ \delta h \\ \delta v^e \\ \delta v^n \\ \delta v^u \\ \delta\theta \\ \delta\phi \\ \delta\psi \\ \delta\omega_{3 \times 1} \\ \delta f_{3 \times 1} \end{pmatrix}_{15 \times 1} + v_{7 \times 1}$$

5.46

The external observations random noise vector v_k includes the uncertainty in the MCM position, ZUPT, and heading updates. The setup of the tests and analyses of the results are described in section 5.5.

5.5 Setup of Soft and Hard Formation Drilling Tests

INS based directional drilling surveying systems were conducted in a laboratory environment to simulate drilled well trajectories through hard (slow drilling) and soft (faster drilling) formations. Tests were conducted at the Royal Military College of Canada in Kingston, Ontario, Canada. The test setup is illustrated in Figure 5.7–5.9, where the inertial measurement unit is mounted on the three-axis positioning and rate

turn table model 2103HT [Ideal Aerosmith, 2006]. The rotation table provides accurate rotation around inner, middle, and outer axes. This produces changes in toolface, inclination, and heading of the drill string, and thus provides the desired simulated trajectory. The rotation table was controlled through a profile mode, where it was programmed with specific rotation rates around the three axes of the rotation table. The start of the test with the drill string in the vertical position is shown in Figure 5.7. Figure 5.8 illustrates the rotation table at an orientation equivalent to drill string in an inclined section of the well. The end of the trip at the high inclined and horizontal sections of the well is demonstrated by the rate table in the orientation shown in Figure 5.9.



Figure 5.7: Drilling Simulation Test—Rotation Table in Vertical Position



Figure 5.8: Drilling Simulation Test—Rotation Table in Inclined Position



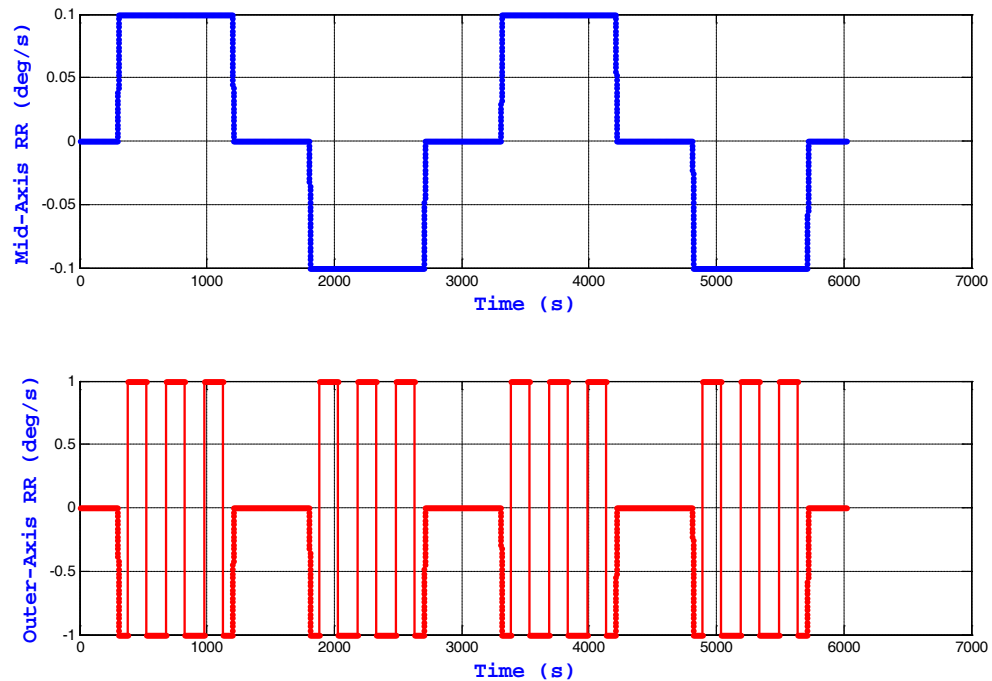
Figure 5.9: Drilling Simulation Test—Rotation Table in Highly Inclined Section

Two tests were conducted with two different trajectory profiles to simulate drilling through soft and hard formations. The two tests differed mainly on the middle axis rotation rate which represents the inclination angle build up rate. It was chosen to be 0.1 °/s for the first (soft formation) test and 0.01 °/s for the second (hard formation) test. The inclination changed from 0° to 90° for both tests.

In the first test a drilling inclination build up rate of 0.1 °/s was applied, suitable for soft formation drilling. The first test began with a 10 minute stationary period that corresponds to the required time to make a drill string connection. The rate table was programmed to perform change in the inclination angle from 0° to 9° by performing rotation at a rate of 0.1 °/s before staying stationary for 10 minutes. In practice, stationary intervals are used to connect new drilling pipes. To explore the system's long-term performance, we rotated the rate table so that it would go from 90° to 0° inclination and stay stationary for another 10 minutes. The above procedure was repeated one more time giving a total of 4 trips between 0° and 90°.

During each of the above trips, rotations along the inner axis of the rate table were performed in order to simulate changes in the toolface angle. The rotation rate was set at 1 °/s and the toolface angle was set to change 30° in 30 seconds then rotate back to the initial toolface angle in another 30 seconds. The toolface angle kept fluctuating with 30° intervals during the change of the inclination angle from 0° to 90° and back to 0°.

In a similar manner, the rotation rate of the outer axis which represents the azimuth of the drill string was set to 1 °/s, where the azimuth experienced a similar fluctuating motion, but with 75° intervals. From the initial azimuth angle, the azimuth changed 75° to the right in 75 seconds, then changed back to the initial azimuth angle in another 75 seconds. Figure 5.10 demonstrates the rotation rates along the middle, inner, and outer axes of the rate table. The upper panel presents the rotation rate of the middle axis. The middle panel shows the rotation rate of the outer axis and the lower panel demonstrates the rotation rate of the inner axis.



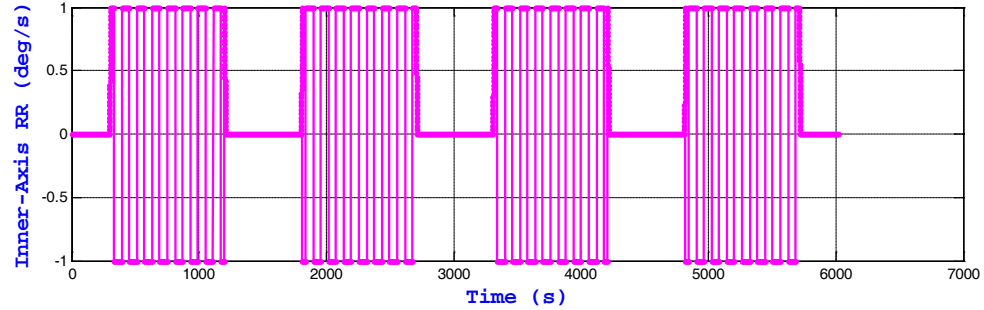


Figure 5.10: Test 1 Rotation Rates around the 3 Axes

The second test was conducted with a drilling inclination build up rate of $0.01 \text{ }^\circ/\text{s}$. This was slower than the first test and more suitable for hard formation drilling. The rotation rate of the middle axis was set to $0.01 \text{ }^\circ/\text{s}$. At this rotation rate, a period of 2.5 hours was required to drill from an inclination angle 0° to inclination angle of 90° . The rotation profile stopped for a period of 10 minutes corresponding to the time of installing a new connection to the drill pipe, then continued in the reverse direction until the inclination angle was again 0° . The outer and inner axes were changed in a manner similar to the first test throughout the entire trip. The rotation rate of the middle, outer, and inner axes are presented in Figure 5.11. The total time of the second test was 5.5 hours.

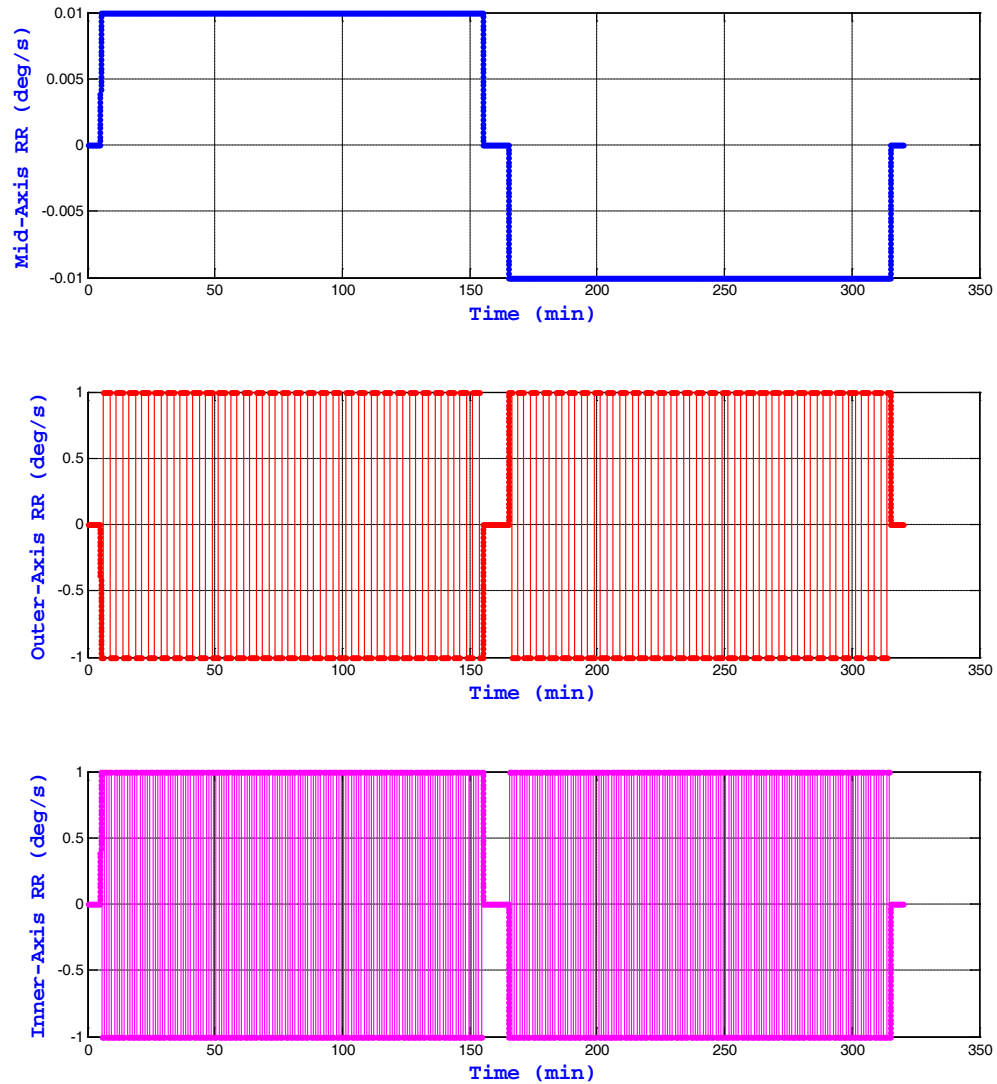


Figure 5.11: Test 2 Rotation Rates around the 3 Axes

The low cost MEMS IMU utilized in this experiment was the Crossbow IMU300CC [Crossbow, 2007]. The physical dimension of the Crossbow IMU is 3" \times 3" \times 3.2". The sensor measurements were collected at a data rate of 200 Hz and processed through a wavelet denoising module described later. The IMU specifications are listed in Table 5.1.

Table 5.1: Crossbow IMU300CC Specifications [Crossbow, 2007]

Gyro Range	$\pm 100^\circ/\text{s}$
Gyro Bias	$< \pm 2.0^\circ/\text{s}$
Gyro Scale Factor	$< 1\%$
Gyro Angle Random	$< 2.25^\circ/\sqrt{hr}$
Accelerometer Range	$\pm 2 \text{ g}$
Accelerometer Bias	$< \pm 30 \text{ mg}$
Accelerometer Scale	$< 1\%$
Accelerometer Velocity	$< 0.15 \text{ m/s}/\sqrt{hr}$
Accelerometer Linearity	$< 1\%$

The reference position, velocity, and attitude were extracted from the Honeywell HG1700 AG11 IMU installed inside the NovAtel's SPAN (Synchronized Position Attitude & Navigation) system [NovAtel, 2008]. The SPAN system was mounted on the rotation table top and ran throughout the same trajectory profiles for the two tests in order to provide an accurate reference to the Crossbow IMU. The NovAtel SPAN system integrates a GPS receiver and the HG1700 Honeywell IMU. The SPAN unit provides the position, velocity, and attitude based on a tightly coupled INS/GPS integration solution. The HG1700 IMU was mounted on the table top while the GPS antenna was mounted on the roof of the laboratory building. The HG1700 IMU specifications are summarized in Table 5.2. Analyses of the results for the tests described in this section is presented in section 5.6.

Table 5.2: HG1700 Specifications [Honeywell, 1997]

Gyro Range	$\pm 1000^\circ/\text{s}$
Gyro Bias	$1.0^\circ/\text{hr}$
Gyro Scale Factor	0.015%
Gyro Angle Random	$0.125^\circ/\sqrt{\text{hr}}$
Accelerometer Range	$\pm 50 \text{ g}$
Accelerometer Bias	1.0 mg
Accelerometer Scale	0.03%
Accelerometer Linearity	0.05%

5.6 Analysis of Results for Soft Formation Drilling Test

As described in the previous section, the first test simulated drilling through a soft formation with a relatively faster inclination build up rate. The raw sensor measurements were first denoised in order to increase the signal to noise ratio and reduce the uncertainty of the raw measurements. Position, velocity, and attitude information was extracted from the denoised measurements after they were processed through INS mechanizations and Kalman filtering and the results were analyzed.

5.6.1 Analysis of Raw Measurements

The MEMS inertial sensor measurements (especially gyroscope measurements) exhibit high noise and short term errors that can be challenging during relatively slow directional drilling applications. Figure 5.12 compares the accelerometer measurements before and after applying the denoising wavelet module. Similarly, gyroscope measurements are presented in Figure 5.13.

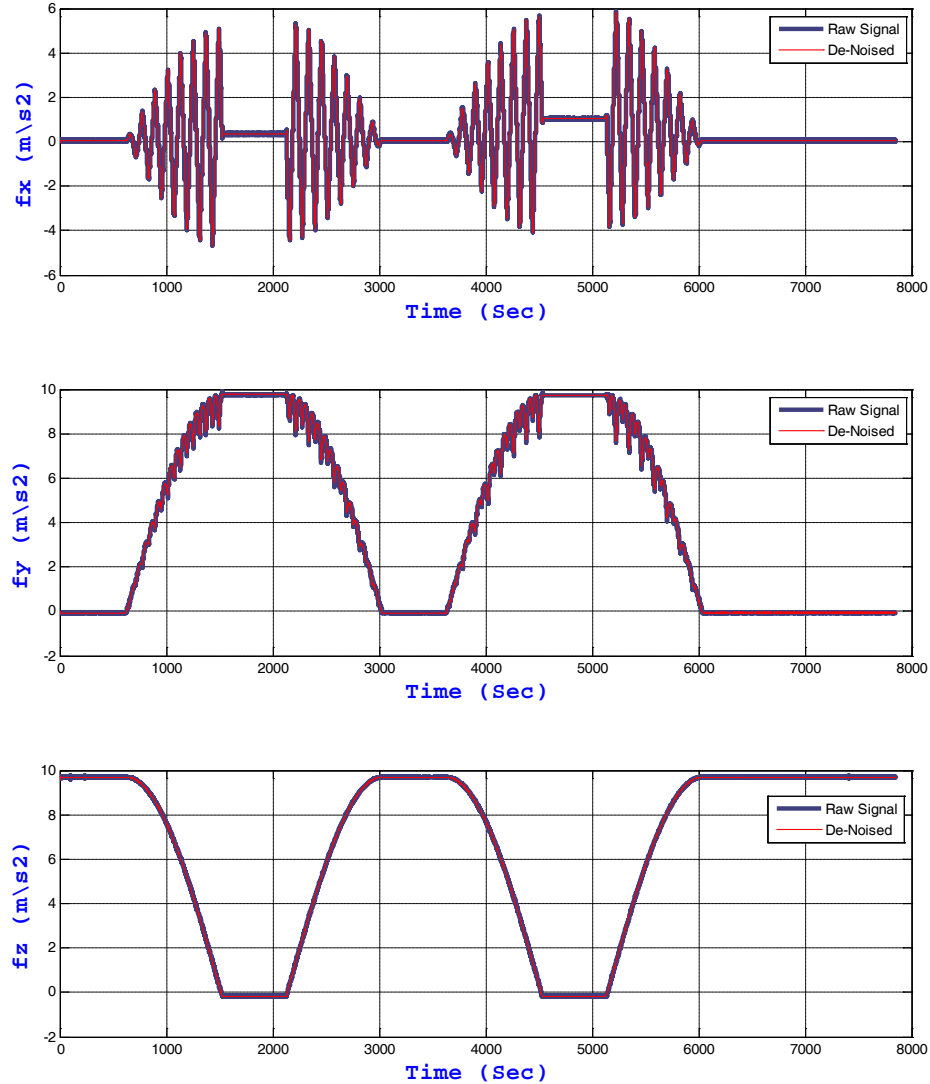


Figure 5.12 Accelerometer X (upper panel), Y (middle panel), and Z (lower panel) Measurements before and after Wavelet Denoising

The sensor output data rate was 200 Hz for accelerometers and gyroscopes. A Daubechies wavelet was applied with a soft threshold in order to denoise the sensor measurements. Four levels of decomposition were applied for the accelerometer measurements. The number of levels of decomposition is determined based on

removing the undesired high frequency components (noise) of the signal, while maintaining the useful signal information. Gyroscope measurements contain more undesired low frequency components than accelerometer measurements; thus gyroscope measurements need a higher level of decomposition. Six levels of decomposition were applied to gyroscope measurements to remove most of the long-term (low frequency) errors. The improvement of the sensor output signal after applying the wavelet module can be measured by computing the relative signal-to-noise ratio (SNR) using the following expression:

$$SNR = 10 \log \left(\frac{\sigma_{before}^2}{\sigma_{after}^2} \right). \quad 5.47$$

Improvements in the SNR for accelerometers and gyroscopes are summarized in Table 5.3.

Table 5.3: Improvements in SNR of Output Signals

fx	fy	fz	wx	wy	wz
56	34	16	37	37	28

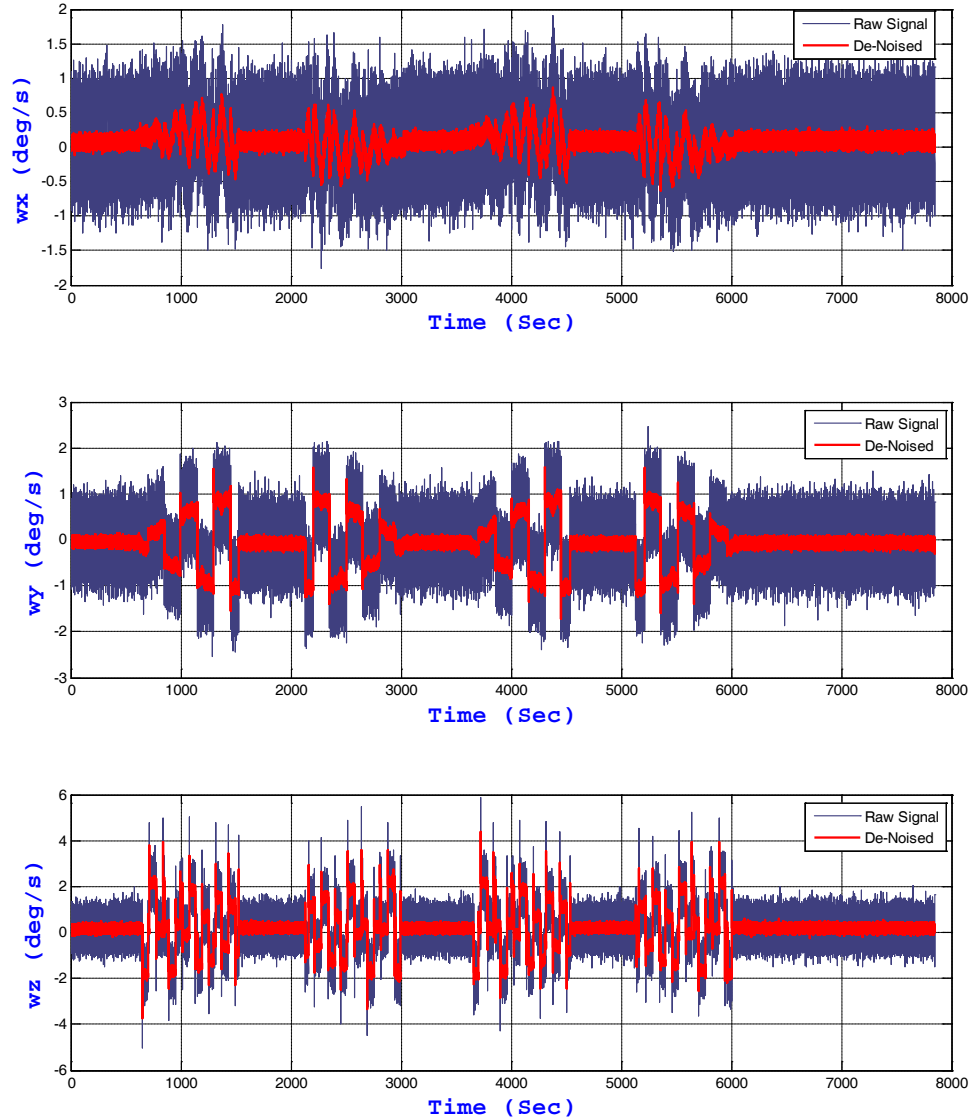


Figure 5.13: Gyroscope X (upper panel), Y (middle panel), and Z (lower panel) Measurements before and after Wavelet Denoising

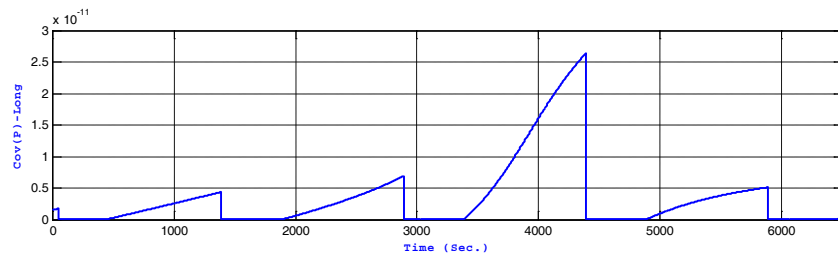
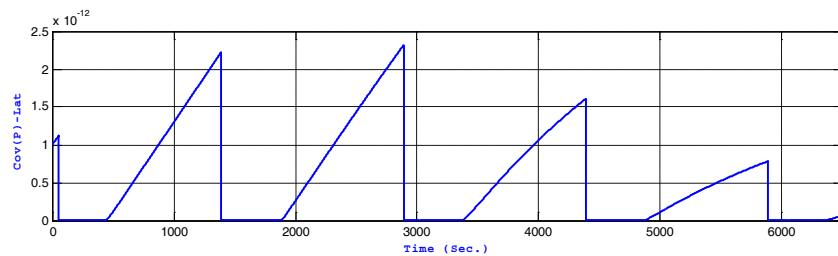
After denoising and reducing the uncertainty of the raw MEMS measurements, the position, velocity, and attitude of the drill bit is extracted. This is done by processing the denoised measurements through INS mechanization and the Kalman filtering

algorithm using MatLab® software. Analyses of the results are reported in the following subsections.

5.6.2 Estimation Errors—Covariance Analysis

5.6.2.1 Position errors

The error covariance matrix $P_k(+)$ of the estimate $\hat{\chi}_k(+)$ was derived using Equation 5.37. The diagonal elements of the error covariance matrix $P_k(+)$ are checked while drilling to determine MSEE convergence toward a minimum value or divergence. The MSEE of the drill bit position error states are presented in Figure 5.14 and Figure 5.15 for two different scenarios.



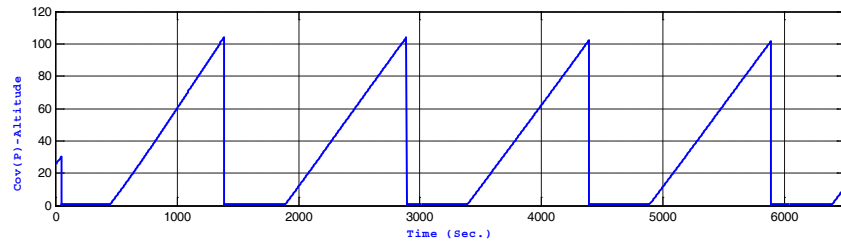


Figure 5.14: Covariance of Position Components during Drilling with a Continuous Drill Bit Rate of Penetration Updates and Stationary Updates

The first scenario differs from the second in that there are no continuous MCM position updates available during drilling. It can be noted from Figure 5.14 that the MSEE of three position error states diverged between the stationary stations where there was no external position measurements updates available to the Kalman filtering. Therefore, they became unobservable error states until the drilling operation stopped and stationary position updates were applied. When there were continuous MCM position updates available during drilling between the stationary periods, the MSEE of the position errors states converged to minimum values of $1.12 \times 10^{-14} \text{ rad}^2$ (0.045 m^2), $4.2 \times 10^{-14} \text{ rad}^2$ (1.70 m^2), and 0.06 m^2 for $\delta\varphi$, $\delta\lambda$, and δh , respectively as shown in Figure 5.15.

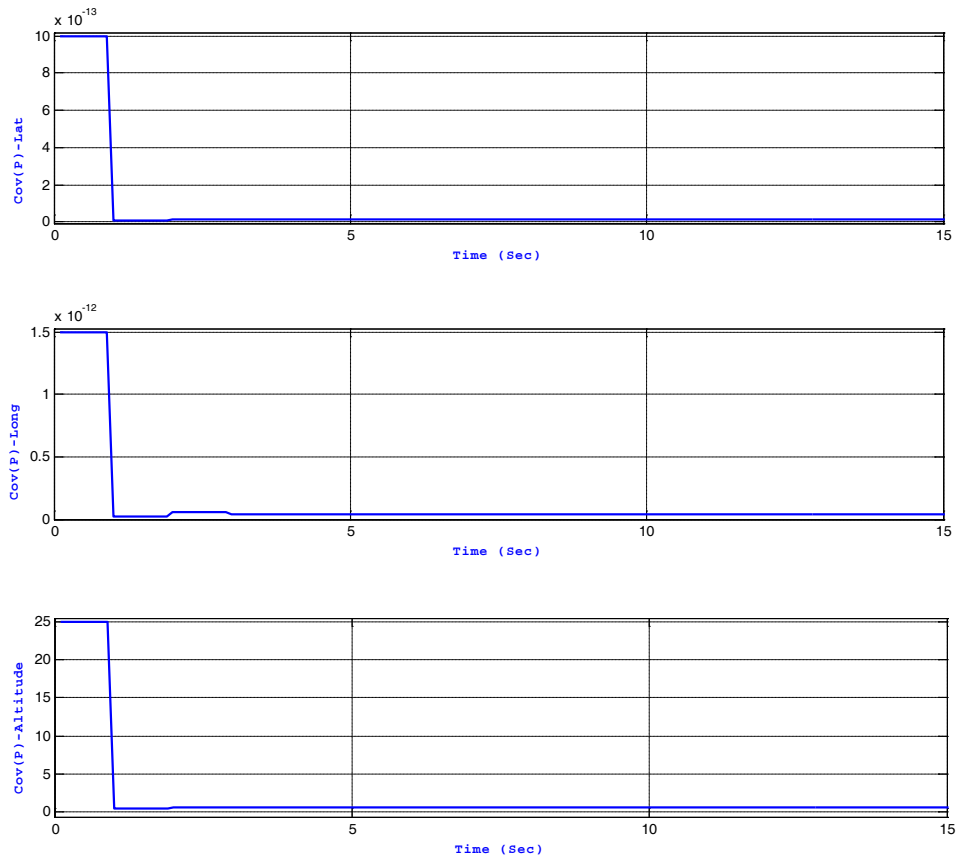


Figure 5.15: Covariance of Position Components during Drilling with Continuous MCM Position/Drill Bit Rate of Penetration Updates and Stationary Updates

5.6.2.2 Velocity errors

The MSEE of the velocity error states converged to minimum of 0.08 (m/s)^2 , 0.08 (m/s)^2 , and 0.1 (m/s)^2 for δV^e , δV^n , and δV^u , respectively. This fast convergence to the steady state values of the minimum MSEE was mainly due to the continuous updates of the drill bit rate of penetration. This makes the velocity error states strongly observable by the Kalman filter. The Kalman filter sustained minimum velocity error state estimations throughout the entire drilling process.

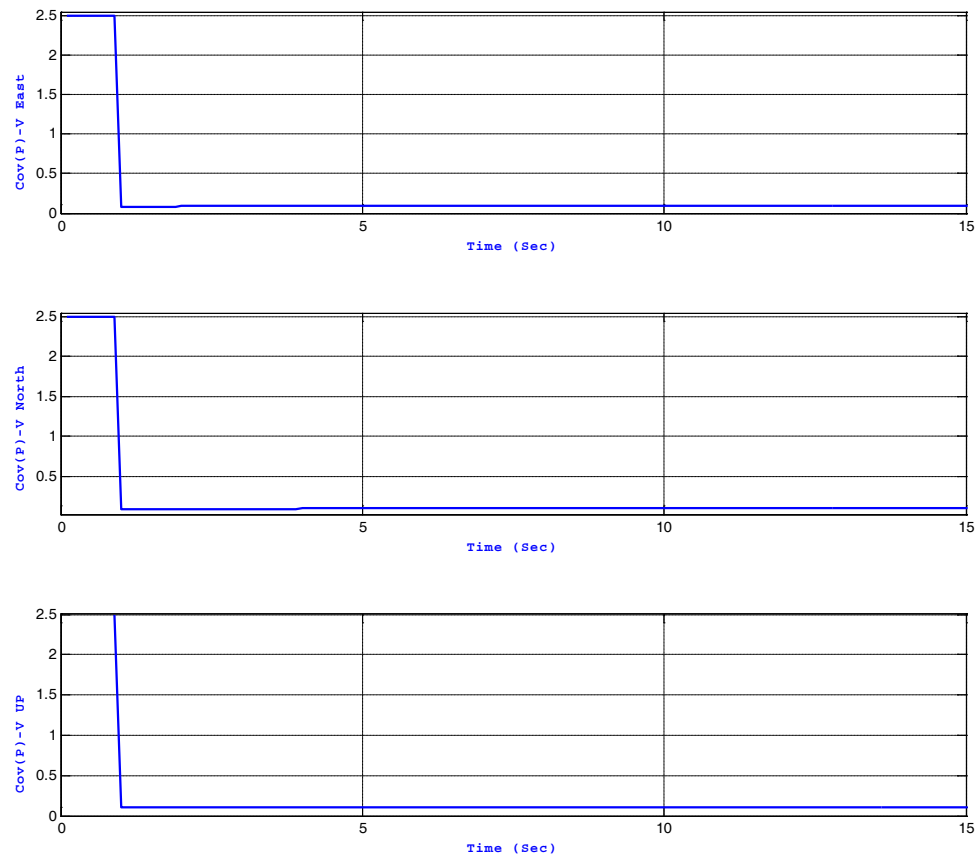


Figure 5.16: Covariance of Velocity Components during Drilling with Continuous MCM Position/Drill Bit Rate of Penetration Updates and Stationary Updates

5.6.2.3 Attitude errors

The MSEE of the inclination (pitch), toolface, and azimuth error states are presented in Figure 5.17. The toolface ϕ and pitch θ angles benefited from the continuous velocity updates, as both toolface $\delta\phi$ and pitch $\delta\theta$ error states converged to minimum MSEE values of $3.47 \times 10^{-5} \text{ rad}^2$ and $2.83 \times 10^{-5} \text{ rad}^2$, respectively. This is mainly due

to the strong coupling relationship between the east velocity error δV^e and the toolface angle error $\delta\phi$, and between the north velocity error δV^n and the pitch error $\delta\theta$; this is discussed in Appendix C.

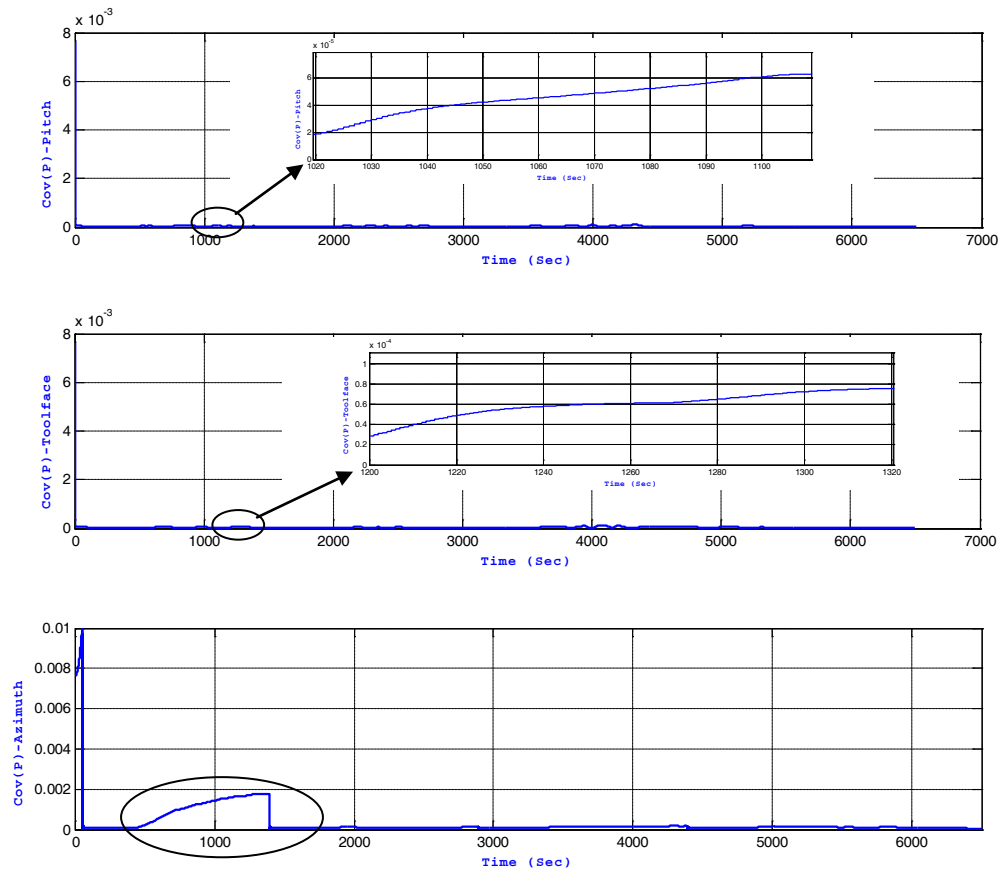


Figure 5.17: Covariance of Attitude Components during Drilling with Continuous MCM Position/Drill Bit Rate of Penetration Updates and Stationary Updates

Due to the slow penetration rate in the second test that implies small velocities along east and north directions, the pitch and roll angle errors may have become

unobservable states. As a result, the Kalman filter may not have sustained a steady state of a minimum MSEE all the time for pitch and roll errors; pitch and roll errors diverged as seen in the zoomed periods on the upper and middle panels of Figure 5.17. This motivated the derivation of synthetic pitch and toolface angles based on accelerometer measurements using Equations 5.26 and 5.27. Analyses of synthetic and Kalman filter derived angles are discussed in section 5.6.5.

The lower panel of Figure 5.17 presents the covariance of the drill string azimuth error state. It is noted that the azimuth error mostly diverged between stationary surveying stations. This is due to the weak coupling of the azimuth with velocity errors. The Kalman filter could not provide optimal estimates of azimuth errors until drilling stopped and stationary magnetometer heading updates became available. Details of the stationary heading updates are discussed in section 5.4.2.2.

5.6.2.4 Inertial sensor errors

Figure 5.18 presents the covariance of the three gyroscope and three accelerometer measurements that are applied as Kalman filter inputs during the drilling test. The gyroscope sensor error states converged to minimum MSEES of $6.55 \times 10^{-8} \text{ (deg/s)}^2$, $1.21 \times 10^{-7} \text{ (deg/s)}^2$, and $1.15 \times 10^{-7} \text{ (deg/s)}^2$ for $\delta\omega_x$, $\delta\omega_y$ and $\delta\omega_z$, respectively. Similarly, the accelerometer errors δf_x , δf_y , and δf_z converged to minimum MSEES of $2.14 \times 10^{-5} \text{ (m/s}^2\text{)}^2$, $2.35 \times 10^{-5} \text{ (m/s}^2\text{)}^2$, and $1.07 \times 10^{-5} \text{ (m/s}^2\text{)}^2$, respectively. The

covariance of the six sensor errors in Figure 5.18 validates the modelling of such errors as first order Gauss–Markov processes in Kalman filters.

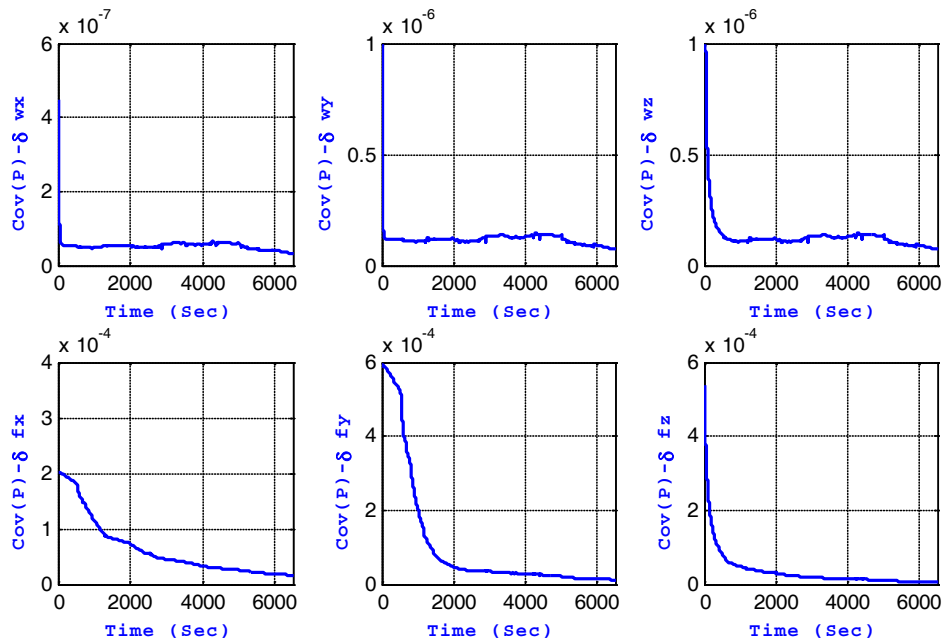


Figure 5.18: Covariance of Inertial Sensor Errors during Drilling with Continuous MCM Position/Drill Bit Rate of Penetration Updates and Stationary Updates

5.6.3 Position Results Analysis

North, east, and vertical positions, and position errors of the drill bit throughout the drilling test, are presented in the following subsections for two different scenarios. Additionally, a proposed solution is presented in order to limit the position error growth during periods of telemetry interruption.

5.6.3.1 Drilling with continuous updates and no telemetry interruption

During the first scenario, the inertial sensor measurements were processed through the Kalman filter with continuous uninterrupted updates of drill bit rate of penetration and MCM position. North, east and altitude positions derived by the Kalman filter during the drilling test were compared to the reference positions as shown in the upper panels of Figure 5.19, Figure 5.20, and Figure 5.21, respectively, while the lower panels of these figures present the observed position errors during the test. Maximum errors of 0.24 m, 0.72 m, and 0.36 m were observed over the entire drilling tests along the north, east, and altitude directions, respectively. The reference position was obtained from the tightly coupled INS/GPS integration solution provided by the SPAN unit. Although the utilized rotation table provides only rotation motions around its three axes, the rotation table top (where the sensors were mounted) exhibited a position displacement from the initial position.

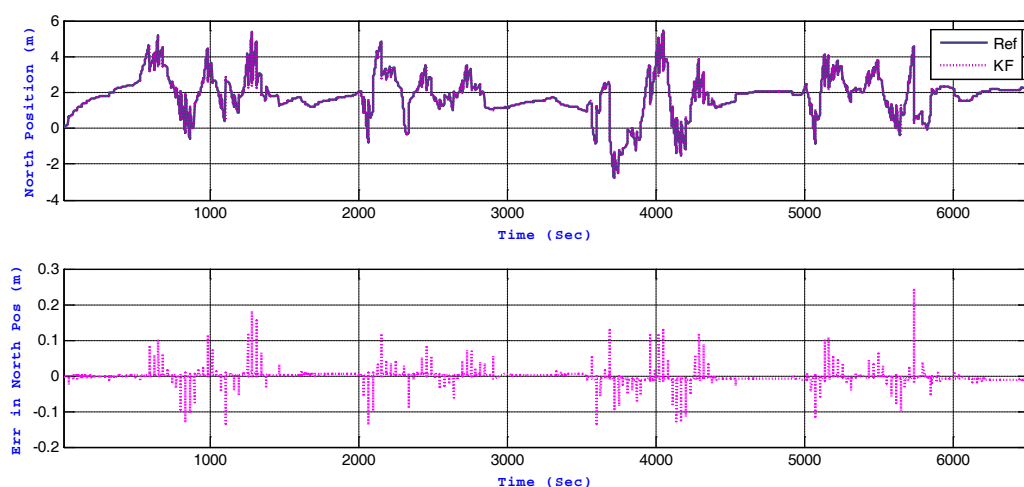


Figure 5.19: North Position Derived by KF Compared to a Reference Position (upper panel); Position Errors (lower panel) during Drilling

The relatively low values of the position errors are due to the continuous updates of the computed MCM position. Slow drilling along a predetermined well path had the advantage of providing good external position updates that limit the growth of position error components during drilling and provided RMS values of north, east, and altitude position errors of 0.012 m, 0.05 m, and 0.14 m, respectively.

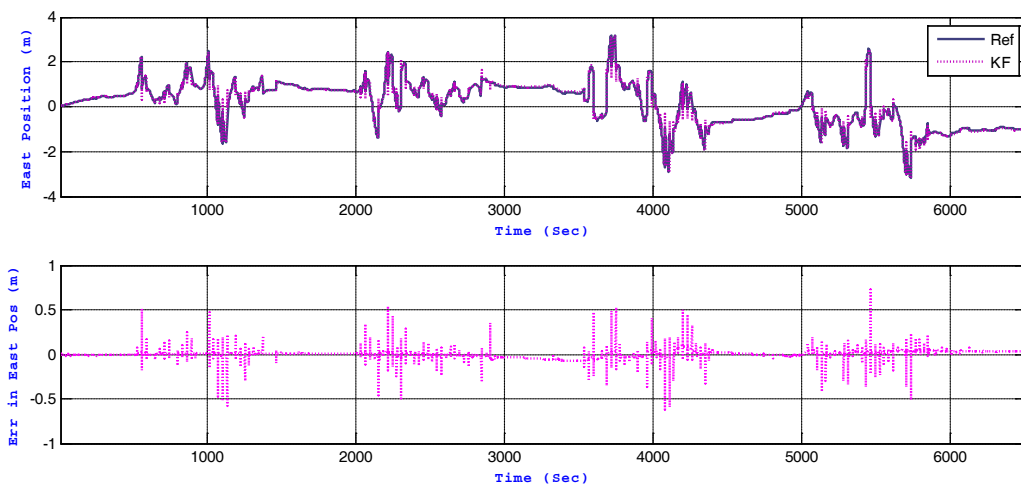


Figure 5.20: East Position Derived by KF Compared to a Reference Position (upper panel), Position Errors (lower panel) during Drilling

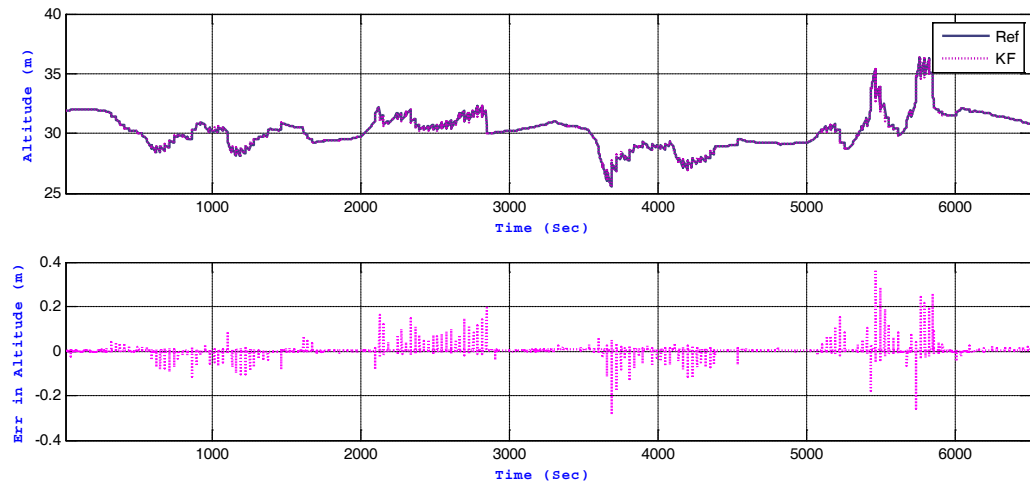


Figure 5.21: Altitude Derived by KF Compared to a Reference Altitude (upper panel), Position Errors (lower panel) during Drilling

5.6.3.2 Drilling with continuous updates during telemetry interruption periods

The second scenario is similar to the previous one, but it contains some periods of interruption of the continuous updates. These periods of interruptions can exist in actual drilling processes due to telemetry problems between the downhole equipment and the surface control station, These interruptions prevent the INS from being continuously updated with external measurements by the Kalman filter. Twelve telemetry interruption periods were introduced during drilling for a period of 60 seconds each. The observed position error in north (upper panel), east (middle panel), and altitude (lower panel) directions are presented in Figure 5.22.

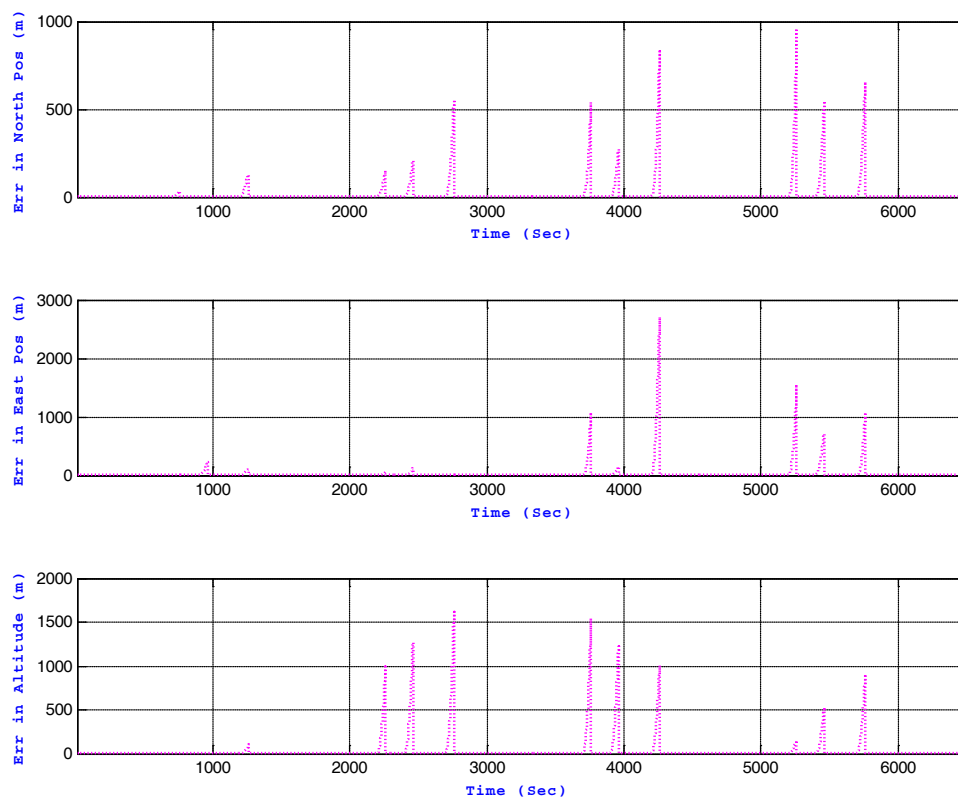


Figure 5.22: Position Errors in North (upper panel), East (middle panel), and Altitude (lower panel) Directions

Maximum observed errors in north, east, and altitude positions were 922 m, 2625 m, and 1566 m, respectively. The three position components of error begin to grow if there is a telemetry interruption of the continuous drill bit rate of penetration and MCM position updates; these errors continue to grow until continuous updates become available again. Although part of the sensor bias error was removed by the first order GM model in the Kalman filter, residual errors caused the position error to drift with time. The following subsection addresses this problem.

5.6.3.3 Limiting position error growth during telemetry interruption

A slow drill bit rate of penetration limits position error growth at periods of telemetry interruption. To further reduce position error growth, zero integrated velocity and position error drift at periods of telemetry interruptions is proposed. In this technique, the velocity and position of the drill bit along the entire interruption period are fixed at the last velocity and position reading before the interruption. This significantly improved the north, east, and altitude position errors during periods of telemetry interruption as shown in Figure 5.23, Figure 5.24, and Figure 5.25, respectively. The position errors were limited to maximums of 3.18 m (RMS of 0.34 m) for the north direction, 3.405 m (RMS of 0.28 m) for the east direction, and 4.1273 m (RMS of 0.33 m) for the altitude direction.

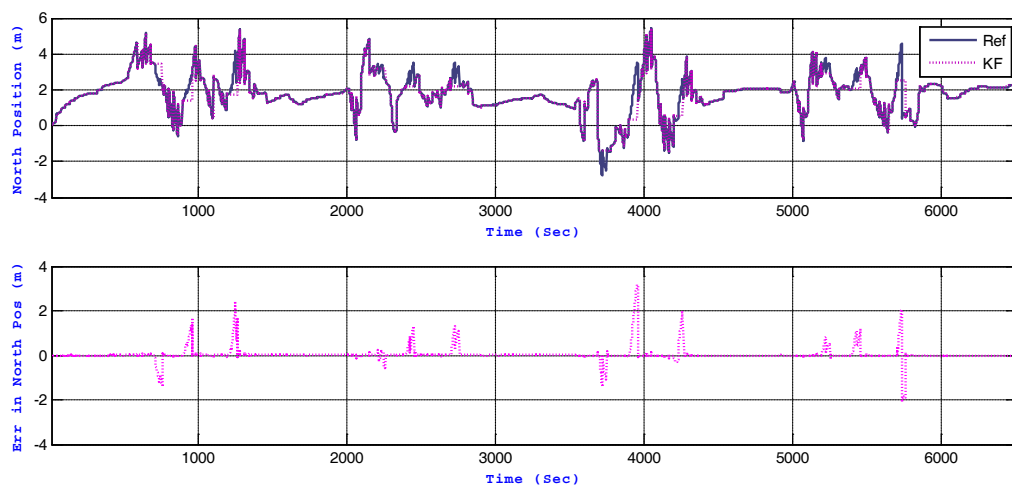


Figure 5.23: Position in North Direction Compared to a Reference Position (upper panel); Position Errors (lower panel)

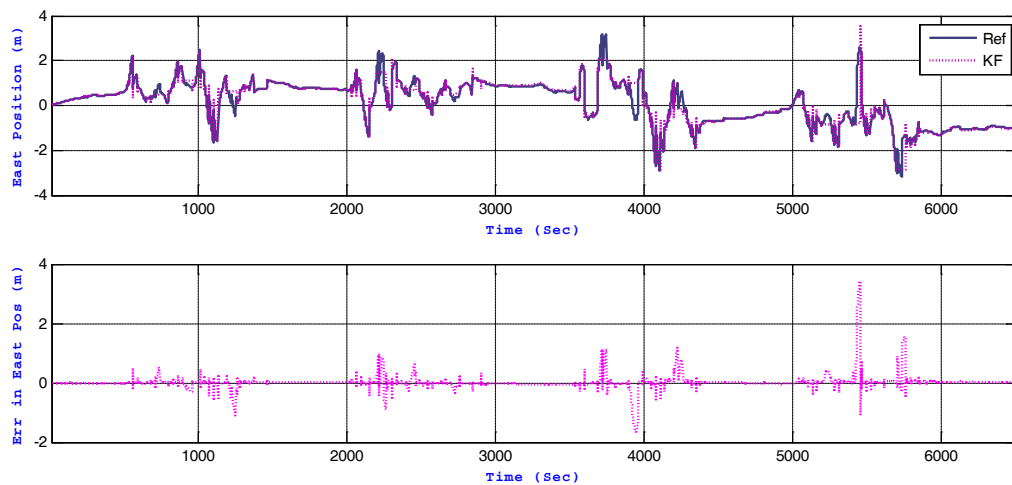


Figure 5.24: Position in East Direction Compared to a Reference Position (upper panel); Position Errors (lower panel)

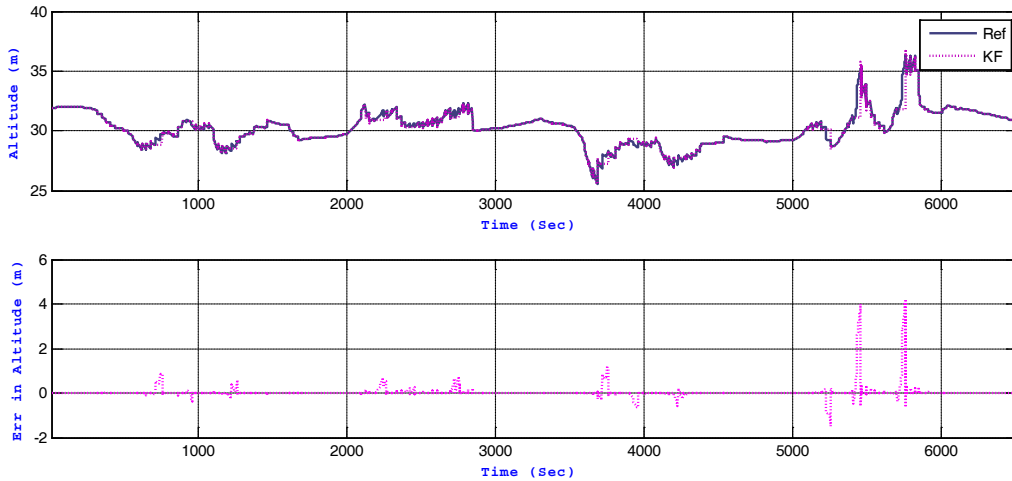


Figure 5.25: Altitude Position Compared to a Reference Altitude (upper panel); Position Errors (lower panel)

5.6.4 Velocity Results

5.6.4.1 Drilling with continuous updates and no telemetry interruption

The continuous drill bit rate of penetration was available for the entire test as long as there were no telemetry interruptions. The observed velocity component errors are shown in Figure 5.26 for east (upper panel), north (middle panel), and up (lower panel) velocity directions, respectively. The observed RMS values of velocity errors were 0.069 m/s along the east direction, 0.057 m/s along the north direction, and 7.84×10^{-4} m/s along the vertical direction.

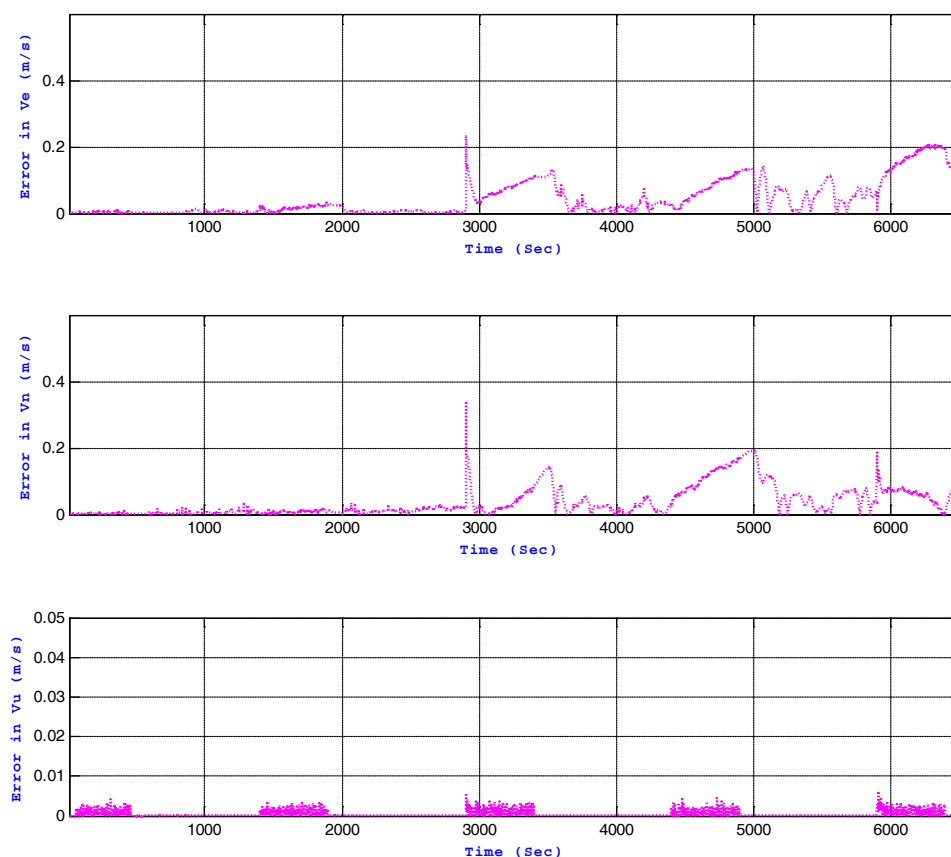


Figure 5.26: Velocity Error in East (upper panel), North (middle panel), and Up (lower panel) Directions

The available continuous updates of the drill bit rate of penetrations cause the velocity error states to be strongly observable by the Kalman filter, thus the velocity errors were optimally estimated. Velocity errors in east and north directions exhibited similar performance during the entire drilling test. The velocity errors during the second half of the test were relatively higher than the first half. This is expected to improve with further tuning of the covariance matrix of the measurement update R . The up velocity exhibited a consistent accuracy due to the consistent update measurements.

5.6.4.2 Drilling with continuous updates during telemetry interruption periods

Telemetry interruption were introduced during the test as in section 5.6.3.2. The drill bit rate of penetration was not available during these periods as an external update to the Kalman filter. The observed velocity errors in east (upper panel), north (middle panel), and altitude (lower panel) directions are presented in Figure 5.27 during these interruptions periods. Maximum velocity errors of 53 m/s (east direction), 66 m/s (north direction), and 53 m/s (up direction) were observed. The high unlimited growth of the velocity errors during the interruption periods is clearly seen in Figure 5.27. It was concluded that this effect was due to the high drift of the low cost inertial sensors.

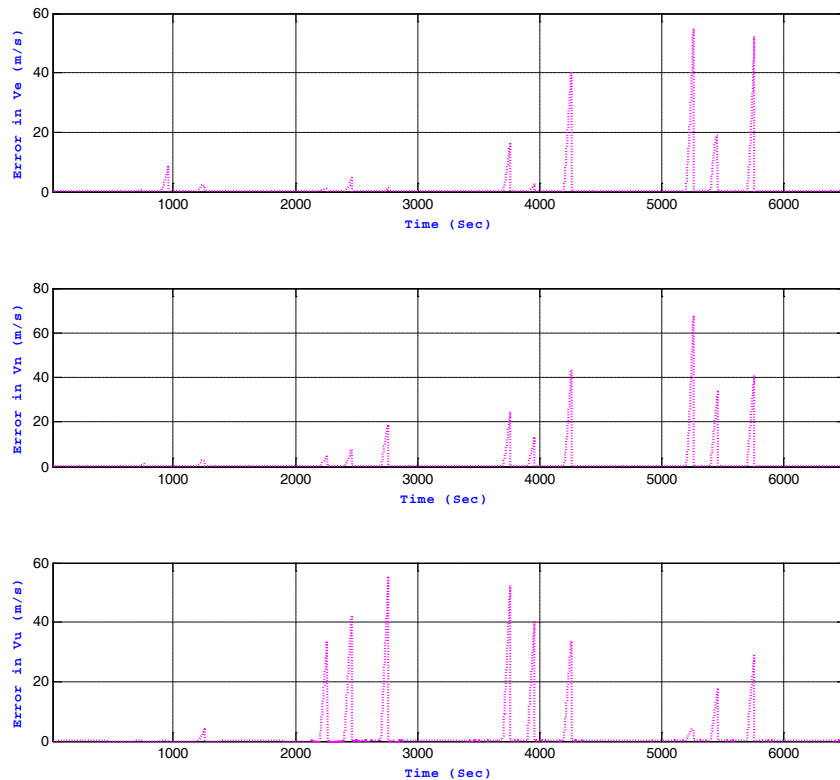


Figure 5.27: Velocity Error in East (upper panel), North (middle panel), and Up (lower panel) Directions

5.6.4.3 Limiting velocity error growth during telemetry interruption

Velocity errors can be reduced significantly by keeping fixed velocity updates during periods of telemetry interruptions. By applying the zero integrated velocity error drift technique for velocity errors in east (upper panel), north (middle panel), and up (lower panel) directions, the maximum velocity errors were reduced to 0.19 m/s, 0.18 m/s, and 0.04 m/s, respectively, as shown in Figure 5.28. This led to significant performance improvement and enhanced positioning accuracy.

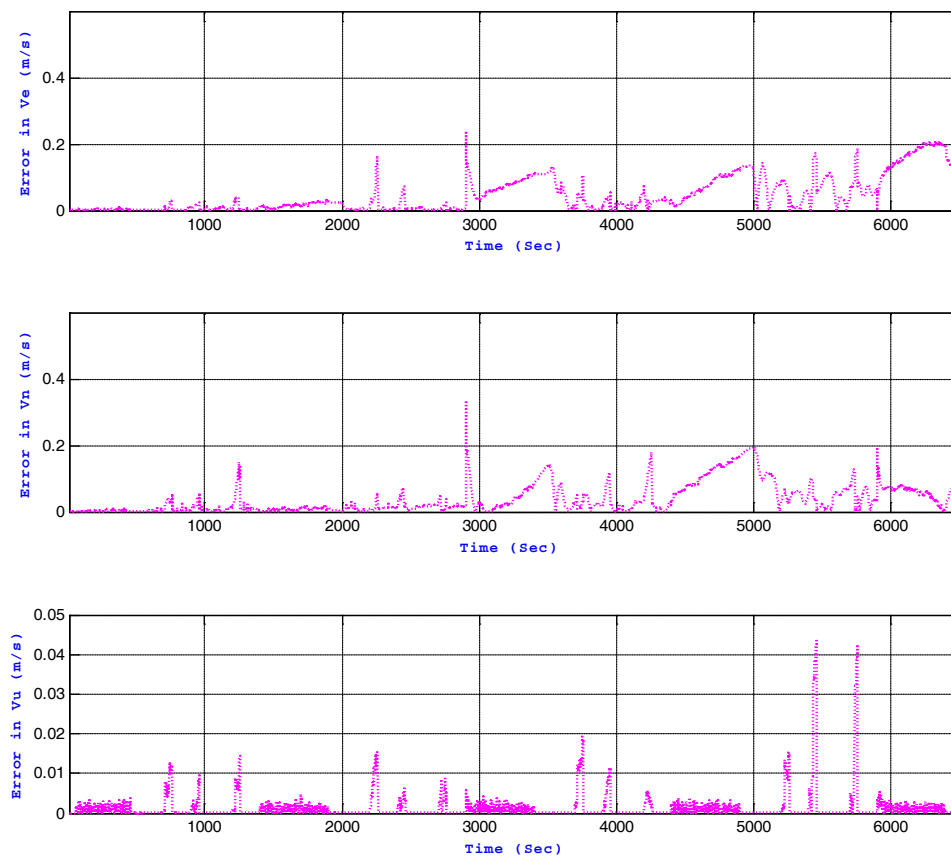


Figure 5.28: Velocity Errors in East (upper panel), North (middle panel), and Up (lower panel) Directions

5.6.5 Attitudes Results

5.6.5.1 Drill bit inclination and toolface results analysis

The reference 3-axis rotation table of the inclination angle is presented in the upper panel of Figure 5.29 and compared to the KF inclination angle during the entire drilling test. The lower panel of Figure 5.29 depicts the observed error of the KF inclination angle. Similarly, the KF output toolface angle is compared to the reference drill bit toolface angle as shown in the upper panel of Figure 5.30; the observed error

of the KF toolface angle is shown in the lower panel of Figure 5.30. Although there is a continuous velocity update available from the drill bit rate of penetration, which should influence inclination and toolface angle accuracies, the slow penetration rates limited the effects of velocity updates on the attitude errors. Consequently, the inclination and toolface angle accuracies deteriorate in the long term (see Figure 5.29 and Figure 5.30). We also noticed that such effects were stronger when the drill bit was in vertical or near vertical sections of the well (small inclination angles). Over the entire test period, the inclination angle error RMS value was 14° while the toolface angle error had a RMS value of 21° . Such accuracy levels are not acceptable and other methods should be considered for the computation of both inclination and toolface angles.

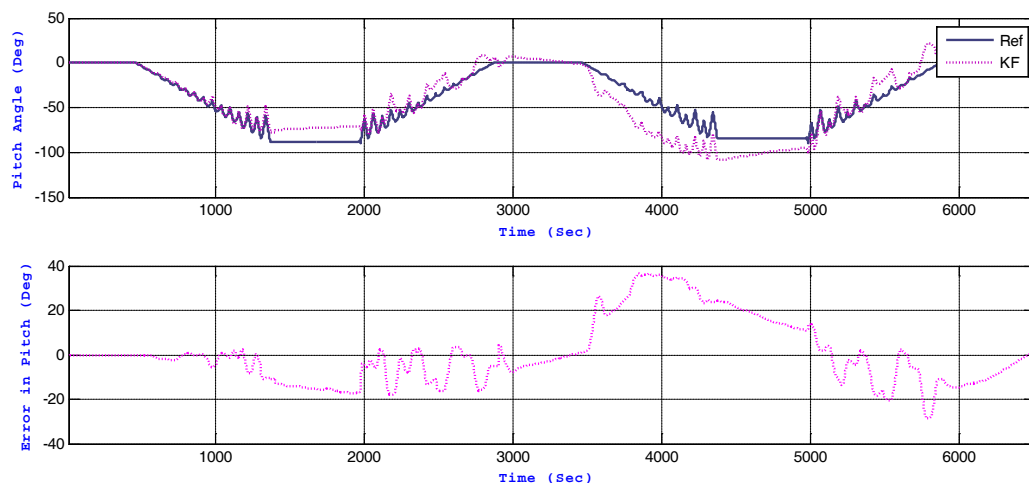


Figure 5.29: KF Pitch Angle Compared to Reference Angle (upper panel); Error in the Pitch Angle (lower panel).

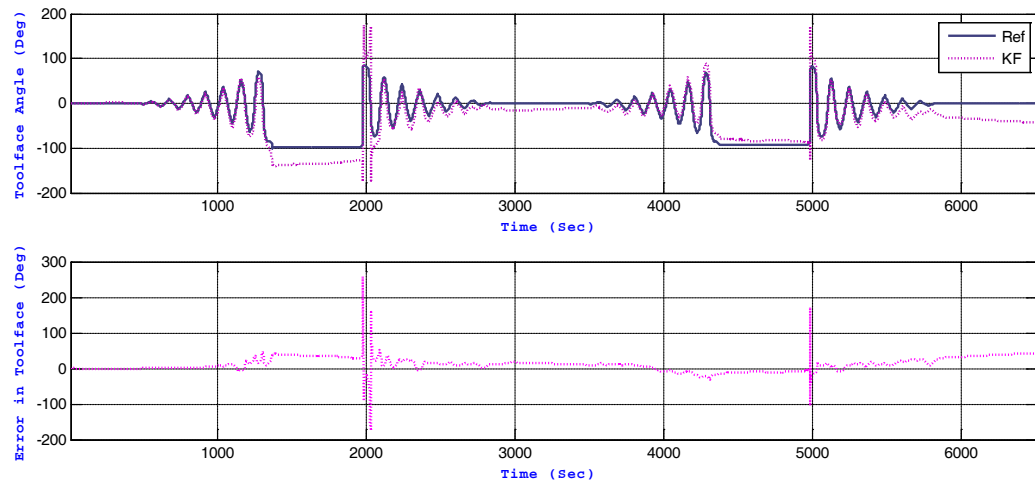


Figure 5.30: KF Toolface Angle Compared to Reference Drill bit Toolface Angle (upper panel); Error in Toolface Angle (lower panel).

5.6.5.2 Synthetic drill bit inclination angle and toolface angle

Synthetic inclination and toolface angles are proposed in order to overcome the deterioration in accuracies of the KF drill bit inclination and toolface angles in vertical or near vertical sections of the well. The synthetic angles are based entirely on accelerometer measurements and are derived using Equations 5.26 and 5.27. They are only valid at slow speed applications such as the one discussed in this dissertation. Synthetic pitch angles compared to the 3-axes table reference pitch angle and the KF derived angle are presented in the upper panel of Figure 5.31, while the lower panel of this figure presents the synthetic pitch angle error that did not exceed a RMS value of 0.19° . Figure 5.32 presents similar plots for the toolface angles with an observed RMS value of 0.69° . Figures 5.31 and 5.32 show that significant accuracy improvement of

inclination and toolface angles was achieved by utilizing the synthetic angles technique.

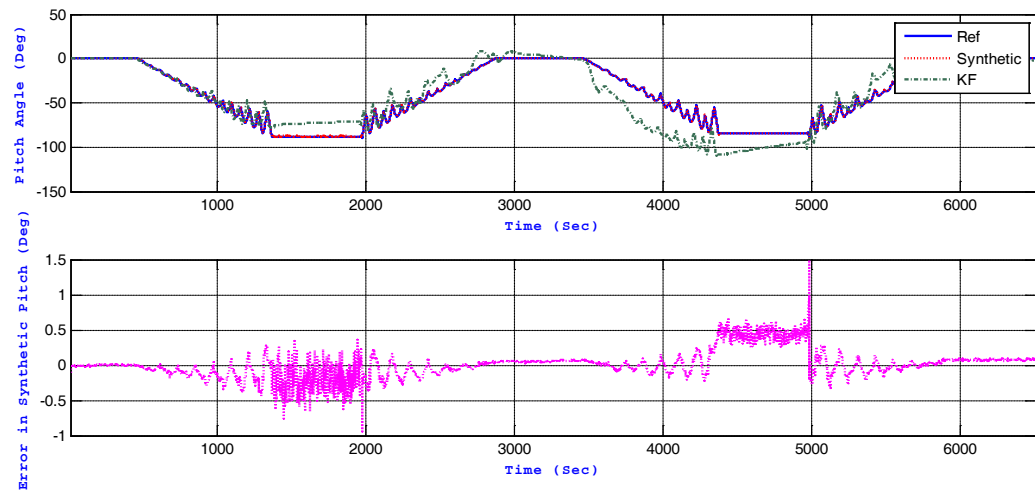


Figure 5.31: Synthetic Pitch Angle Compared to Reference and KF Derived Pitch Angles (upper panel); Error in Synthetic Pitch Angle (lower panel).

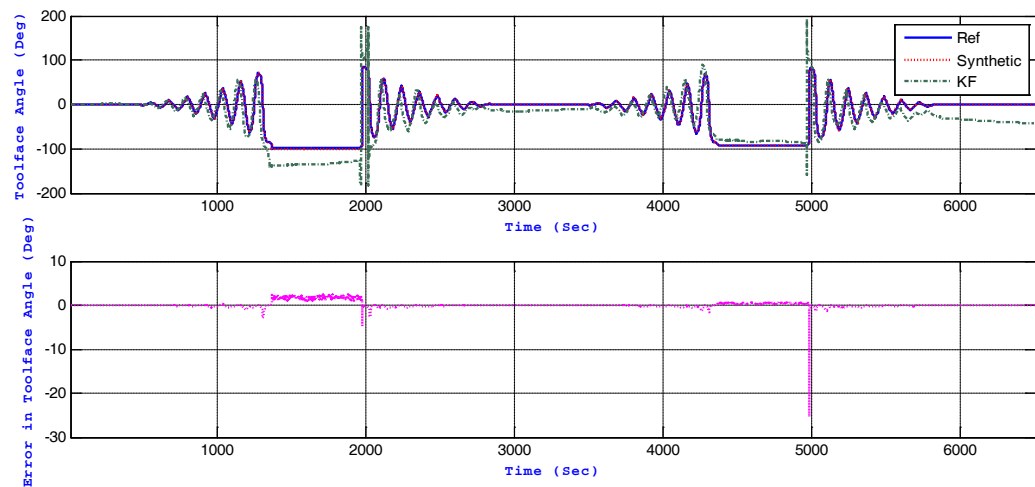
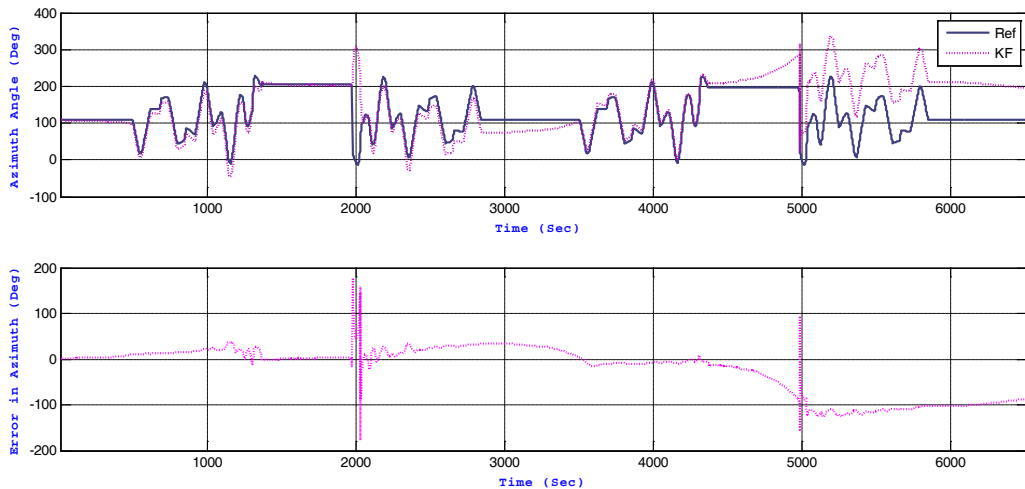


Figure 5.32: Synthetic Toolface Angle Compared to Reference and KF Derived Toolface Angles (upper panel); Error in Synthetic Toolface Angle (lower panel).

5.6.5.3 Analysis of azimuth angle results

Values for KF azimuth angles during the soft formation drilling test are presented in Figure 5.33 and compared to the reference azimuth angle in the upper panel; azimuth angle errors are shown in the lower panel. Continuous updates for the drill bit rate of penetration and the MCM position were applied to the Kalman filter. The observed RMS value of the azimuth errors was 55° with a maximum error of 126° . It is believed that the main source of this large azimuth error was the relatively large scale factor of MEMS gyroscope errors. In the experiment conducted here, significant rotations around the tool spin axes were simulated. Such large values of rotation rates modulated the scale factor errors of the MEMS gyroscopes and led to large azimuth errors. The azimuth accuracy can be improved by applying external stationary heading updates as explained in the following section.



**Figure 5.33: KF Azimuth Angle Compared to a Reference Angle (upper panel);
Errors in Azimuth Angle (lower panel)**

The sharp spikes around 2000 and 5000 seconds noted in Figure 5.33 occur in the transition periods from stationary to drill-ahead modes. Improper denoising in these transition periods may be the reason for this undesirable behaviour.

5.6.5.4 Stationary azimuth angle updates

When the drill string is stopped to add new pipe stands, heading stationary information can be obtained from installed magnetometers inside the drilling probe. The measured magnetic azimuth is converted to the true azimuth and applied as heading updates during stationary periods. In Figure 5.34, the KF azimuth with applied stationary heading updates is compared to the reference azimuth (upper panel); the azimuth error is presented in the lower panel of Figure 5.34. It can be seen in the figure that the azimuth error increases between the heading update stations prior to resetting at the commencement of each update station. The observed azimuth error during the first drilling period reached a maximum of 36° , then decreased to 0.06° due to the stationary heading update. The maximum azimuth error during the second drilling trip was 35° before it was reduced to 0.052° when stationary heading updates were applied; similar behaviour is true for the rest of the test. Over the entire drilling test, the observed azimuth RMS value was 15° .

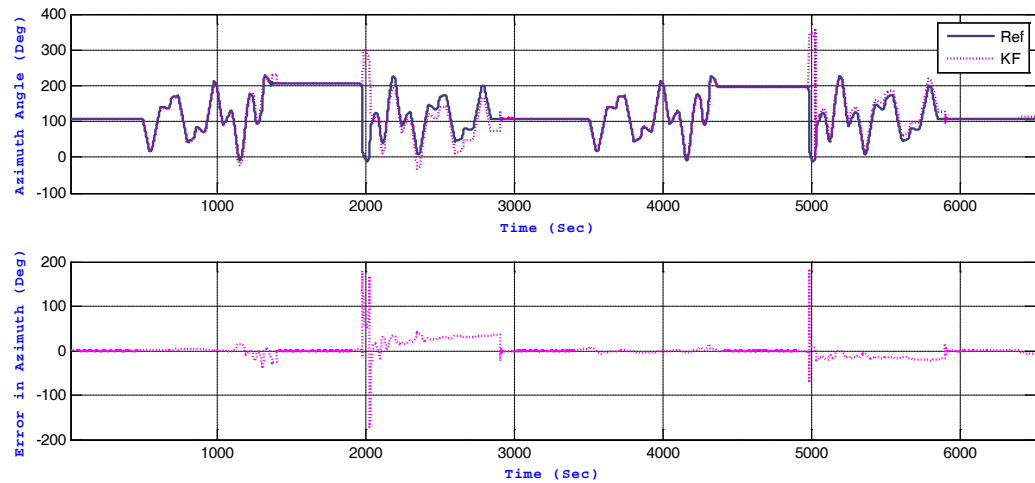


**Figure 5.34: KF Azimuth Angle Compared to a Reference Angle (upper panel);
Errors in the Azimuth Angle (lower panel)**

5.7 Analysis of Test Results from Hard Formation Drilling

Drilling in a hard formation is slower than drilling in a soft formation. Thus, the hard formation test was conducted with a slower drilling inclination build-up rate, where the rotation rate of the middle axis was set to 0.01 °/s. This translates to a change of inclination from 0° to 90° over a period of 9000 s (2.5 h). This test included two trips for a period of 5 hours with a 10 minute stationary period in between trips in order to connect a new drill pipe stand. The outer and inner axes were changed in a manner similar manner to the first test throughout the entire trip. Rotation rates of the middle, outer, and inner axes are presented in Figure 5.11.

Procedures in the hard formation test were similar to those of the soft formation test. Position, velocity, and attitude of the drill bit were similar in both tests. This confirms

the consistency of the developed drilling navigation algorithm. Position, velocity, and attitude measurements for the hard formation test are presented in the following subsections.

Continuous updates of the MCM position and the continuous drill bit rate of penetration were applied while drilling except at periods of telemetry interruptions. Sixteen interruptions of 60 seconds each were introduced during this drilling test. A zero integrated velocity and position error drift at periods of telemetry interruptions was applied, where the velocity and position of the drill bit along the entire interruption period were fixed as the last velocity and position reading before the interruption. A summary of position, velocity, and attitude results of the hard formation test is provided in the following sections.

5.7.1 Position Results

Kalman filter output positions are compared to the reference position during the entire test and results are presented in the upper panels of Figure 5.35, Figure 5.36, and Figure 5.37 for north, east, and vertical directions, respectively; position errors are depicted in the lower panel of each figure.

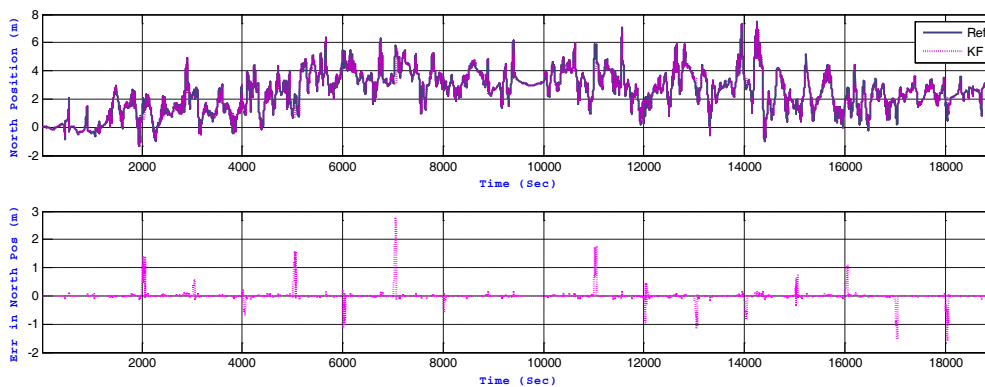


Figure 5.35: Position in North Direction Compared to the Reference North
Position (upper panel); Error in North Position (lower panel)

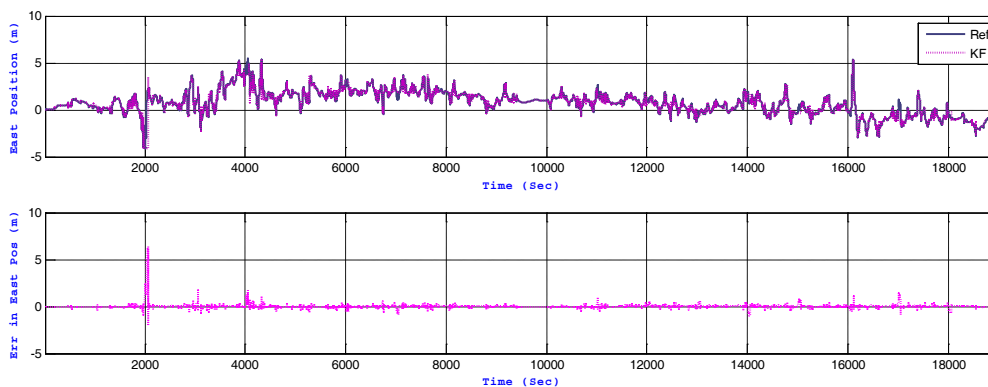


Figure 5.36: East Position Compared to the Reference East Position (upper
panel); Error in East Position (lower panel)

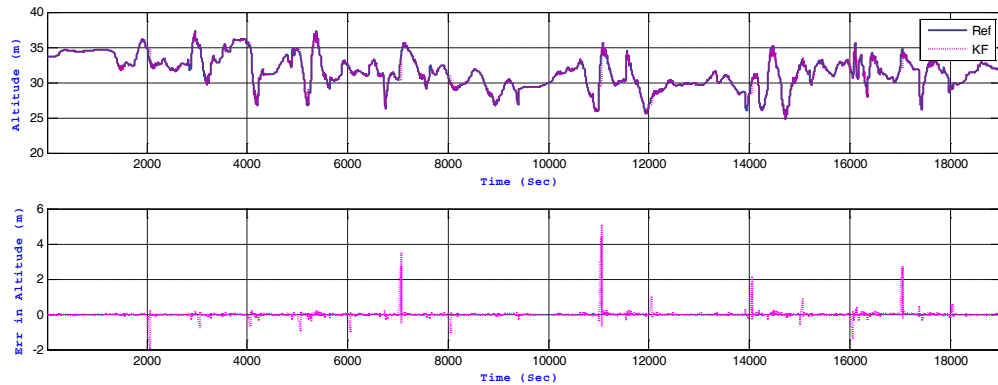


Figure 5.37: Altitude Compared to the Reference Altitude (upper panel); Error in Altitude (lower panel)

The maximum observed position errors during telemetry interruption periods was 2.73 m, 6.32 m, and 5.02 m for north, east, and vertical directions, respectively. RMS position errors over the entire drilling process were 0.18 m, 0.29 m, and 0.26 m along the north, east, and vertical directions, respectively.

5.7.2 Velocity Results

Observed velocity errors along the east (upper panel), north (middle panel), and up (lower panel) directions are presented in Figure 5.38. Periods of telemetry interruption that resulted in interruption of the drill bit rate of penetration information are marked by a growth in the velocity error which decreased when continuous velocity updates became available again. The observed maximum velocity errors at telemetry interruption periods along east, north, and up directions were 0.22 m/s, 0.1 m/s, and 0.05 m/s, respectively.

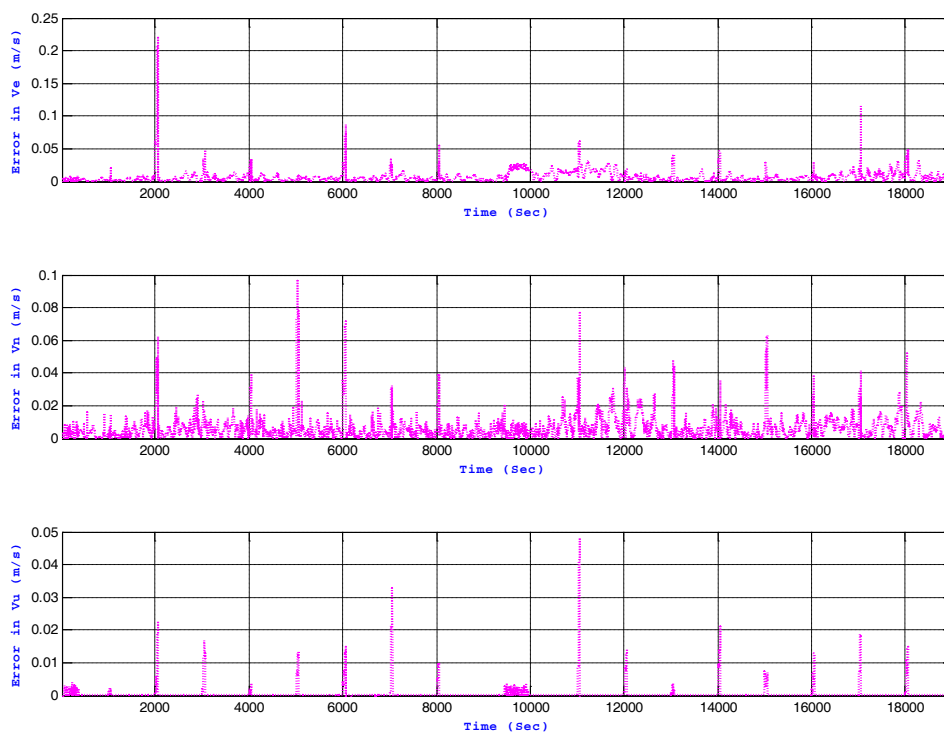


Figure 5.38: Velocity Error in East (upper panel), North (middle panel) and Up (lower panel) Directions

5.7.3 Attitude Results

Synthetic inclination and toolface angles were used to overcome accuracy deterioration of the KF drill bit inclination and toolface angles in vertical or near vertical directions. The advantages of this method are discussed in section 5.6.5.2. Synthetic pitch angles used during this test were compared to reference and KF derived angles in the upper panel of Figure 5.39. The lower panel of Figure 5.39 depicts the error in the pitch angle—a RMS pitch error of 0.11° was observed. Synthetic toolface angles are presented in the upper panel of Figure 5.40 where they are compared to reference and KF toolface angles; the observed synthetic toolface

errors are shown in the lower panel of Figure 5.40. The observed RMS toolface error was 0.30° during the entire drilling period.

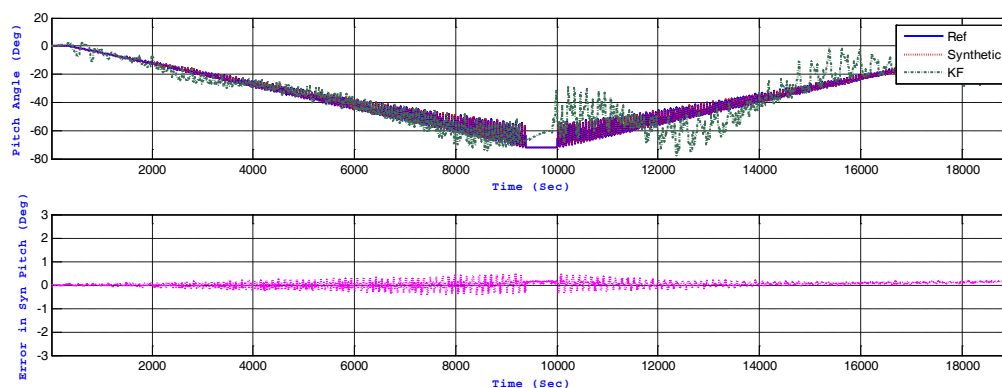


Figure 5.39: Synthetic Pitch Angle Compared to Reference and KF Driven Pitch Angles (upper panel); Error in Synthetic Pitch Angle (lower panel).

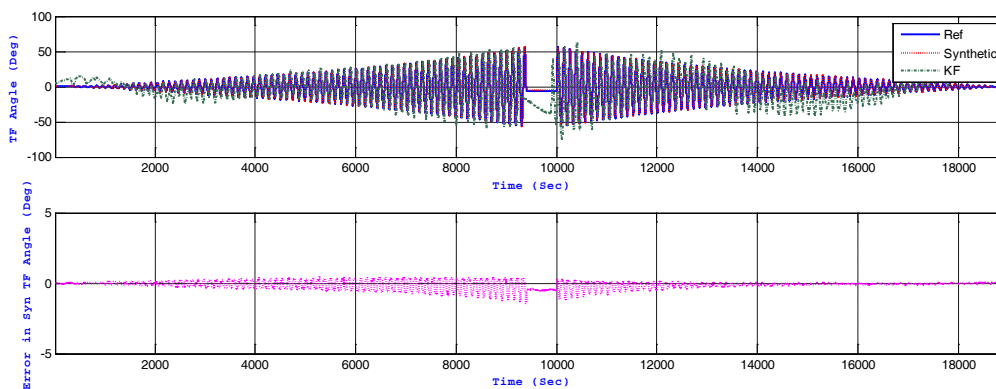
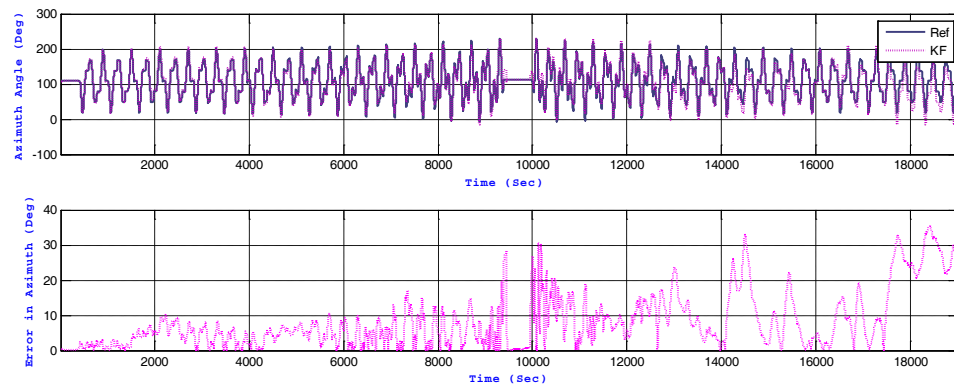


Figure 5.40: Synthetic Toolface Angle Compared to Reference and KF Driven Toolface Angles (upper panel); Error in Synthetic Toolface Angle (lower panel)

The KF azimuth is compared to the reference azimuth and presented in the upper panel of Figure 5.41, while azimuth error is presented in the lower panel. Stationary

heading updates were applied when drilling was stopped to add a new pipe stand. Drilling was stopped for 10 minutes after the first trip at time 9400 sec. Continuous MCM position and drill bit rate of penetration updates were available and utilized in the Kalman filter. The observed RMS azimuth error was 11° during drilling. The observed azimuth error during the first drilling period reached a maximum 28° then decreased to 0.6° due to the stationary heading update. The maximum azimuth error during the second drilling trip was 35.5° .



**Figure 5.41: KF Azimuth Compared to a Reference Azimuth (upper panel);
Error in Azimuth (lower panel)**

5.8 Conclusions

The Kalman filter continuous surveying system was applied to two drilling simulation tests with inclination build up rates of $0.1\text{ }^\circ/\text{s}$ and $0.01\text{ }^\circ/\text{s}$ for drilling in soft and hard formations, respectively. Continuous external updates of the MCM position and the drill bit rate of penetration were utilized to reduce measurement error drift. When the drilling process was stopped to connect new drill pipe stands, stationary updates of the

MCM position, ZUPT, and heading were employed by the Kalman filter. The zero integrated velocity and position error drift technique was applied to telemetry interruption periods, where it significantly reduced the velocity and the position errors. Synthetic inclination and toolface angles based entirely on accelerometer measurements were introduced while drilling. They improved the accuracy of attitude angles when compared to the accuracy provided by the Kalman filter.

CHAPTER SIX:

CONCLUSIONS

AND THESIS CONTRIBUTIONS

6.1 Summary

This thesis investigated the potential of low cost MEMS inertial sensors as a borehole surveying system for oil and gas directional drilling applications. Such a system can be miniaturized on the electronic chassis inside an MWD tool or inside an RSS electronic section. This thesis validated and qualified the MEMS INS for drilling applications where the hostile drilling environment is a limiting factor to most commercially available inertial navigation systems. Furthermore, this thesis utilized wavelet multi-resolution analysis to denoise MEMS inertial sensor signals and to mitigate the effects of the shock and vibration while drilling. A technique to detect shock level and severity while drilling based on MEMS measurements and wavelet packet analysis was introduced and discussed in this thesis.

A method utilizing a complete MEMS-based INS was employed to continuously survey a well trajectory while drilling. After denoising by a wavelet signal processing module, the MEMS sensor measurements were processed through Kalman filtering

and unique external aiding measurements while drilling. The performance of the surveying technique was enhanced during periods of telemetry interruptions of continuous update measurements. This was achieved by employing the proposed zero integrated velocity and position error drift. Finally, the inclination and toolface accuracies of the drill bit were improved by using synthetic inclination and toolface angles based entirely on accelerometer measurements.

6.2 Conclusions and Thesis Contributions

The following are the highlights of the thesis contributions:

- **MEMS Inertial Sensors Qualification for Harsh Drilling Environments**

Shock and vibration are the main challenges for electronic components and sensors used downhole while drilling. The selection of sensors for the drilling industry is very limited as sensors must withstand hostile drilling condition. This thesis qualified an inertial MEMS-based unit for drilling applications according to drilling industry standards. Qualification testing was conducted at a testing facility located in Houston, Texas. MEMS inertial sensors were subjected to shock forces of 1400 g for a period of 4 hours and a vibration level of 14 g at random frequencies ranging from 5 Hz to 400 Hz. The mechanical and electrical integrity and proper functioning of the MEMS inertial sensors were verified during both shock and vibration testing,.

- **Performance Enhancement of MEMS Inertial Sensors under Severe Shock and Vibration**

MEMS inertial sensor performance was enhanced by reducing the induced short term error due to shock and vibration while drilling. Wavelet multi-resolution analysis was implemented to separate shock and vibration from the motion dynamic components and wavelet packet analysis was employed to analyze shock and vibration effects. Sensor output signals were decomposed into 6 levels, while the reconstructed signal included only the approximation signal at the 6th decomposition level. MEMS output signal uncertainty was considerably reduced with an average improvement of 87% for accelerometer measurements and 67% for gyroscope measurements.

- **Detection Technique of Shock and Vibration Levels while Drilling**

Shock and vibration while drilling significantly reduce drilling speed and thus increase drilling cost. Shock and vibration are the main causes of drilling tool failure and can cause the BHA to twist off and be lost downhole. This thesis suggests a method based entirely on MEMS inertial sensors to detect severe shock and vibration levels while drilling. During drilling, information about shock and vibration was obtained from MEMS inertial sensors and analyzed utilizing wavelet packet analysis, where energy of a specific packet was derived and compared to a reference threshold. Information about shock and vibration levels allow mitigating actions to reduce or avoid these effects, resulting in a tremendous reduction of drilling cost per foot.

- **Continuous Borehole Surveying System Based on MEMS Inertial Sensors**

The continuous surveying of a well trajectory while drilling is a highly desirable application in the oil and gas drilling industry. This was not possible before this thesis

due to two limitations: the size of gyroscopes prevents their installation inside the drilling housing and the current directional drilling technology relies only on magnetometer and accelerometer measurements at stationary surveying stations. This thesis describes the development of a continuous borehole surveying system based on a complete low cost MEMS INS package.

A novel update scheme based on Kalman filtering was developed integrating INS measurements with external drilling parameter updates. The continuous drill bit rate of penetration and MCM position were applied as external measurement updates while drilling. Moreover, stationary updates of ZUPT, MCM position, and a magnetometer heading were applied to the Kalman filter when drilling was stopped so a new drill pipe stand could be connected.

Two experiments simulating the drilling through soft and hard formations were conducted. The two tests differ in the build up rate of the inclination angle. The inclination build up rate was $0.1^\circ/\text{s}$ while drilling in a soft formation and a slower rate of $0.01^\circ/\text{s}$ while drilling in a hard formation. The first test extended for a period of approximately two hours with an achieved position accuracy of 0.24 m, 0.72 m and 0.36 m along the drill bit North, East and vertical directions, respectively. The second test was run for over 5 hours and had a maximum position error of 0.25 m, 1.2 m and 0.41 m in North, East and vertical directions, respectively. It should be noted that this particular analysis/results is valid only for the class of the utilized inertial hardware and the defined

test parameters. More analysis is required for other inertial sensors and inclination build up rates in order to generalize the results.

- **Limiting Position and Velocity Errors at Telemetry Interruption Periods**

A telemetry interruption is a period when a communication problem prevents transferring of the external measurements updates to the Kalman filter. The position components of error begin to grow if there is a telemetry interruption of the continuous drill bit rate of penetration and MCM position updates; these errors continue to grow until continuous updates become available again. To reduce position error growth, zero integrated velocity and position error drift at periods of telemetry interruption was proposed. In this technique, the velocity and position of the drill bit along the entire interruption period are fixed at the last velocity and position reading before the interruption. This significantly reduced the magnitude of errors during periods of telemetry interruption.

- **Synthetic Attitude Angles**

Synthetic inclination and toolface angles based on accelerometer measurements were established in this thesis by making a use of the slow drilling operation. Improvements of 75 times for drill bit inclination angle and 30 times for toolface angle were achieved by utilizing the synthetic angles technique. The advantage of the synthetic inclination and toolface angles is their dependence only on accelerometer measurements.

Accelerometer measurements are more stable and exhibit less error drift than gyroscope measurements.

6.3 Recommendations and Future Research

- **Thermal Modeling of MEMS Inertial Sensors**

Temperature variations affect low cost MEMS sensor characteristics, particularly the sensor bias component. The performance characteristics of MEMS sensors can change and produce additional error known as a thermal noise error. This effect has not been studied in this thesis. Investigation of a thermal model that compensates for the drift in sensor output in drilling environments is needed.

- **MEMS Inertial Multi-Sensor Drilling Package**

In future development, multi-sensor MEMS accelerometers and gyroscopes will be installed inside the RSS collar directly behind the drill bit. A sensor fixture inside the RSS provides a redundancy of sensor measurements and thus a potential to improve the estimate of sensor errors. Improvements in the well trajectory position and attitude accuracies can take an advantage of a possible combination of eight triads for gyroscope measurements and eight triads for accelerometer measurements.

- **Drill Rig Testing**

The MEMS inertial drilling system developed here should be applied to a testing rig in an actual drilling environment, and similar analyses should be performed before commercialization of such a system.

- **Artificial Intelligence Technique to Aid Kalman Filtering**

Artificial intelligence techniques such as neural networks or fuzzy inference systems could aid Kalman filtering. If an intelligent algorithm can tune Kalman filter internal parameters (e.g., the apriori parameters of the system and the measurement noise matrices) while drilling, this could potentially enhance the filter state estimates and improve overall system accuracy.

REFERENCES

Akinniranye, G., Amanda, W., Elswaisy, H., Palacio, J., Poedjono, B and R. Goobie, (2007), "Implementation of a Shock and Vibration Mitigation Process: Achieving Real-Time Solutions and Savings," *Society of Petroleum Engineers / International Association of Drilling Contractors*, Middle East Drilling Technology Conference & Exhibition, Cairo, Egypt.

Amundsen, P.A., Ding, S., Datta, B. K., Torkildsen, T. and A. Saasen, (2008), "Magnetic Shielding during MWD Azimuth Measurements and Wellbore Positioning," *Indian Oil and Gas Technical Conference and Exhibition*, Mumbai, India.

Berger, P. E., Helgesen, T. B. and J. K. Kismul, (1999), "FE-MWD Logging in a Different Environment Induced by Drilling with a Rotary Steerable System," *Society of Petroleum Engineers Annual Technical Conference and Exhibition*, Houston, TX, USA.

Berger, P. E. and R. Sele, (1998), "Improving Wellbore Position Accuracy of Horizontal Wells by Using A Continuous Inclination Measurement From A Near Bit Inclination MWD Sensor," *Society of Petroleum Engineers International Conference on Horizontal Well Technology*, Calgary, Alberta, Canada

Bourgoyne, A. T., Millheim, K. K., Chenevert, M. E. and F. S. Young, (2005), “Applied Drilling Engineering,” *Tenth Printing Society of Petroleum Engineers Text Series*, Vol.2, Richardson, TX, USA.

Burke Hubbard, B., (1998), “The World According to Wavelets: The Story of a Mathematical Technique in the Making,” *AK Peters, Ltd.*, Second revised edition, Wellesley, MA, USA.

Burrus, C.S., Gopinath, R.A. and H. Guo, (1997), “Introduction to Wavelets and Wavelet Transforms,” *First Edition, Prentice Hall Inc.*, Englewood Cliffs, N.J., USA.

Chui, C. K., (1992), “Wavelets: A Tutorial in Theory and Application,” *Academic Press*, New York, NY, USA.

Conti, P. F., (1989), “Controlled Horizontal Drilling,” *Society of Petroleum Engineers / International Association of Drilling Contractors Drilling Conference*, New Orleans, LA, USA.

Crossbow , (2007), “Document 7430-0003-03 - IMU User’s Manual Models IMU300CC – IMU400CC – IMU400CD,” *Crossbow Technology Inc*, San Jose, CA, USA.

Daubechies, I., (1998), "Orthogonal Bases of Compactly Supported Wavelets," *Communication in Pure Applied Math Journal*, 41 (7): 909:996.

Edmondson, J., Chris, A., Dalton, C. and J. Johnstone, (2000), "The Application of Rotary Closed-Loop Drilling Technology to Meet the Challenges of Complex Wellbore Trajectories in the Janice Field," *Society of Petroleum Engineers / International Association of Drilling Contractors Drilling Conference*, New Orleans, LA, USA.

Eickelberg, D. , (1982), "Controlled Directional Drilling Instruments and Tools," 9th *International Symposium of firms Baker Oil Tools GmbH, Christensen Diamond Products GmbH, and Vetco Inspection GmbH.*

Ekseth, R., (1998), "Uncertainties in Connection with the Determination of Wellbore Positions," *a dissertation for the partial fulfillment of requirements for the degree of doctor of philosophy*, Norwegian University of Science and Technology, Norway.

El-Gizawy, M., A. Noureldin and N. El-Sheimy, (2006), "Performance Analysis of Tactical Grade Inertial Systems for Measurement-While-Drilling (MWD) Process," *Proceedings of IEEE/ION Position Location and Navigation Symposium*, PLANS, San Diego, CA, USA.

El-Gizawy, M., (2003), "Development of an Ionosphere Monitoring Technique Using GPS Measurements for High Latitude GPS Users," *a thesis for the partial fulfillment of requirements for the degree of Master of Science*, Department of Geomatics Engineering, University of Calgary, Calgary, AB, Canada.

El-Sheimy, N. and X. Niu, (2007), "The Promise of MEMS to the Navigation Community," *Inside GNSS, Invited Paper*, March/April Issue, pp. 46-56.

El-Sheimy, N., (2003), "Inertial Techniques and INS/DGPS Integration," *Lecture notes of ENGO 623*, The University of Calgary, Calgary, AB, Canada.

Estes, R. A. and D. M. Epplin, (2000), "Development of a Robust Gyroscopic Orientation Tool for MWD Operations," *Society of Petroleum Engineers Annual Technical Conference and Exhibition*, Dallas, TX, USA.

Fisher, E. K. and M. R. French, (1991), "Drilling the First Horizontal Well in The Gulf of Mexico: A Case History of East Cameron Block 278 well B-12," *Society of Petroleum Engineers Annual Technical Conference and Exhibition*, Dallas, TX, USA.

FOGIA, (1990), "Directional Drilling and Deviation Control Technology," *French Oil and Gas Industry Association (FOGIA) Technical Committee*, Gulf Publishing Company, Book Division, Houston, TX, USA.

Grindord, S. and C. Wolf, (1983), "Calculation of NMDC Length Required for Various Latitudes Developed From Field Measurements of Drill String Magnetization," *Society of Petroleum Engineers / International Association of Drilling Contractors Drilling Conference*, New Orleans, LA, USA.

Helm, W., (1991), "Method and Apparatus for Measurement of Azimuth of a Borehole While Drilling," *US patent # 5012412*.

Honeywell, (1997), "Document DS34468-01 - Critical Item Development Specification HG1700AG Inertial Measurement Unit," *Honeywell International Inc*, Minneapolis, MN, USA.

Hulsing R., (1989), "Borehole Survey System Utilizing Strapdown Inertial Navigation," *US patent # 4812977*.

Ideal Aerosmith, (2006), "Model 2103HT Three-Axis Positioning and Rate Table System," *Ideal Aerosmith Inc*, East Grand Forks, MN, USA.

Jekeli, C., (2000), "Inertial Navigation Systems with Geodetic Applications," *Walter de Gruyter*, New York, NY., USA.

Joshi, S. D. and W. Ding, (1991), "The Cost Benefits of Horizontal Drilling," *American Gas Association*, Arlington, VA, USA.

Kelsey, J. B., (1983), "A Wellbore Inertial Navigation System," *Society of Petroleum Engineers / International Association of Drilling Contractors Drilling Conference*, New Orleans, LA, USA.

Lyons, W. C. and G. J. Plisga, (2005), "Standard Handbook of Petroleum and Natural Gas Engineering," *Gulf Professional Publishing*, Linacre House, Jordan Hill, Oxford, UK.

Mallat, S., (1999), "A Wavelet Tour of Signal Processing," *Second Edition*, Academic Press, London, UK.

Mallat, S., (1989), "A Theory for Multiresolution Signal Decomposition: The Wavelet Representation," *IEEE Transactions on Pattern Analysis and Machine Intelligence*, vol. 11, pp. 674- 693.

Mallat, S., (1989), "Multifrequency Channel Decompositions of Images and Wavelet Models," *IEEE Transactions on Acoustics, Speech & Signal Processing*, vol. 37, pp. 2091- 2110.

Mason, C. M. and H. L. Taylor, (1971), "Systematic Approach to Well Surveying Calculations," *Society of Petroleum Engineers*, SPE3362.

McMillian, W., (1981), "Planning the Directional Well – A Calculation Method," *Journal of Petroleum Technology*, 1981; 33(6):952-962.

Misiti, M., Y. Misiti, G. Oppenheim and J. M. Poggi, (2000), "Wavelet Toolbox for the Use with Matlab," *The Math Works Inc.*, MA, USA.

Mohamed, A.H., (1999), "Optimizing the Estimation Procedure in INS/GPS Integration for kinematic applications," *a dissertation for the partial fulfillment of requirements for the degree of Doctor of Philosophy*, UCGE report # 20127, Department of Geomatics Engineering, University of Calgary, Calgary, AB, Canada.

Noureldin, A., (2002), "New Measurement-While-Drilling Surveying Technique Utilizing a Set of Fiber Optic Rotation Sensors," *a dissertation for the partial fulfillment of requirements for the degree of Doctor of Philosophy*, Department of Electrical and Computer Engineering, University of Calgary, Calgary, AB, Canada.

Noureldin A., Tabler, H., Irvine-Halliday, D. and M. Mintchev, (2001), "Measurement-While-Drilling Surveying of Near-Vertical Wells and In Sections of Multi-Well Structure Using FOG-Based INS," *National Technical Meeting of the Institute of Navigation*, Long Beach, CA, USA.

NovAtel, (2008), "SPAN Technology for OEMV," *User Manual*, Calgary, AB, Canada.

Noy K. A. and J. G. Leonard, (1997), "A New Rate Gyroscopic Wellbore Survey System Achieves The Accuracy and Operational Flexibility Needed for Today's Complex Drilling Challenges," *Society of Petroleum Engineers / International Association of Drilling Contractors Drilling Conference*, Amsterdam, Netherlands.

Ogden, R.T., (1997), "Essential Wavelets for Statistical Applications and Data Analysis," *Birkhäuser Inc.*, Boston, MA, USA.

Parkinson W. D., (1983), "Introduction to Geomagnetism," *Scottish Academic Press*, Edinburgh, 1983.

Ripka, P., (2001), "Magnetic Sensors and Magnetometers," *Artech House Inc.*, Norwood, MA, USA.

Robertson, D.C., Camps, O. I., Mayer J.S. and Gish, W. B., (1996), "Wavelets and Electromagnetic Power System Transients," *IEEE Transaction on Power Delivery*, 11 (2): 1050-1056.

Russel, A.W. and R. F. Roesler, (1985), "Reduction of Nonmagnetic Drill Collar Length Through Magnetic Azimuth Correction Technique," *Society of Petroleum Engineers / International Association of Drilling Contractors Drilling Conference*, New Orleans, LA, USA.

Russel, M. K. and A. W. Russel, (1979), "Surveying of Boreholes," *US patent # 4163324*.

Salychev, O., (1998), "Inertial Systems in Navigation and Geophysics," *Bauman MSTU press, Moscow*.

Schwarz, K. P and M. Wei, (1999), "INS / GPS Integration for Geodetic Applications," *Lecture notes of ENGO 623*, Department of Geomatics Engineering at the University of Calgary, AB, Canada.

Sesay, A.B., (2003), "Adaptive Signal Processing," *Lecture notes of ENEL 671*, Department of Electrical and Computer Engineering at the University of Calgary, Calgary, AB, Canada.

Steinberg, D. S., (2000), "Vibration Analysis for Electronic Equipment," *3rd Edition, A Wiley-Interscience Publication, John Wiley & Sons, Inc., ISBN 0-471-37685-X, USA*.

Stephenson, M. A. and H. Wilson, (1992), "Improving Quality Control of Directional Survey Data with Continuous Inertial Navigation," *Society of Petroleum Engineers, Drilling Engineering, V7 (2), 100-105*.

Thorogood, J. L., (1990), "Instrument performance models and their application to directional surveying operations," *Society of Petroleum Engineers Drilling Engineering*, V5 (4), pp: 294-298.

Thorogood, J. L. and D. R. Knott, (1990), "Surveying Techniques with A Solid State Magnetic Multi-Shot Device," *Society of Petroleum Engineers Drilling Engineering*, V5 (3), pp: 209-214.

Thorogood J. L. and D. R. Knott, (1989), "Surveying Techniques With a Solid State Magnetic Multi-Shot Device," *Society of Petroleum Engineers / International Association of Drilling Contractors Drilling Conference*, New Orleans, LA, USA.

Thorogood, J. L., (1989), "Directional Survey Operations Management," *Journal of Petroleum Technology*, pp: 1250-1252.

Titterton, D. H. and J. L. Weston, (1997), "Strapdown Inertial Navigation Technology," *Peter Peregrinus Ltd.*, London, UK.

Torkildsen, T., Edvardsen, I., Fjogstad, A., Saasen, A., Amundsen, P.A. and T. H. Omland, (2004), "Drilling Fluid Affects MWD Magnetic Azimuth and Wellbore Position," *Society of Petroleum Engineers / International Association of Drilling Contractors Drilling Conference*, Dallas, TX, USA.

Uttecht, G. W. and J. P. de Wadrt, (1983), "Application of Small Diameter Inertial Grade Gyroscopes Significantly Reduces Borehole Position Uncertainty," *Society of Petroleum Engineers / International Association of Drilling Contractors Drilling Conference*, New Orleans, LA, USA.

Weatherford, (2006), Personal Communication with Research and Development Group, Houston, TX, USA.

Weijermans, P., Ruzska, J., Jamshidian, H. and M. Matheson, (2001), "Drilling with Rotary Steerable System Reduces Wellbore Tortuosity," *Society of Petroleum Engineers / International Association of Drilling Contractors Drilling Conference*, Amsterdam, The Netherlands.

Wilson, H. and A. G. Brooks, (2001), "Wellbore Position Errors Caused By Drilling Fluid Contamination," *Society of Petroleum Engineers Annual Technical Conference and Exhibition*, New Orleans, LA, USA.

Wolf C.J.M. and J. P. deWardt, (1981), "Borehole Position Wncertainty – Analysis of Measuring Methods and Derivation of Systematic Error Model," *Journal of Petroleum Technology*, pp: 2339-2350.

Wright J. W., (1988), "Directional Drilling Azimuth Reference Systems," *Society of Petroleum Engineers / International Association of Drilling Contractors Drilling Conference*, Dallas, TX, USA.

Yazdi, N., Ayazi, F. and Najafi. K., (1998), "Micromachined Inertial Sensors," *IEEE*, Vol. 86, No. 8.

Zijsling, D. H and R. A. Wilson, (1989), "Improved Magnetic Surveying Techniques: Field Experience," *Society of Petroleum Engineers Offshore Conference*, Aberdeen, UK.

APPENDIX A:

MODELING MOTION IN NAVIGATION FRAME

A.1 Position Mechanization in the Navigation Frame

Accelerometer and gyroscope measurements of an inertial measurements unit mounted inside an RSS collar are taken in the b-frame, and then transformed into the n-frame using the R_b^n . The position of the RSS collar as mapped in the n-frame r^n is expressed by the latitude φ , longitude λ , and altitude h of the curvilinear coordinate.

$$r^n = \begin{pmatrix} \varphi \\ \lambda \\ h \end{pmatrix}. \quad \text{A.1}$$

It is important to define the three velocity components in the n-frame. They are the north velocity V^n , east velocity V^e , and vertical velocity V^u .

$$V^n = \begin{pmatrix} V^e \\ V^n \\ V^u \end{pmatrix}. \quad \text{A.2}$$

The velocity components in the n-frame as well as the latitude φ and longitude λ for any given location on the earth's surface are illustrated in Figure A.1.

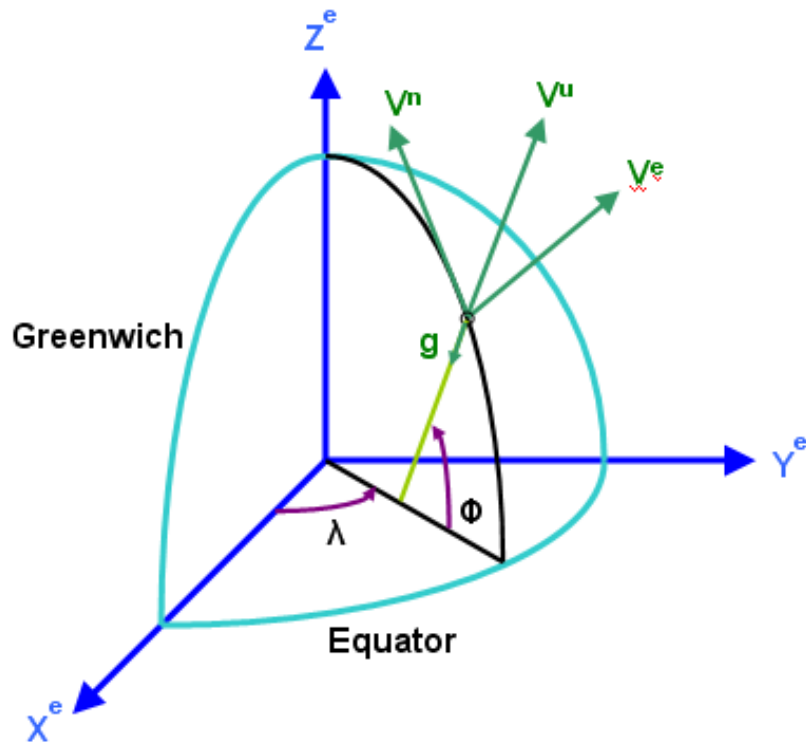


Figure A.1: Velocity Components of a Given Point in the Navigation Frame

The velocity components are directly related to the position time rate of change components, and can be expressed as [Schwarz and Wei, 1999]:

$$\dot{r}^n = \begin{pmatrix} \dot{\phi} \\ \dot{\lambda} \\ \dot{h} \end{pmatrix} = \begin{pmatrix} 0 & 1/M + h & 0 \\ 1/(N + h) \cos \phi & 0 & 0 \\ 0 & 0 & 1 \end{pmatrix} \begin{pmatrix} V^e \\ V^n \\ V^u \end{pmatrix} = D^{-1} V^n, \quad \text{A.3}$$

where M is the meridian radius of curvature and N is the prime vertical radius of curvature of the earth ellipsoid.

A.2 Velocity Mechanization in the Navigation Frame

An IMU mounted inside an RSS collar measures the acceleration in the b-frame along three mutually orthogonal directions using the accelerometer triad.

$$f^b = \begin{pmatrix} f_x \\ f_y \\ f_z \end{pmatrix}, \quad \text{A.4}$$

Then these measurements are transformed into the n-frame using the transformation matrix R_b^n :

$$f^n = \begin{pmatrix} f^e \\ f^n \\ f^u \end{pmatrix} = R_b^n f^b = R_b^n \begin{pmatrix} f_x \\ f_y \\ f_z \end{pmatrix}. \quad \text{A.5}$$

Integration of the acceleration components f^n in the n-frame should derive the velocity components v^n in the n-frame. However this is not the case due to the earth's rotation rate, the change of orientation of the navigation frame with respect to the earth, and the earth's gravity field. These "earth" effects are explained below:

The earth's rotation rate: $\omega^e = 15 \text{ deg/hr}$ is interpreted in the n-frame as an angular velocity vector ω_{ie}^n as follows:

$$\omega_{ie}^n = \begin{pmatrix} 0 \\ \omega^e \cos \varphi \\ \omega^e \sin \varphi \end{pmatrix}. \quad \mathbf{A.6}$$

The change of orientation of the n-frame with respect to the earth arises due to the definition of the north and vertical directions of the navigation frame. The north direction is always tangential to the meridian while the vertical direction is always normal to the earth's surface. This is expressed by the angular velocity vector ω_{en}^n and is illustrated in Figure A.2.

$$\omega_{en}^n = \begin{pmatrix} -\dot{\varphi} \\ \dot{\lambda} \cos \varphi \\ \dot{\lambda} \sin \varphi \end{pmatrix} = \begin{pmatrix} -\frac{V^n}{M+h} \\ \frac{V^e}{N+h} \\ \frac{V^e \tan \varphi}{N+h} \end{pmatrix}. \quad \mathbf{A.7}$$

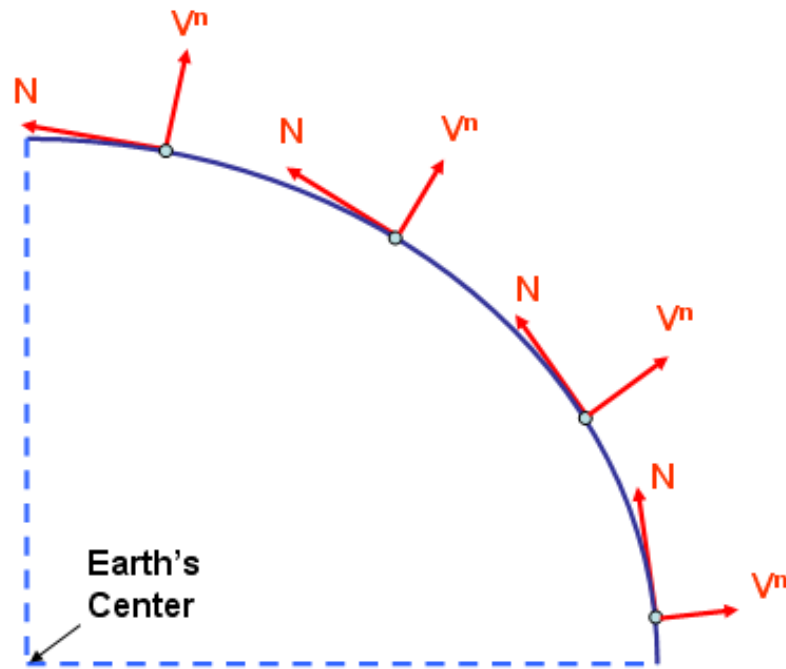


Figure A.2: Change of Orientation of the Navigation Frame

The earth's gravity also effects the IMU acceleration measurements. The earth's gravity field can be accurately computed using a well-known gravity model as follows [Schwarz and Wei, 1999]:

$$g = a_1(1 + a_2 \sin^2 \varphi + a_3 \sin^4 \varphi) + (a_4 + a_5 \sin^2 \varphi)h + a_6 h^2, \quad \mathbf{A.8}$$

where,

$$\begin{aligned} a_1 &= 9.7803267715 \text{ m/sec}^2 & a_4 &= -0.000003087691089 \text{ 1/sec}^2 \\ a_2 &= 0.0052790414 & a_5 &= 0.000000004397731 \text{ 1/sec}^2 \\ a_3 &= 0.0000232718 & a_6 &= 0.000000000000721 \text{ 1/(m} \\ & & & \text{sec}^2) \end{aligned}$$

The earth's gravity field is then presented in the n-frame as:

$$g^n = \begin{pmatrix} 0 \\ 0 \\ -g \end{pmatrix}^T. \quad \text{A.9}$$

Taking the three “earth” effects into consideration, the time rate of change of the velocity components V^n of the drill collar in the n-frame is expressed as [Schwarz and Wei, 1999]:

$$\dot{V}^n = R_b^n f^b - (2\Omega_{ie}^n + \Omega_{en}^n) V^n + g^n, \quad \text{A.10}$$

where Ω_{ie}^n and Ω_{en}^n are the skew-symmetric matrices of ω_{ie}^n and ω_{en}^n , respectively;

they are expressed as:

$$\Omega_{ie}^n = \begin{pmatrix} 0 & -\omega^e \sin \varphi & \omega^e \cos \varphi \\ \omega^e \sin \varphi & 0 & 0 \\ -\omega^e \cos \varphi & 0 & 0 \end{pmatrix}, \quad \text{A.11}$$

$$\Omega_{en}^n = \begin{pmatrix} 0 & -\frac{V^e \tan \varphi}{N+h} & \frac{V^e}{N+h} \\ \frac{V^e \tan \varphi}{N+h} & 0 & \frac{V^n}{M+h} \\ -\frac{V^e}{N+h} & -\frac{V^n}{M+h} & 0 \end{pmatrix}. \quad \text{A.12}$$

A.3 Attitude Mechanization in the Navigation Frame

The azimuth, inclination, and toolface angles, known as attitude angles of the moving drill collar, are determined by solving the time derivative equation of the transformation matrix R_b^n . They are obtained by solving the following differential equations [Schwarz and Wei, 1999]:

$$\dot{R}_b^n = R_b^n \Omega_{nb}^b = R_b^n (\Omega_{ib}^b - \Omega_{in}^b), \quad \text{A.13}$$

where Ω_{ib}^b is the skew-symmetric matrix of the angular velocities measurements by the gyroscope. This skew-symmetric matrix corresponds to the angular velocity vector ω_{ib}^b ; it is expressed as:

$$\Omega_{ib}^b = \begin{pmatrix} 0 & -\omega_z & \omega_y \\ \omega_z & 0 & \omega_x \\ -\omega_y & \omega_x & 0 \end{pmatrix}. \quad \text{A.14}$$

The gyroscopes measure the angular velocities of the moving RSS collar. In addition, they measure the earth's rotation and the change of orientation of the navigation frame. Therefore, the angular velocities Ω_{in}^b are subtracted from Ω_{ib}^b in order to remove these two effects.

The angular velocities Ω_{in}^b consist of two parts. The first part accounts for the earth's rotation rate Ω_{ie}^b , while the second part accounts for the change of orientation of the navigation frame with respect to the earth-fixed frame Ω_{en}^b . It can be expressed as:

$$\Omega_{in}^b = \Omega_{ie}^b + \Omega_{en}^b. \quad \text{A.15}$$

These skew symmetric angular velocity matrices correspond to:

$$\omega_{in}^b = \omega_{ie}^b + \omega_{en}^b = R_n^b \omega_{ie}^n + R_n^b \omega_{en}^n = R_n^b (\omega_{ie}^n + \omega_{en}^n), \quad \text{A.16}$$

$$\omega_{in}^b = R_n^b \left[\begin{array}{c} 0 \\ \omega^e \cos \varphi \\ \omega^e \sin \varphi \end{array} \right] + \left[\begin{array}{c} -\frac{V^n}{M+h} \\ \frac{V^e}{N+h} \\ \frac{V^e \tan \varphi}{N+h} \end{array} \right] = R_n^b \left[\begin{array}{c} -\frac{V^n}{M+h} \\ \frac{V^e}{N+h} + \omega^e \cos \varphi \\ \frac{V^e \tan \varphi}{N+h} + \omega^e \sin \varphi \end{array} \right]. \quad \text{A.17}$$

The corresponding skew symmetric matrix Ω_{in}^b can then be determined. Finally, the time derivative equation of the transformation matrix R_b^n can be solved and the azimuth, inclination, and toolface angles of the moving drill collar can be determined [Schwarz and Wei, 1999]:

$$\dot{R}_b^n = R_b^n \Omega_{nb}^b = R_b^n (\Omega_{ib}^b - \Omega_{in}^b), \quad \text{A.18}$$

$$\dot{R}_b^n = R_b^n \left[\begin{array}{c} \omega^x \\ \omega^y \\ \omega^z \end{array} \right] - R_n^b \left[\begin{array}{c} -\frac{V^n}{M+h} \\ \frac{V^e}{N+h} + \omega^e \cos \varphi \\ \frac{V^e \tan \varphi}{N+h} + \omega^e \sin \varphi \end{array} \right]. \quad \mathbf{A.19}$$

APPENDIX B:

INS MECHANIZATION EQUATIONS SOLUTION

BY QUATERNION

The quaternion is based on Euler's theorem which states that the rotation of a rigid body represented by a navigation frame with respect to a navigation reference frame can be expressed in terms of a rotation angle Θ about a fixed axis and the direction cosine of the rotation axis that defines the rotation direction [Salychev, 1998]. This is shown in Figure B.1.

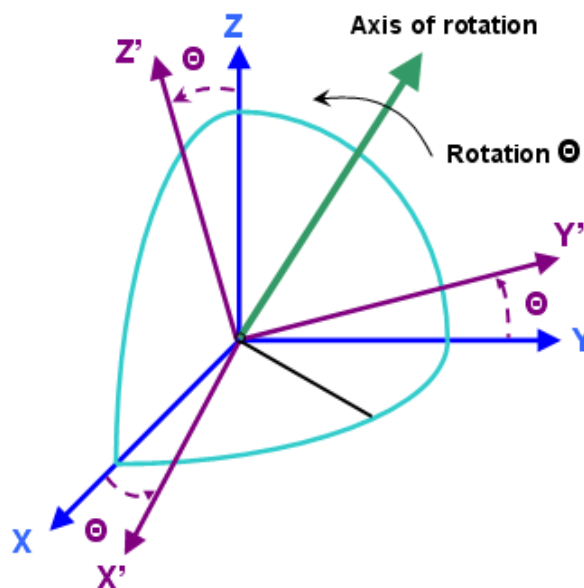


Figure B.1: Quaternion Rotation

There are a number of advantages of using the quaternion approach. First, the quaternion contains only four differential equations, while six differential equations are needed to model the rotation matrix R_b^n . In addition, the quaternion solution avoids singularity problems that can exist with other solution methods. The computational simplicity as well of the quaternion method as compared to other methods is another advantage.

Quaternion parameters are introduced to describe the rotation of a body frame with respect to a reference navigation frame. They are expressed as:

$$Q = \begin{pmatrix} q_1 \\ q_2 \\ q_3 \\ q_4 \end{pmatrix} = \begin{pmatrix} (\Theta_x / \Theta) \sin(\Theta / 2) \\ (\Theta_y / \Theta) \sin(\Theta / 2) \\ (\Theta_z / \Theta) \sin(\Theta / 2) \\ \cos(\Theta / 2) \end{pmatrix}, \quad \text{B.1}$$

where the rotation angle $\Theta = \sqrt{\Theta_x^2 + \Theta_y^2 + \Theta_z^2}$, and the three direction cosines of the

rotation axis with respect to the navigation frame are $\frac{\Theta_x}{\Theta}, \frac{\Theta_y}{\Theta}, \frac{\Theta_z}{\Theta}$.

According to the quaternion approach, any rigid body rotation can be described using three independent quaternion components. This is explained by the following relationship:

$$q_1^2 + q_2^2 + q_3^2 + q_4^2 = 1.$$

B.2

This relationship, however, can be violated due to computational errors. Therefore, special normalization procedures are implemented to compensate for this effect [Salychev, 1998] if an error Δ exists after the computation of the quaternion parameters:

$$\Delta = 1 - (q_1^2 + q_2^2 + q_3^2 + q_4^2).$$

B.3

As a result, the quaternion parameter vector Q will be updated after each computational step according to the following expression:

$$\hat{Q} = \frac{Q}{\sqrt{1-\Delta}} \cong Q \left(1 + \frac{\Delta}{2} \right).$$

B.4

A quaternion first-order differential equation describes the time rate of change of the quaternion; it is:

$$\dot{Q} = \frac{1}{2} \Omega(\omega) Q,$$

B.5

where $\Omega(\omega)$ is a skew-symmetric matrix expressed as:

$$\Omega(\omega) = \begin{pmatrix} 0 & \omega_z & -\omega_y & \omega_x \\ -\omega_z & 0 & \omega_x & \omega_y \\ \omega_y & -\omega_x & 0 & \omega_z \\ -\omega_x & -\omega_y & -\omega_z & 0 \end{pmatrix}, \quad \text{B.6}$$

where ω_x , ω_y , and ω_z are the angular velocities of the body rotation measured by the gyroscope triad installed inside the drill collar after compensating for the effects of the earth's rotation and the change of orientation of the navigation frame.

In order to solve the quaternion first-order differential equation in Equation B.5, Euler's method is applied. This determines the quaternion parameters Q_{k+1} at time t_{k+1} based on the values of the quaternion parameters Q_k at time t_k as follows:

$$Q_{k+1} = Q_k + \left(\frac{1}{2} \Omega(\omega_k) Q_k \right) (t_{k+1} - t_k). \quad \text{B.7}$$

When the quaternion parameters are computed at a certain time t_k , the rotation matrix R_b^n can then be determined according to the following relationship:

$$R_b^n = \begin{pmatrix} R_{11} & R_{12} & R_{13} \\ R_{21} & R_{22} & R_{23} \\ R_{31} & R_{32} & R_{33} \end{pmatrix}, \quad \text{B.8}$$

$$R_b^n = \begin{pmatrix} q_1^2 - q_2^2 - q_3^2 + q_4^2 & 2(q_1q_2 - q_3q_4) & 2(q_1q_3 + q_2q_4) \\ 2(q_1q_2 + q_3q_4) & -q_1^2 + q_2^2 - q_3^2 + q_4^2 & 2(q_2q_3 - q_1q_4) \\ 2(q_1q_3 - q_2q_4) & 2(q_2q_3 + q_1q_4) & -q_1^2 - q_2^2 + q_3^2 + q_4^2 \end{pmatrix}. \quad \mathbf{B.9}$$

APPENDIX C:

SURVEYING ERROR MODELLING USING

LINEAR STATE EQUATIONS

C.1 Drill String Coordinate Errors

The errors within a drill string coordinates vector are expressed as the difference between the unknown true coordinates r^n and the computed coordinate r'^n . Therefore, by applying the Taylor series expansion to a first order approximation, the time derivative of the coordinate errors is [Schwarz and Wei, 1999]:

$$\delta \dot{r}^n = \dot{\bar{r}}^n - \dot{r}^n = \frac{\delta}{\delta r^n} (\dot{r}^n) \delta r^n = \frac{\delta}{\delta r^n} \left\{ \begin{pmatrix} 0 & \frac{1}{M+h} & 0 \\ \frac{1}{(N+h)\cos\varphi} & 0 & 0 \\ 0 & 0 & 1 \end{pmatrix} \begin{pmatrix} V^e \\ V^n \\ V^u \end{pmatrix} \right\} \delta r^n.$$

C.1

Differentiating Equation C.1 gives the following expression:

$$\delta \mathbf{r}^n \begin{pmatrix} \delta \dot{\varphi} \\ \delta \dot{\lambda} \\ \delta \dot{h} \end{pmatrix} = \begin{pmatrix} 0 & \frac{1}{M+h} & 0 \\ \frac{1}{(N+h)\cos\varphi} & 0 & 0 \\ 0 & 0 & 1 \end{pmatrix} \begin{pmatrix} \delta V^e \\ \delta V^n \\ \delta V^u \end{pmatrix} + \begin{pmatrix} 0 & 0 & \frac{-V^u}{(M+h)^2} \\ \frac{V^e \tan\varphi}{(N+h)\cos\varphi} & 0 & \frac{-V^e}{(N+h)^2 \cos\varphi} \\ 0 & 0 & 0 \end{pmatrix} \begin{pmatrix} \delta\varphi \\ \delta\lambda \\ \delta h \end{pmatrix} . \quad \text{C.2}$$

The second term in Equation C.2 can be neglected as it is a very small value resulting from velocity components divided by the earth's radius. Hence the coordinate errors are mainly dependent on the velocity errors in the first term.

C.2 Drill String Velocity Errors

Velocity components V^e , V^n , and V^u of the drill collar in the navigation-frame are expressed in Equation A.10. Velocity errors are derived by applying the Taylor series expansion to a first order approximation to Equation A.10 as follows [Schwarz and Wei, 1999]:

$$\begin{pmatrix} \delta \dot{V}^e \\ \delta \dot{V}^n \\ \delta \dot{V}^u \end{pmatrix} = \begin{pmatrix} 0 & f_u & -f_n \\ -f_u & 0 & f_e \\ f_n & -f_e & 0 \end{pmatrix} \begin{pmatrix} \delta \theta \\ \delta \phi \\ \delta \psi \end{pmatrix} + R_b^n \begin{pmatrix} \delta f_x \\ \delta f_y \\ \delta f_z \end{pmatrix} + \\
\begin{pmatrix} (2\omega^e \sin \varphi)V^u + (2\omega^e \cos \varphi)V^n + \frac{V^n V^e}{(N+h) \cos^2 \varphi} & 0 & 0 \\ (-2\omega^e \cos \varphi)V^e - \frac{(V^e)^2}{(N+h) \cos^2 \varphi} & 0 & 0 \\ (2\omega^e \sin \varphi)V^e & 0 & \frac{2\gamma}{R} \end{pmatrix} \begin{pmatrix} \delta \varphi \\ \delta \lambda \\ \delta h \end{pmatrix} + \\
\begin{pmatrix} -\frac{V^u}{N+h} + \frac{V^n \tan \varphi}{N+h} & 2\omega^e \sin \varphi + \frac{V^e \tan \varphi}{(N+h)} & -2\omega^e \cos \varphi - \frac{V^e}{(N+h)} \\ -2\omega^e \sin \varphi - \frac{2V^e \tan \varphi}{(N+h)} & -\frac{V^u}{(M+h)} & -\frac{V^n}{(M+h)} \\ 2\omega^e \cos \varphi + \frac{2V^e}{(N+h)} & \frac{2V^n}{(M+h)} & 0 \end{pmatrix} \begin{pmatrix} \delta V^e \\ \delta V^n \\ \delta V^u \end{pmatrix}$$

C.3

The third and fourth terms of Equation C.3 are very small due to dividing the velocity components by the earth's radius, and they can be neglected. Therefore, the first two terms are the major components of the velocity errors.

It is important to examine the first and second terms of Equation C.3, where δV^e and δV^n consist of a Schuler part and a nonstationary part. The Schuler part includes the Schuler effect that implies that δV^e and δV^n are bounded over time. They oscillate

over time with a Schuler frequency of approximately 1/5000 Hz with a period of 84.4 minutes [El-Sheimy, 2003]. Additionally, the Schuler part establishes a strong coupling relationship between δV^e and $\delta\phi$, and between δV^n and $\delta\theta$, due to the fact that the up acceleration on the navigation frame f_u measures a value close to the acceleration of gravity (9.81 m/s^2). This is a larger value when compared to the acceleration in east and north directions, f_e and f_n , respectively. This implies if one error state is accurately estimated with one of the optimal estimation tools, the other coupled error state can be estimated accurately too [El-Sheimy, 2003].

The nonstationary part of Equation C.3 relates the drill string horizontal velocity errors δV^e and δV^n to the azimuth error $\delta\Psi$. It depends on the horizontal body acceleration components, and hence there is no strong coupling between the horizontal velocity errors δV^e and δV^n and the azimuth error $\delta\Psi$. This leads to a continuous change of the nonstationary part with time depending on the azimuth drift.

C.3 Drill String Attitude Errors

The time rate of change of the errors in roll (toolface) $\delta\theta$, pitch (90 – inclination) $\delta\phi$, and azimuth (heading) $\delta\psi$ of the drill collar in the navigation-frame are given as [Schwarz and Wei, 1999]:

$$\begin{pmatrix} \delta\dot{\theta} \\ \delta\dot{\phi} \\ \delta\dot{\psi} \end{pmatrix} = -\Omega_{in}^n \begin{pmatrix} \delta\theta \\ \delta\phi \\ \delta\psi \end{pmatrix} - \delta\omega_{in}^n + R_b^n \begin{pmatrix} \delta\omega_x \\ \delta\omega_y \\ \delta\omega_z \end{pmatrix}.$$

C.4

The attitude angle errors are derived from angular velocity errors due to the earth's rotation and the change of orientation of navigation frame on the earth's surface presented in the first term of Equation C.4. The second term of Equation C.4 depends on the coordinate and velocity errors, while the last term presets the vector of the angular velocities measurement errors (gyroscope drift). Equation C.4 can be rewritten as [Schwarz and Wei, 1999]:

$$\begin{pmatrix} \delta\dot{\theta} \\ \delta\dot{\phi} \\ \delta\dot{\psi} \end{pmatrix} = \begin{pmatrix} 0 & \frac{1}{M+h} & 0 \\ \frac{-1}{N+h} & 0 & 0 \\ \frac{-\tan\varphi}{N+h} & 0 & 0 \end{pmatrix} \begin{pmatrix} \delta V^e \\ \delta V^n \\ \delta V^u \end{pmatrix} + R_b^n \begin{pmatrix} \delta\omega_x \\ \delta\omega_y \\ \delta\omega_z \end{pmatrix} +$$

$$\begin{pmatrix} 0 & 0 & \frac{-V^n}{(M+h)^2} \\ \omega^e \sin\varphi & 0 & \frac{V^e}{(N+h)^2} \\ -\omega^e \cos\varphi - \frac{V^e}{(N+h)\cos^2\varphi} & 0 & \frac{V^e \tan\varphi}{(N+h)^2} \end{pmatrix} \begin{pmatrix} \delta\varphi \\ \delta\lambda \\ \delta h \end{pmatrix} +$$

$$\begin{pmatrix} 0 & \omega^e \sin \varphi + \frac{V^e \tan \varphi}{(N+h)} & -\omega^e \cos \varphi - \frac{V^e}{(N+h)} \\ -2\omega^e \sin \varphi - \frac{V^e \tan \varphi}{(N+h)} & 0 & -\frac{V^n}{(M+h)} \\ \omega^e \cos \varphi + \frac{V^e}{(N+h)} & \frac{V^n}{(M+h)} & 0 \end{pmatrix} \begin{pmatrix} \delta\theta \\ \delta\phi \\ \delta\psi \end{pmatrix}.$$

C.5

The first two terms of Equation C.5 are the major components for deriving the attitude errors, where the first term on the right hand side represents the relationship between the attitude errors and velocity errors. The second term includes the effect of the drifts of the three utilized gyroscopes. The third term represents the position error effect on the attitude error, which is very insignificant due to division of the velocity components by the earth's radius and the earth's rotation rate components. The last term on the right hand side is insignificant as well for the same reasons as the third term.

C.4 Inertial Sensor Error Modelling

The three accelerometers' random errors are presented as follows [Gelb, 1974; Brown and Hwang, 1992]:

$$\begin{pmatrix} \dot{\delta f}_x \\ \dot{\delta f}_y \\ \dot{\delta f}_z \end{pmatrix} = \begin{pmatrix} -\alpha_x & 0 & 0 \\ 0 & -\alpha_y & 0 \\ 0 & 0 & -\alpha_z \end{pmatrix} \begin{pmatrix} \delta f_x \\ \delta f_y \\ \delta f_z \end{pmatrix} + \begin{pmatrix} \sqrt{2\alpha_x \sigma_x^2} \\ \sqrt{2\alpha_y \sigma_y^2} \\ \sqrt{2\alpha_z \sigma_z^2} \end{pmatrix} w(t), \quad \text{C.5}$$

where α_x , α_y , and α_z are the reciprocals of the time correlation parameters of the modelled random processes associated with the accelerometer measurements f_x , f_y , and f_z , respectively. σ_x^2 , σ_y^2 , and σ_z^2 are variances of the random processes. Finally, $w(t)$ is a unity-variance white Gaussian noise. Similarly, random errors for the three gyroscope measurements are described as follows [Gelb, 1974; Brown and Hwang, 1992]:

$$\begin{pmatrix} \delta\dot{\omega}_x \\ \delta\dot{\omega}_y \\ \delta\dot{\omega}_z \end{pmatrix} = \begin{pmatrix} -\beta_x & 0 & 0 \\ 0 & -\beta_y & 0 \\ 0 & 0 & -\beta_z \end{pmatrix} \begin{pmatrix} \delta\omega_x \\ \delta\omega_y \\ \delta\omega_z \end{pmatrix} + \begin{pmatrix} \sqrt{2\beta_x\sigma_x^2} \\ \sqrt{2\beta_y\sigma_y^2} \\ \sqrt{2\beta_z\sigma_z^2} \end{pmatrix} w(t),$$

C.6

where β_x , β_y , and β_z are the reciprocals of the time correlation parameters of the modelled random processes associated with the gyroscope measurements ω_x , ω_y , and ω_z , respectively. The measurements errors of the inertial sensors are known to drift with time in the absence of external measurements updates. This error growth has to be limited by applying an optimal estimation tool such as Kalman filtering.